

## **Copyright Warning & Restrictions**

The copyright law of the United States (Title 17, United States Code) governs the making of photocopies or other reproductions of copyrighted material.

Under certain conditions specified in the law, libraries and archives are authorized to furnish a photocopy or other reproduction. One of these specified conditions is that the photocopy or reproduction is not to be “used for any purpose other than private study, scholarship, or research.” If a user makes a request for, or later uses, a photocopy or reproduction for purposes in excess of “fair use” that user may be liable for copyright infringement,

This institution reserves the right to refuse to accept a copying order if, in its judgment, fulfillment of the order would involve violation of copyright law.

**Please Note: The author retains the copyright while the New Jersey Institute of Technology reserves the right to distribute this thesis or dissertation**

Printing note: If you do not wish to print this page, then select “Pages from: first page # to: last page #” on the print dialog screen

The Van Houten library has removed some of the personal information and all signatures from the approval page and biographical sketches of theses and dissertations in order to protect the identity of NJIT graduates and faculty.

## **ABSTRACT**

### **NORMAL-STRENGTH AND HIGH-STRENGTH CONCRETE COLUMNS UNDER CYCLIC AXIAL LOAD AND BIAXIAL MOMENT**

**by  
Mehdi Zarei**

The technique of using Carbon Fiber Reinforced Polymer (CFRP) materials to repair and strengthen various concrete members has become popular in the structural retrofitting field as an effective way to enhance the strength and ductility of concrete members due to its superior mechanical properties. In this study a method was introduced to study the behavior of concrete columns with and without CFRP jackets under constant axial load and variable lateral load. The lateral load was applied monotonically and cyclically. To predict the behavior of concrete columns under monotonic and cyclic compressive loadings, a computer code was developed to produce the moment-curvature diagram for concrete sections. The moment-curvature diagram was then input in SAP2000 to study the behavior of reinforced concrete columns. The result of this analysis was found to correlate with experimental data well.

The behavior of high-strength concrete (HSC) columns having various properties and subjected to a variety of loading conditions has been the topic of considerable investigation. Of particular significance in this area is the behavior of HSC columns under cyclic compressive load with bidirectional eccentricity. For the experimental investigation, tests of six square slender HSC columns were conducted under stroke control to achieve both ascending and descending branches of the load-deformation curves.

Analysis of HSC columns subjected to cyclic axial compression with bidirectional eccentricity was approached from the standpoint of a three-dimensional problem. A computer program based on the extended finite segment method and accounting for geometrical nonlinearity has been proposed here to predict the load-deflection curves of HSC columns under cyclical loading. The HSC stress-strain relationship obtained by parametric study and experimental investigation into the behavior of concrete under cyclical load history has been incorporated into the numerical procedure.

The presented computer analysis results have been compared with the experimental data, and a satisfactory agreement was attained for both the ascending and descending branches of the load-deformation curves.

**NORMAL-STRENGTH AND HIGH-STRENGTH CONCRETE COLUMNS  
UNDER CYCLIC AXIAL LOAD AND BIAXIAL MOMENT**

**by  
Mehdi Zarei**

**A Dissertation  
Submitted to the Faculty of  
New Jersey Institute of Technology  
in Partial Fulfillment of the Requirements for the Degree of  
Doctor of Philosophy in Civil Engineering**

**John A. Reif, Jr. Department of  
Civil and Environmental Engineering**

**January 2016**

Copyright © 2016 by Mehdi Zarei

**ALL RIGHTS RESERVED**

**APPROVAL PAGE**

**NORMAL-STRENGTH AND HIGH-STRENGTH CONCRETE COLUMNS  
UNDER CYCLIC AXIAL LOAD AND BIAXIAL MOMENT**

**Mehdi Zarei**

---

Dr. Taha F. Marhaba, Dissertation Advisor Date  
Professor and Chair of Civil and Environmental Engineering, NJIT

---

Dr. Methi Wecharatana, Committee Member Date  
Professor of Civil and Environmental Engineering, NJIT

---

Dr. John R. Schuring, Committee Member Date  
Professor of Civil and Environmental Engineering, NJIT

---

Dr. Dorairaja Raghu, Committee Member Date  
Professor Emeritus, Civil and Environmental Engineering, NJIT

---

Dr. Wei Wang, Committee Member Date  
President, UrbanTech Consulting Engineering, New York, NY

## BIOGRAPHICAL SKETCH

**Author:** Mehdi Zarei  
**Degree:** Doctor of Philosophy  
**Date:** January 2016

### **Undergraduate and Graduate Education:**

- Doctor of Philosophy in Civil Engineering,  
New Jersey Institute of Technology, Newark, NJ, 2016
- Master of Science in Civil Engineering (Hydraulic Structures)  
Sharif University of Technology, Tehran, Iran, 2009
- Bachelor of Science in Civil Engineering  
Isfahan University of Technology, Isfahan, Iran, 2007

**Major:** Civil Engineering

### **Publications:**

Majdi, Y., Hsu, C.T.T. and Zarei, M. (2014), "Finite Element Modeling of Composite Floors with Cold-formed Steel and Concrete Slab", *Journal of Engineering Structures*, 77, 63-68.



*To my devoted parents  
and  
my loving wife*

*In Memory of  
Dr. C.T.T. Hsu  
1941-2014*

## ACKNOWLEDGMENT

I wish to express my deepest gratitude to my advisor, Professor C. T. Thomas Hsu, for his guidance, encouragement, and help throughout the course of this research and dissertation. He was a true scholar and a great gentleman. It was an honor to work with him on this dissertation. The author is also grateful to the members of his dissertation committee, Professor Methi Wecharatana, Professor John Schuring, Professor Dorairaja Raghu, and Dr. Wei Wang for their helpful evaluations and valuable suggestions.

The graduate assistantship received from the Department of Civil and Environmental Engineering is greatly appreciated. Furthermore, the author wishes to specifically thank Dr. Taha F. Marhaba, the chair of the Department, for his continuous support of this research.

Appreciation is expressed to my friends, Dr. Yazdan Majdi and Dr. Frank Golon for their help, advice and idea exchange regarding my research work. The author also wishes to thank Mr. Scott Cavanaugh for English proofreading of this dissertation and Mr. Andrew R. Flory, a staff of the Structural Concrete Laboratory at NJIT, for his assistance in the experiment.

Finally, I would like to deeply thank my parents, Narges and Majid, and express my love to my wife, Mahnaz, for their continuous support and understanding during all these years.

## TABLE OF CONTENTS

Chapter	Page
1 PRELIMINARIES AND LITERATURE REVIEW.....	1
1.1 Introduction .....	1
1.2 Description of the Proposed Research .....	7
1.2.1 Research Objectives .....	7
1.2.2 Research Significance .....	8
1.3 Literature Review.....	9
1.3.1 Concrete Columns Retrofitted with FRP or CFRP.....	9
1.3.2 High Strength Concrete Columns.....	22
1.4 Summary of Literature Review.....	28
2 BEHAVIOR OF NSC COLUMNS WITH CFRP.....	29
2.1 Introduction.....	29
2.2 Moment-Curvature Diagram of Concrete Sections.....	29
2.3 Material Models.....	33
2.3.1 Stress-Strain Model for Steel.....	33
2.3.2 Stress-Strain Model for Plain Concrete.....	34
2.3.3 Stress-Strain Model for Concrete Confined with FRP.....	35
2.4 Experimental Study.....	38
2.4.1 Moment-Curvature of the Experiment Column Section.....	40
2.5 Monotonic and Cyclic Pushover Analysis.....	43

**TABLE OF CONTENTS**  
**(Continued)**

<b>Chapter</b>	<b>Page</b>
3 EXPERIMENTAL PROGRAM.....	51
3.1 Introduction.....	51
3.2 Experimental Scheme.....	51
3.2.1 Design of Concrete Columns.....	51
3.2.2 Materials.....	52
3.2.3 Cast and Cure of the Concrete Columns.....	54
3.2.4 Experimental Setup.....	56
3.2.5 Test Procedures.....	60
3.3 Results and Discussions.....	67
3.3.1 Analysis of Test Results.....	67
4 ANALYSIS OF RC CONCRETE COLUMNS UNDER AXIAL LOADING WITH BIDIRECTIONAL ECCENTRICITIES.....	71
4.1 Introduction.....	71
4.2 Analysis Strategies.....	71
4.2.1 Description of Column Analysis.....	71
4.2.2 Idealized Stress-Strain Relations for Column Analysis.....	73
4.2.3 Extended Finite Segment Method for Analysis.....	82
4.2.4 Incremental Procedure and Flowchart.....	95
4.2.5 Accuracy and Convergence.....	97
4.3 Procedure of Numerical Analysis.....	100

**TABLE OF CONTENTS**  
**(Continued)**

<b>Chapter</b>	<b>Page</b>
4.4 Comparison of Experimental and Analytical Results.....	102
5 CONCLUSIONS.....	108
APPENDIX A STRESS-STRAIN CURVES OF STEEL BARS.....	111
APPENDIX B STRAIN-POSITION CURVES FOR COLUMN SPECIMENS	114
APPENDIX C LOAD-DEFLECTION CURVES OF COLUMN SPECIMENS	121
APPENDIX D ANALYTICAL LOAD-DEFLECTION AND MOMENT- CURVATURE CURVES.....	128
APPENDIX E COMPUTATIONAL PROCESS FLOWCHART.....	147
REFERENCES.....	148

## LIST OF TABLES

<b>Table</b>	<b>Page</b>
2.1 Summary of Column Specifications and Details.....	39
3.1 Mix Design of Concrete Columns.....	52
3.2 Test Outline of Column Specimens.....	55
3.3 Condition of Column Specimens at Failure.....	66
3.4 Experimental Results of Test Columns.....	70
4.1 Maximum Axial Load and Corresponding Deflection Results.....	107
4.2 Maximum Moment Results.....	107

## LIST OF FIGURES

Figure	Page
1.1 Test setup, Saadatmanesh, Ehsani, & Jin.....	12
1.2 Load-displacement responses of the first column before repair, Saadatmanesh, Ehsani, and Jin.....	13
1.3 Load-displacement responses of the first column after repair.....	14
1.4 Details of test specimen and test setup, Sheikh and Yau.....	17
1.5 Details of test specimen by, a) Sadeghian, Rahai, and Ehsani, b) Bibsy and Ranger.....	21
1.6 Configuration used to apply eccentric load, Sarkeret and Rangan.....	25
2.1 Whitney stress block.....	30
2.2 Real stress block.....	31
2.3 Section strain and stress distribution for concrete and steel.....	32
2.4 Steel stress-strain relationship.....	34
2.5 Stress-strain model for unconfined concrete.....	35
2.6 Schematic Lam and Teng's stress-strain model for FRP-confined concrete.....	38
2.7 Test column geometry and reinforcement: (a) Specimen 1, column in double bending; (b) Specimen 2, cantilever column.....	39
2.8 Stress-strain relationship of Column #1's concrete with and without a CFRP jacket.....	41
2.9 Moment-curvature for Column #1's section with and without a CFRP jacket...	41
2.10 Stress-strain relationship of Column #2's concrete with and without a CFRP jacket.....	42
2.11 Moment-curvature for Column #2's section with and without a CFRP jacket...	42

**LIST OF FIGURES**  
**(Continued)**

<b>Figure</b>	<b>Page</b>
2.12 Monotonic load-displacement response of column #1.....	44
2.13 Cyclic load-displacement response of column #1 without CFRP.....	44
2.14 Cyclic load-displacement response of column #1 with CFRP.....	45
2.15 Monotonic load-displacement response of column #2.....	45
2.16 Cyclic load-displacement response of column #2 without CFRP.....	46
2.17 Cyclic load-displacement response of column #2 with CFRP.....	46
2.18 Load-displacement response of column #1 without CFRP.....	47
2.19 Load-displacement response of column #1 with CFRP.....	47
2.20 Load-displacement response of column #2 without CFRP.....	48
2.21 Load-displacement response of column #2 with CFRP.....	48
3.1 Steel reinforcement for test columns.....	53
3.2 Column configuration.....	54
3.3 Wooden forms used for the test columns.....	56
3.4 Test setup.....	58
3.5 Arrangement of mechanical strain gauges.....	59
3.6 Failure of column C1.....	60
3.7 Failure of column C2.....	61
3.8 Failure of column C3.....	62
3.9 Failure of column C4.....	63
3.10 Failure of column C5.....	64



**LIST OF FIGURES**  
(Continued)

<b>Figure</b>	<b>Page</b>
3.11 Failure of column C6.....	65
3.12 Final conditions of column specimens.....	66
3.13 Typical load-vertical deflection curve for column C5.....	68
3.14 Typical load-deflection curves for column C5.....	69
3.15 Typical strain-position curve for column C5 in X direction.....	69
3.16 Envelope curves for unconfined and confined HSC.....	75
3.17 Plastic strain in the low strain range.....	78
3.18 Plastic strain in the intermediate and high-strain range.....	79
4.4 Reloading branches.....	80
4.5 Deterioration in tensile concrete strength due to prior compression loading.....	81
4.6 Idealized cyclic stress-strain curve for steel.....	82
4.7 Cross section and coordinate system.....	83
4.8 Strain plane of combined biaxial bending and axial load.....	85
4.9 Column divided into $n$ segments.....	88
4.10 Cross section of slender column for computer analysis.....	102
4.11 Comparison of load-vertical deflection curves for column C6.....	103
4.12 Comparison of load-deflection curves in the X-direction for column C6.....	103
4.13 Comparison of load-deflection curves in the Y-direction for column C6.....	104
4.14 Moment-curvature curve in the X-direction for column C6.....	104

**LIST OF FIGURES**  
**(Continued)**

<b>Figure</b>	<b>Page</b>
A.1 Stress-Strain curve of No. 3 bar (test1).....	112
A.2 Stress-Strain curve of No. 3 bar (test2).....	112
A.3 Stress-Strain curve of No. 3 bar (test3).....	113
B.1 Strain-position curve for control column C1 in the X direction.....	115
B.2 Strain-position curve for control column C1 in the Y direction.....	115
B.3 Strain-position curve for control column C2 in the X direction.....	116
B.4 Strain-position curve for control column C2 in the Y direction.....	116
B.5 Strain-position curve for control column C3 in the X direction.....	117
B.6 Strain-position curve for control column C3 in the Y direction.....	117
B.7 Strain-position curve for control column C4 in the X direction.....	118
B.8 Strain-position curve for control column C4 in the Y direction.....	118
B.9 Strain-position curve for control column C5 in the X direction.....	119
B.10 Strain-position curve for control column C5 in the Y direction.....	119
B.11 Strain-position curve for control column C6 in the X direction.....	120
B.12 Strain-position curve for control column C6 in the Y direction.....	120
C.1 Experimental load-vertical deflection for column C1.....	122
C.2 Experimental load-vertical deflection for column C2.....	122
C.3 Experimental load-vertical deflection for column C3.....	123
C.4 Experimental load-vertical deflection for column C4.....	123
C.5 Experimental load-vertical deflection for column C5.....	124

**LIST OF FIGURES**  
(Continued)

<b>Figure</b>	<b>Page</b>
C.6 Experimental load-vertical deflection for column C6.....	124
C.7 Experimental load-deflection in the X direction for column C1.....	125
C.8 Experimental load-deflection in the X direction for column C2.....	125
C.9 Experimental load-deflection in the X direction for column C3.....	126
C.10 Experimental load-deflection in the X direction for column C4.....	126
C.11 Experimental load-deflection in the X direction for column C5.....	127
C.12 Experimental load-deflection in the X direction for column C6.....	127
D.1 Analytical load-vertical deflection for column C1.....	129
D.2 Analytical load-vertical deflection for column C2.....	129
D.3 Analytical load-vertical deflection for column C3.....	130
D.4 Analytical load-vertical deflection for column C4.....	130
D.5 Analytical load-vertical deflection for column C5.....	131
D.6 Analytical load-vertical deflection for column C6.....	131
D.7 Analytical load-deflection in the X direction for column C1.....	132
D.8 Analytical load-deflection in the X direction for column C2.....	132
D.9 Analytical load-deflection in the X direction for column C3.....	133
D.10 Analytical load-deflection in the X direction for column C4.....	133
D.11 Analytical load-deflection in the X direction for column C5.....	134
D.12 Analytical load-deflection in the X direction for column C6.....	134

**LIST OF FIGURES**  
**(Continued)**

<b>Figure</b>	<b>Page</b>
D.13 Analytical moment-curvature curve at X-direction for column C1.....	135
D.14 Analytical moment-curvature curve at X-direction for column C2.....	135
D.15 Analytical moment-curvature curve at X-direction for column C3.....	136
D.16 Analytical moment-curvature curve at X-direction for column C4.....	136
D.17 Analytical moment-curvature curve at X-direction for column C5.....	137
D.18 Analytical moment-curvature curve at X-direction for column C6.....	137
D.19 Load-vertical deflection for column C1.....	138
D.20 Load-vertical deflection for column C2.....	138
D.21 Load-vertical deflection for column C3.....	139
D.22 Load-vertical deflection for column C4.....	139
D.23 Load-vertical deflection for column C5.....	140
D.24 Load-deflection in the X direction for column C1.....	141
D.25 Load-deflection in the X direction for column C2.....	141
D.26 Load-deflection in the X direction for column C3.....	142
D.27 Load-deflection in the X direction for column C4.....	142
D.28 Load-deflection in the X direction for column C5.....	143
D.29 Moment-curvature curve at X-direction for column C1.....	144
D.30 Moment-curvature curve at X-direction for column C2.....	144
D.31 Moment-curvature curve at X-direction for column C3.....	145

**LIST OF FIGURES**  
**(Continued)**

<b>Figure</b>	<b>Page</b>
D.32 Moment-curvature curve at X-direction for column C4.....	145
D.33 Moment-curvature curve at X-direction for column C5.....	146

## **CHAPTER 1**

### **PRELIMINARIES AND LITERATURE REVIEW**

#### **1.1 Introduction**

A large amount of research has been done in conjunction with the nonlinear behavior of reinforced concrete members for many years. Due to the locations of the structural members, the various framing of structures and the nature of the applied loads, many members are subjected to combined biaxial bending and axial compression. In the case of most structural members, reinforced concrete members are subjected to two main types of load, dead load and live load. For any member, the dead load is present throughout the life of the structure and can be considered to be constant. However, this is not the case for live load which has a cyclic form during the life of the structure. The behavior of any reinforced concrete column depends on many parameters including the material properties, section geometry, and history of moment and/or axial load to which the column is subjected.

The behavior of concrete is dependent upon its load history. In most cases, quantitatively accurate predictions on the load-deformation history up to and beyond the ultimate load remain difficult to obtain. The highly nonlinear nature of the concrete stress-strain relationship under a cyclic loading cannot be easily described by mathematical formulas. Although a considerable amount of effort has been focused on the development of a concrete model under cyclic compressive loading, most original concrete models cannot be incorporated into the analysis of reinforced concrete structures. A reliable and substantial cyclic stress-strain relationship is thus needed for the analysis of structures subjected to repetitive loadings.

For members where stability and secondary effects influence the strength, such as eccentrically loaded reinforced concrete (RC) columns, the changes in live load may have either a beneficial or detrimental effect on the strength of a member. Therefore the influence of repeated cycles of live load on column behavior is of interest in this study. The cyclic compressive loading with bidirectional eccentricities considered in this study is in the longitudinal (vertical) direction, and not in the transverse direction, with respect to the column axis. Such a loading and member might be present in a bridge substructure or building which is subjected to repetitive loadings. In both cases, changes in live load can occur frequently (Bahn, 1994).

In some cases, RC columns may not have been designed sufficiently or may have experienced excessive loads, such as those commonly associated with seismic activity. In these types of situations, the columns can be damaged. As a solution to these issues, Fiber Reinforced Polymer (FRP) or CFRP strengthening can be used for RC columns. Research has shown that closely spaced transverse reinforcement in the potential plastic hinge zone of concrete bridge columns substantially increases the compressive strength and effective ultimate compressive strain in the core concrete. The gain in the ultimate compressive strain significantly increases the ductility capacity of concrete columns. Thus, many recent research efforts on seismic retrofitting of concrete columns have been directed to providing additional confinement to the core concrete by means of external reinforcement (Saadatmanesh, Ehsani, & Jin, 1997). One recently developed and implemented strategy is to improve the strength of RC columns by wrapping them with CFRP. Fiber reinforced polymers (FRP) in the form of thin laminates or fabric, also known as composites, wrapped or epoxy-bonded to the tension side of a concrete member

have been used successfully in the aerospace and automotive industry for more than two decades. They are generally constructed of high performance fibers such as carbon, aramid, or glass, which are then placed in a resin matrix. By selecting among the many available fibers, geometry and polymers, the mechanical and durability properties can be tailored for particular application. This synthetic quality makes FRP a good choice for civil engineering application as well. The FRP offers the engineer an outstanding combination of properties, such as low weight (making them much easier to handle on site), resistance to corrosion, excellent mechanical strength and stiffness, and the ability of formation in very long length, thus eliminating the need for lapping at joints (Chen J. , 2005). Although FRP is a relatively expensive material compared to steel, it has been found that total rehabilitation project costs can be about 20% lower by using FRP in place of steel due to the savings in construction expenses (Muffi, Erki, & Jaeger, 1991). Tests have shown that externally bonded CFRP composites are able to increase the strength and displacement ductility significantly and double the hysteretic energy dissipation of reinforced concrete pier bents. Composite jackets can be very efficient for flexural plastic hinges even though the jackets themselves have a low modulus. The *in situ* tests have provided strong evidence that seismic retrofit using CFRP composites is a viable option for improving the seismic performance of bridges comprised of RC members. Furthermore, the retrofit implementation takes significantly less time to complete than other traditional methods, which is important in reducing the overall retrofit costs (Mirmiran & Shahawy, 1997) (Pantelides & Gergely, 2002) (Seible, Priestley, Hegemier, & Innamorato, 1997).



In recent years, the applications of high-strength concrete have increased, and high-strength concrete is now being used in many parts of the world. The growth has been possible as a result of recent developments in material technology and a demand for higher-strength concrete. The construction of Chicago's Water Tower Place and 311 South Wacker Drive concrete buildings would not have been possible without the development of high-strength concrete. The use of concrete superstructures in long span cable-stayed bridges such as the East Huntington, W.V., bridge over the Ohio River would not be possible without the availability of high-strength concrete (ACI Committee 363, 1992).

Generally, normal strength concrete is specified with a compressive strength of 3,000 psi to 6,000 psi. In recent years however, there is a trend to define it as a compressive strength of 3,000 psi to 8,000 psi. As the development of high strength concrete has been continued, the definition of high strength concrete varies in time and on a geographical basis (ACI Committee 363, 1992) due to lack of the standard criterion for high strength concrete (Chen D. , 1995). ACI committee 363 (1992) defines high-strength concrete as a concrete with a specified compressive strength for design of 6,000 psi (41MPa) or greater. At present, the definition doesn't include concrete made with exotic materials or techniques.

The most important properties of high strength concrete used in building code are its high compressive strength and its high modulus of elasticity. The strength of high strength concrete is affected by several main factors:

- Mixing proportioning and the selection of materials
- The method of curing
- The size of the specimen

The selection of materials and mixing proportions for high strength concrete are more crucial than those for normal strength concrete. Concrete is a two-phase composite material consisting of cement paste and aggregate. The methods of strength improvement of concrete can be classified into three parts: Strength improvement of cement matrix, aggregate, and bond between cement matrix and aggregate.

According to ACI Committee 363 (1992), the strength of the cement matrix is based on the strength of the hydration structure and the porosity of the matrix. The increase of porosity will reduce the strength of the cement matrix. Because porosity increases with increasing water to cement ratio, high strength concrete generally has a low water-cement ratio. Therefore, reducing the water to cement ratio and adding other chemical admixtures are methods of attaining high strength concrete. Chemical admixtures, such as superplasticizers and water reducing products have been widely used in attaining high strength concrete. Silica fume has also been used to improve the strength of the cement matrix in a ultra-high-strength concrete with compressive strength over 20,000 psi.

As a heterogeneous material, the properties of concrete depend on both the properties of the individual component and the properties of the combined material. The quality and type of aggregate have a significant effect on the strength and behavior of high strength concrete. The characteristics of coarse aggregate, such as bond potential with the cement paste and low water absorption capacity, are a very important consideration in the production of high strength concrete.

The methods of curing and the curing age are also important factors in developing the strength of concrete. Curing is mainly to promote the hydration of the cement, and is

extremely important in attaining a high strength concrete. The strength of concrete increases with the increase of its curing age. This has been proven by many researchers.

Due to special properties such as high strength and high elastic modulus, high strength concrete is often used in the design and construction of high-rise buildings in order to achieve greater heights while reducing the total weight of concrete needed by reducing the sizes of column cross sections. Its high elastic modulus can also reduce deflections as well as creep deformation. The brittle property can be partly overcome by adding fibers and/or tie confinement. It has been shown that the addition of fibers to concrete increases the materials ductility and fatigue strength. Due to the higher amount of cement used to develop high strength concrete, it is inherently more resistant to chemical deterioration (Chen D. , 1995).

## 1.2 Description of the Proposed Research

### 1.2.1 Research Objectives

In this study, the behavior of concrete columns with and without CFRP jackets under constant axial load and variable lateral load is studied. A computer code will be developed to predict the moment-curvature diagram for concrete sections wrapped with CFRP. The moment-curvature diagrams for sections with different properties will be used in the finite element computer software SAP2000 to study the behavior of concrete columns.

Secondly, tests on six four-foot-long square reinforced high-strength concrete columns under combined cyclical biaxial bending and axial compression will be performed. The displacement control loading and pinned-ended conditions will be used. The experimental ultimate load and load-deflection curves will be attained as well as discrete curvature readings.

Finally, a non-linear computer analysis of slender reinforced high-strength concrete columns under combined cyclical biaxial bending and axial load will be developed. Both material and geometrical nonlinearity will be included in the computer analysis. The analysis procedures developed will also be applicable for any column cross section geometry. The computer analysis will evaluate the complete behavior of the load-deflection and moment-curvature characteristics for cyclical biaxial loaded slender reinforced HSC columns with square sections. The presented computer analysis results will be compared with the experimental data.

### 1.2.2 Research Significance

An accurate and rational analysis of reinforced concrete (R/C) structures requires satisfactory modeling of the behavior of concrete. The behavior of concrete is dependent upon its load history. Since the applications and usage of RC short and slender columns with CFRP has increased during past decades, behavior of these structural members under cyclical loading should be studied so that designs can be more efficiently performed and can result in more reliable structures. The proposed method will be significant because a broad range of CFRP wrapped concrete column behaviors from zero loading to the rupture point of the column under cyclical loading will be analyzed.

The behavior of reinforced high-strength concrete columns having various properties and subjected to a variety of loading conditions has been the subject of considerable investigation. Despite this, there are still several important research topics which have been relatively unexplored. Of particular significance in the areas of unexplored topics are the factors affecting the HSC column behavior under cyclic loading. There are not any published experimental and theoretical studies of the cyclic axial loading on slender high-strength concrete columns subjected to biaxial bending. It should be noted that the cyclic compressive load with bidirectional eccentricities considered in this study is in the longitudinal direction, and not in the transverse direction, with respect to the column axis.

For the present experimental study, six four-foot-long HSC columns were tested under cyclic axial compression with bidirectional eccentricities. The main parameter of the column test was the bidirectional eccentricity. Ultimate strength, load-deflection and moment-curvature characteristics of HSC columns under cyclic axial load with double

eccentricities were examined. Furthermore, a computer model based on the finite segment method was developed here to simulate the behavior of high-strength concrete columns under combined biaxial bending and cyclic axial compression. In the previous finite segment models in studies by others, the effect of first derivation of the deflection function was neglected in formulation of the computer code. In the present study, however, this term in the curvature equation has not been neglected.

### **1.3 Literature Review**

#### **1.3.1 Concrete Columns Retrofitted with FRP or CFRP**

The usage of carbon fiber reinforced polymer (CFRP) has increased significantly since it was first used in 1980s. CFRP has been utilized to retrofit existing RC members which do not meeting current code requirements or deficient/damaged members. The fact is that the strength of CFRP is high and it can be easily formed into every shape. Matsuda, Satu, Fujiwara, and Higashira (1990) tested a system for retrofit of reinforced concrete a bridge pier using unidirectional carbon fiber sheets wrapped longitudinally and transversely in the potential plastic hinge region or in the region of the main reinforcing bar cutoff. The carbon fiber sheets were bonded to the concrete surface using epoxy resin.

Yamamoto (1992) performed two kinds of tests to clarify the effect of FRP strengthening on uniaxial concrete strength and shear-flexural behavior of existing RC columns. In that experiment FRP was made of either carbon or glass fiber and epoxy resin. Results showed that the uniaxial strength of FRP-strengthened concrete increases with the FRP strengthening ratio. Based on the experiments, empirical equations were

obtained for estimating the strength of FRP confined concrete. Also, a stress-strain relationship model for concrete confined with FRP was proposed.

Saadatmanesh, Ehsani, and Li (1994) proposed a wrapping system using glass fiber composite straps for column retrofit. Analytical models were presented to quantify the gain in both strength and ductility of concrete columns externally confined by means of high-strength fiber composite straps. A parametric study was conducted to examine the effects of various design parameters. The results indicate that the strength and ductility of concrete columns can be significantly increased by wrapping high-strength fiber composite straps around the columns. It was also concluded that percent increase in the maximum moment capacity is less than the percent increase in the ultimate axial load and ductility factor. This behavior is desirable in seismic strengthening of concrete columns because the retrofitted columns behave in a ductile flexural failure mode rather than a brittle shear mode of failure.

In another study, Saadatmanesh, Ehsani, and Jin (1996) conducted tests on reduced scale concrete specimens. In this experiment, the constant axial load was simulated with a pair of high strength steel rods which were bolted to the concrete floor. Also, an MTS hydraulic actuator was used to apply the reversing lateral forces. It was summarized that retrofitted columns developed very stable load-displacement hysteresis loops up to a high level of displacement ductility without evidence of significant structural deterioration associated with the bond failure of lapped started bars or longitudinal reinforcement buckling.

Seible, Priestley, Hegemier, and Innamorato (1997) proposed carbon jacket design criteria for various seismic column failure modes; they also proposed the usage of

CFRP to retrofit RC columns with circular and rectangular cross sections with different reinforcement ratios and detailing. The carbon jacket designs were validated through large-scale bridge column model tests. It has been demonstrated that advanced composite column retrofit jacket systems can be effective structurally in improving the seismic response characteristics of substandard reinforced concrete columns. In their study, design models for the composite jackets show that for shear and lap splice retrofits the required jacket thickness decreases with increasing jacket modulus in the hoop direction. For flexural plastic hinge confinement, even lower-modulus jackets can be very efficient as long as they exhibit large failure strain capacities. The effectiveness and accuracy of the established design models were validated by large-scale bridge column model tests for the three possible column failure modes of shear, plastic-hinge confinement, and lap splice debonding for both circular- and rectangular column geometries with different levels of column reinforcement ratios.

Mirmiran and Shahawy (1997) compared the results from a series of uniaxial compression tests on concrete-filled FRP tubes with the available confinement models in the associated literature. The study indicates that those models generally result in overestimated strength and unsafe design. In their work, a total of thirty 152.5×305 mm (6×12 in.) cylindrical specimens were tested under uniaxial compression load, which included 24 concrete-filled FRP tubes with different layer thickness and six plain concrete specimens. For each experiment case, three LVDTs (linear variable displacement transducer) were equally spaced on the specimen at every 120° to measure the average axial strain. It was concluded in their paper that FRP curtails the dilation rate of the concrete core.



Saadatmanesh, Ehsani, and Jin (1997) conducted an investigation into the flexural behavior of earthquake-damaged reinforced concrete columns repaired with prefabricated fiber reinforced plastic (FRP) wraps. Four column specimens were tested to failure under reversed inelastic cyclic loading to a level that can be considered higher than would occur in a severe earthquake. Then, the columns were repaired with prefabricated FRP wraps and retested under simulated earthquake loading. **Figure 1.1** shows the testing frame. Hydraulic rams at the base of the specimens were used to apply a constant axial load of 445 kN (100 kips) to simulate the dead load. A typical loading sequence for one of the tested columns is shown in **Figure 1.2**. The loading cycles are divided into two phases: load control and displacement control. The load control phase is used up to yielding of the longitudinal bars; beyond that point, a displacement control loading sequence was used. In **Figures 1.2** and **1.3**,  $u$ , defined as the displacement ductility factor, is the ratio of the applied displacement at the top of the column over the displacement at first yield.

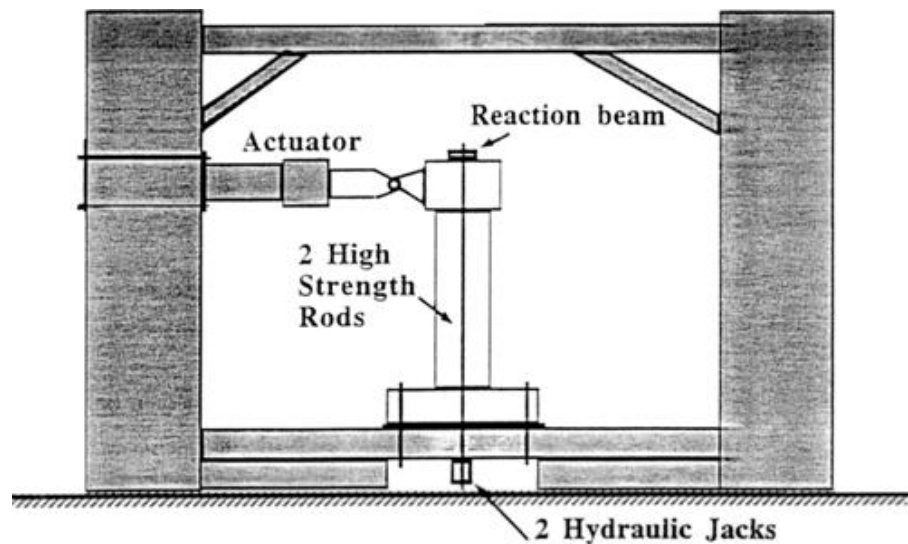


**Figure 1.1** Test setup.  
*Source: Saadatmanesh, Ehsani, & Jin (1997).*

The repair procedures consisted of chipping out loose concrete in the failure zones, filling the gap with fresh concrete, and using an active retrofit scheme. In this work, an active retrofit scheme consisted of wrapping the column with slightly oversized FRP straps and filling the gap between the column and the composite wrap with pressurized epoxy. The four repaired column specimens were subjected to the same loading sequences as those for the original columns approximately one week after the repair operation was completed. All repaired columns performed extremely well under the simulated earthquake loading. **Figure 1.2** and **Figure 1.3** show hysteresis loops for the first tested column before and after retrofitting with FRP. In these figures,  $\delta_y$  indicates lateral displacement at the top of the column at first yielding of the longitudinal steel reinforcing bars and  $V_u$  is the calculated lateral strength of the column.

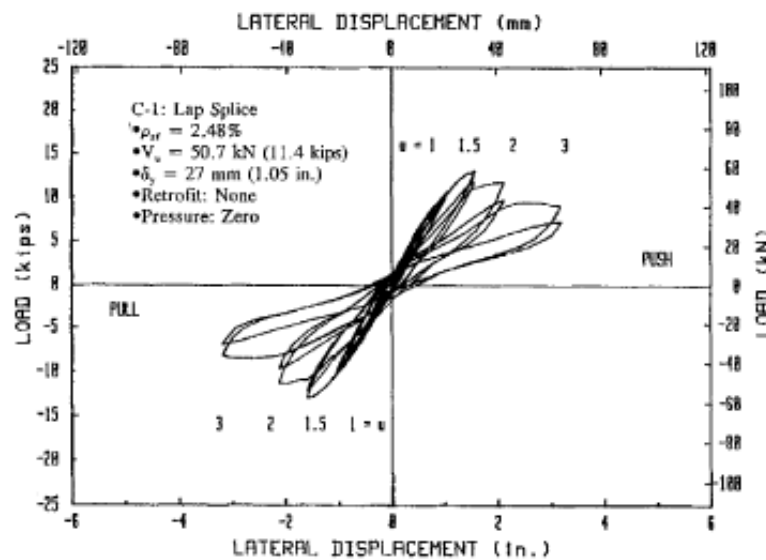


**Figure 1.2** Load-displacement responses of the first column before repair.  
Source: Saadatmanesh, Ehsani, & Jin (1997).

As can be seen in **Figure 1.2**, the lateral load drops significantly at displacement ductility level of  $u = 1.5$ . In subsequent load cycles, the resistance to lateral load drops

until failure has reached. **Figure 1.3** shows the hysteresis loops of the failed column. This column was wrapped with composite straps in the failure region, which consisted of a 635 mm (25 in.) column length located above the footing and measured from the top surface of the footing. Clear improvements in the response to cyclic lateral loads can be seen from this figure. At the displacement ductility level of  $u = 3$ , where the original column has failed, no structural degradation was observed in the repaired column. In fact, the response of the repaired column has improved over the original, undamaged column. The three remaining columns had similar or even more improved responses when compared to the behavior of the first tested column.

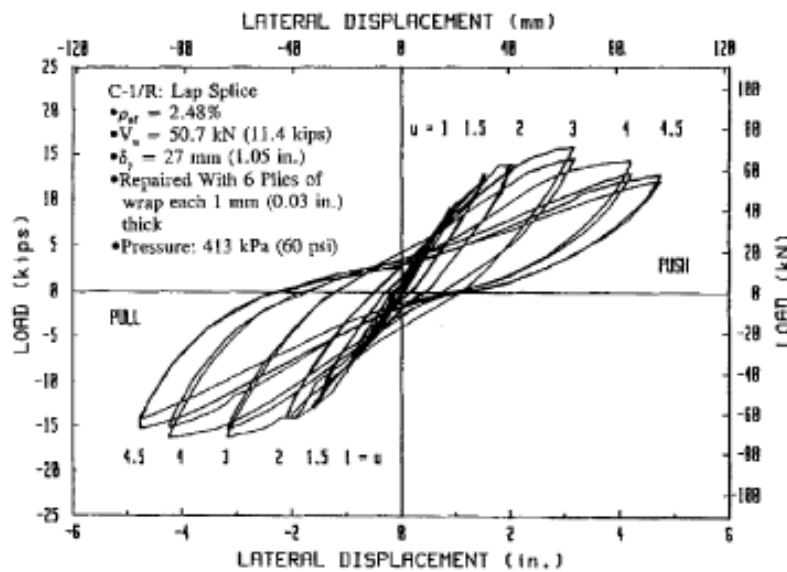


**Figure 1.3** Load-displacement responses of the first column after repair.  
 Source: Saadatmanesh, Ehsani, & Jin (1997).

Mirmiran, Samaan, El Chary, Mastrapa, and Pico (1998) studied the effect of shape, length, and bond on FRP confined concrete on over 100 specimens subjected to uniaxial compression. Their studies showed that square sections are less effective in confining concrete than their circular counterparts. Also, they concluded that the effect of

length-to-diameter ratios within the range from 2:1 through 5:1 is not significant for either strength or ductility of circular sections. Both eccentricities and strength reductions were within the limits prescribed by ACI 318-95 for tied columns. Additionally, their study found that adhesive bond does not affect load-carrying capacity of FRP-confined concrete. However, mechanical bond (shear connectors) significantly improves the performance of the section by distributing the confinement pressure more effectively around the circumference of the tube.

Rochette and Labossière (2000) performed research which yielded experimental results for short concrete column models wrapped with composite materials. The concrete sections, in this investigation, were confined with either carbon or aramid sheets. The effect of the confinement stiffness was examined, as well as the effect of rounding off the specimens corners. For a given number of wraps around a section (or a given transverse reinforcement ratio), the confinement effect was directly related to the shape of the section. It was concluded that the most effective confinements are obtained for circular sections. Also, excessive confinement may lead to very sudden and destructive compressive failures, which must be avoided.

Kachlakev (2002) developed a three-dimensional finite element model using ANSYS to examine the structural behavior of the Horsetail Creek Bridge in Oregon both before and after applying FRP laminates. In this study, truck loadings were applied to the finite elements (FE) bridge model at different locations to simulate the actual bridge tests. The comparisons between ANSYS predictions and field data were then made in terms of concrete strains. The FE bridge model analysis results were found to accurately predict the trends in the strains versus the various truck loading locations. In addition, effects of

FRP strengthening on the structural performance of the bridge were observed in the linear range. The trend in the strain results for the various truck positions obtained from the ANSYS model was similar to those gathered from the field test data. However, the ANSYS strain results differed from the field strain data from 60% to up to 130%. Kachlakev (2002) believes this discrepancy may be caused by inaccurate material properties for the concrete or an incorrect strain calibration in the field.

Pantelides and Gregely (2002) presented an analysis and design procedure for a CFRP composite seismic retrofit of a RC three-column bridge bent. The CFRP jacket was designed using performance-based criteria to provide a target displacement ductility based on seismic retrofit measures for the columns, bent cap, and bent cap-column joints. *In situ* quasi-static cyclic tests of a bent in the as-built condition and a bent retrofitted with the CFRP jacket were previously carried out in 1998. It has been found that the seismic retrofit was successful, and the bridge bent retrofitted with CFRP composites had reached a displacement ductility level in excess of the target ductility and double the hysteretic energy dissipation of the as-built bent. A description of the CFRP composite layout and validation of the design assumptions from the experimental results was also presented in this study.

Sheikh and Yau (2002) presented results from an experimental program in which twelve 356 mm diameter and 1473 mm long columns were tested under both constant axial load and reversed cyclic lateral load, which was intended to simulate seismic loading. Each specimen consisted of a column cast integrally with a 510 x 760 x 810 mm stub that represented a beam-column joint area or a footing (**Figure 1.4**).

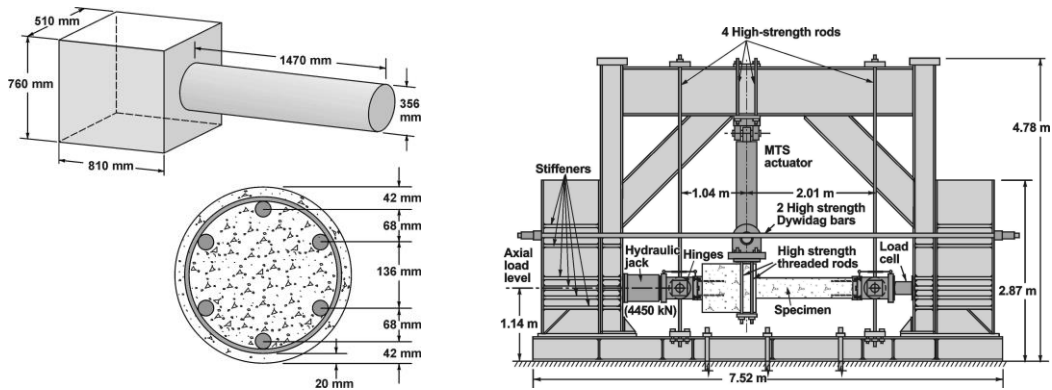


**Figure 1.4** Details of test specimen and test setup.

*Source: Sheikh and Yau (2002).*

The test specimens were divided into three groups. The first group consisted of four columns that were conventionally reinforced with longitudinal and spiral steel reinforcement. The second group contained six reinforced concrete columns that were strengthened with CFRP or glass fiber-reinforced polymers (GFRP) before testing. The last group included two columns that were damaged to a certain extent, repaired with FRP under axial load, and then tested to failure. The main variables investigated were axial load level, spacing of spirals, thickness, and type of FRP. From the results of the tests, it was concluded that carbon and glass FRP can be used effectively to strengthen deficient columns such that their strengthened behavior under simulated earthquake loading matches or exceeds the performance of columns designed according to the seismic provisions of the 1999 ACI Code. The use of FRP was confirmed to significantly enhance the strength, ductility, and energy absorption capacity of columns.

An investigation into the long term behavior of FRP confined concrete columns was carried out by Naquib and Mirmiran (2002). Shrinkage, interface bond, creep, creep recovery, static, and reserve strength of a number of concrete-filled FRP tubes (CFFT) and fiber-wrapped concrete columns were measured. The study showed the shrinkage of

the concrete core in CFFT columns to be quite negligible. Bond strength at the interface of the concrete core and FRP tube was found to be lower than that in steel tubes, but still large enough to counteract the axial shrinkage of the concrete core.

A stress–strain model was formed for concrete confined by FRP wraps with fibers exclusively or predominantly in the hoop direction by Lam and Teng (2003). Although this model was simple, it captured all the main characteristics of the stress–strain behavior of concrete confined by different types of FRP.

Ye, Zhang, Zhao, and Feng (2003) tested eight specimens, including two strengthened after being loaded to the yield level to imitate strengthening with some damage and one strengthened under a sustained axial load to imitate strengthening under a service loading condition. The service loading condition consisted of constant axial load and lateral cyclic load and was used to investigate the seismic performance of RC columns strengthened with CFRP sheets. In this study, the ductility enhancement achieved with the confinement provided by the CFRP sheets was studied by reviewing the development and distribution of strain in the CFRP sheets. Moreover, an equivalent transverse reinforcement index was suggested in order to gain the amount of CFRP needed for the seismic strengthening of RC columns.

In an investigation by Harajli and Rteil (2004), seismic behavior of reinforced concrete columns confined with CFRP flexible sheets were evaluated based on experiments. To simulate gravity load design, the column reinforcement in all specimens was spliced at the column base. In this study, all specimens experienced significant slip of the column reinforcement and widening of one single crack located at the column-stub interface. Without confinement, the RC columns suffered significant deterioration of

bond resistance of the spliced reinforcement, accompanied with considerable reduction in strength and stiffness degradation in the initial few load cycles following yield. By confining a small percentage of the actual concrete column with CFRP sheets, the test specimens exhibited a reduction in bond deterioration, a considerable increase in the energy absorption and dissipation capabilities of the columns, and resulted in a significant improvement in seismic performance.

Conclusions drawn on the basis of test results for twenty concrete column specimens wrapped with FRP were presented in a paper by Bousias, Triantafillou, Fardis, Spathis, and O'Regan (2004). In this study, unretrofitted columns exhibited a gradual loss of lateral and axial load resistance during the cycles that led to failure. Following ultimate deformation the tested specimens retained most of their axial load capacity but retained very little lateral load capacity. During the test, retrofitted columns successfully supported constant axial and lateral load capacity up to ultimate deformation, at which point the test columns failed explosively by fracture of the FRP wrap. They concluded that increasing the number of CFRP layers from two to five does not materially improve member deformation capacity and strength.

In a study conducted by Sause, Harries, Walkup, Pessiki, and Ricles (2004) full-scale column specimens with details and loading conditions based on the columns from the prototype structures were built and tested under combined axial and lateral loads. They concluded that the use of CFRP jackets to confine the inelastic hinge region of nonductile square building columns greatly enhances the deformation capacity of these columns without significantly increasing their strength or lateral stiffness. A fiber model cross section analysis of the prototype columns was carried out to show that the



deformation capacity increases with increasing jacket thickness. The out-of-plane stiffness of CFRP jackets can be sufficient to provide lateral support to the longitudinal bars under large displacement ductility demands. Column failure resulting from deterioration of the compression zone and longitudinal bar buckling in the hinge region can be delayed by using jackets with greater stiffness.

In order to predict the stress-strain behavior of concrete confined by FRP wraps, Bisby, Dent, and Green (2005) evaluated various available analytical models by using a light of a large database of test results on FRP wrapped columns. Moreover, several of the existing stress-strain relationships were modified to provide the best fit to the experimental database for confined ultimate stress and strain.

An experimental program consisting of testing of four series of RC columns with discrete wrapping arrangements and one series of fully wrapped RC columns was conducted by Barros, Ferreira, and Varma (2008). In this study, monotonic and cyclic tests were performed. Furthermore, a constitutive model to simulate FRP-confined RC elements subjected to cyclic compressive loading was developed and incorporated into a computer program based on the finite element method. They concluded that the results of partially confined specimens were slightly lower than that of the fully confined specimens. However, partial confinement arrangements were easier and faster to apply than full confinement arrangements. The obtained stress-strain curves indicated that the curve corresponding to the monotonic test can be considered to envelope the curve of the cyclic test.

More experimental studies involving RC columns strengthened with CFRP have been performed from which it can be concluded that CFRP strengthening can enhance the

performance of both column strength and ductility. In all of these experiments by Wei, Wu, Guo, and Yi (2009), columns were subjected to either monotonic increasing axial load or constant axial load with uniaxial bending. **Figure 1.5** illustrates the test setup and strain gauges for the experiments being done by Sadeghian, Rahai, and Ehsani (2010) and Bibsy and Ranger (2010).

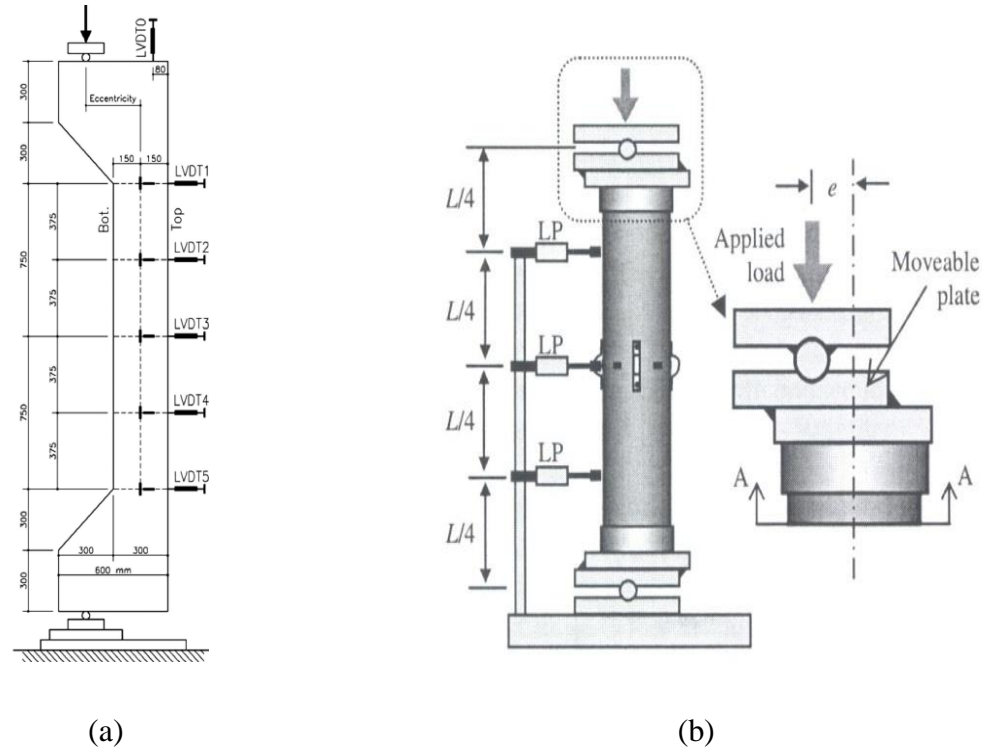


**Figure 1.5** Details of test specimen by a) Sadeghian, Rahai, and Ehsani (2010), b) Bibsy and Ranger (2010).

In recent years, Chen (2005) and Hsu and Punurai (2011) at New Jersey Institute of Technology (NJIT) have studied tension and compression strengthening of RC slender columns by CFRP composite fabrics under combined biaxial loading and axial compression. Based on their studies, strengthening the RC columns in both the longitudinal and transverse directions has a more significant effect on the strength and ductility of the column when compared to strengthening in one direction only.

### 1.3.2 High Strength Concrete Columns

The empirical results of a test program studying the effects of rectilinear confinement in high-strength concrete subjected to monotonically increasing compressive axial load was reported by Yong, Nour, and Nawy (1988). Twenty four columns made of high-strength concrete with compressive strength  $f_c'$  ranging from 12,130 to 13,560 psi (83.6 to 93.5 MPa) and rectilinearly confined with lateral ties and longitudinal reinforcement were tested. Additionally, the stress-strain behavior was studied with respect to the effects of the volumetric ratio of lateral ties, the thickness of the concrete cover, and the distribution of the longitudinal steel around the core perimeter. In this work, expected general improvements in the strength and ductility of the high-strength concrete with rectilinear confinement was observed. The lateral steel confinement in HSC was found to be not as effective as in low and normal-strength concrete. The stress-strain curve of rectilinearly confined high strength concrete was also presented in this study.

Hsu L. at NJIT (1992) performed tests on high strength concrete slender columns containing steel fibers under combined biaxial bending and axial compression load. Empirical equations were proposed to represent the complete stress-strain relationships of high strength and high strength fibrous concretes with compressive strength exceeding 10,000 psi. Various parameters were studied and their relationships were experimentally determined. Comparisons between the experimental and analytical results were found to have good agreement.

Results from four high-strength concrete specimens (HSC), three nonprismatic and one prismatic, tested under constant axial load and cyclic lateral loads (simulating earthquake forces) were presented and compared with similar specimens of normal

strength concrete (NSC) by Sheikh, Shah, and Khory (1994). In this study, the concrete strength varied between 4,500 and 8,500 psi (31 and 59 MPa). They concluded that the increase in the lateral steel reinforcement resulted in an almost proportional increase in the ductility and energy absorption capacity of confined high-strength concrete, just as in the case of normal strength concrete. For the same amount of tie steel, the flexural ductility of HSC columns was found to be significantly less than that of comparable NSC specimens. For the same level of axial load measured as a fraction of  $P_o$  (the ultimate axial load capacity), HSC and NSC columns behaved similarly in terms of energy absorption characteristics when the amount of tie steel in the columns was in proportion to the unconfined concrete strength.

Azizinamini, Kuska, Brungardt, and Hatfied (1994) investigated the flexural capacity and ductility of square high strength concrete columns. In this work, nine 2/3-scale test columns were subjected to constant axial loads and cyclic lateral loads. They concluded in this study that HSC [ $f_c'$  exceeding 10,000 psi (69MPa)] columns with applied axial load levels below 20 percent of the column's axial capacity that are designed based on the seismic provisions of ACI 318 (circa 1994) possess adequate curvature and displacement ductilities. Moreover, the ductility of the HSC columns decreased as the level of axial load increased and the volume of transverse reinforcement increased.

The following conclusions were drawn based on the research reported by Bae and Bayrak (2003). For the 224 HSC columns considered in this study, the use of ACI 318-02 specified stress block parameters resulted in progressively increasing overestimations of the moment capacities as the concrete strength increased. The fact that these

overestimations are systematical suggests that a physical phenomenon that does not affect NSC column capacity does affect HSC column capacity. This phenomenon was identified by the authors to be the early cover spalling in HSC columns. Having recognized the early cover spalling problem for HSC columns, new stress block parameters,  $\alpha_1$  and  $\beta_1$ , were proposed based on the reported research. The proposed parameters are as follows:

$$\alpha_1 = 0.85 - 0.004(f'_c - 70) \quad (f'_c \text{ in MPa}) \quad (1.1)$$

$$\text{where} \quad 0.67 \leq \alpha_1 \leq 0.85$$

$$\beta_1 = 0.85 - 0.004(f'_c - 30) \quad (f'_c \text{ in MPa}) \quad (1.2)$$

$$\text{where} \quad 0.67 \leq \beta_1 \leq 0.85$$

It should be noted that the proposed stress block parameters are based on the analysis in which  $\varepsilon_{cu} = 0.0025$  is employed for maximum useful compressive strain in concrete prior to early cover spalling in HSC ( $f'_c \geq 55$  MPa).

A paper which presents an experimental and analytical investigation of reinforced concrete columns subjected to unequal load eccentricities is authored by Sarker and Rangan (2003). The experimental results of 18 HSC columns and a computer-aided method to analyze reinforced concrete columns subjected to unequal load eccentricities were presented. **Figure 1.6** shows the configuration used to apply eccentric load.

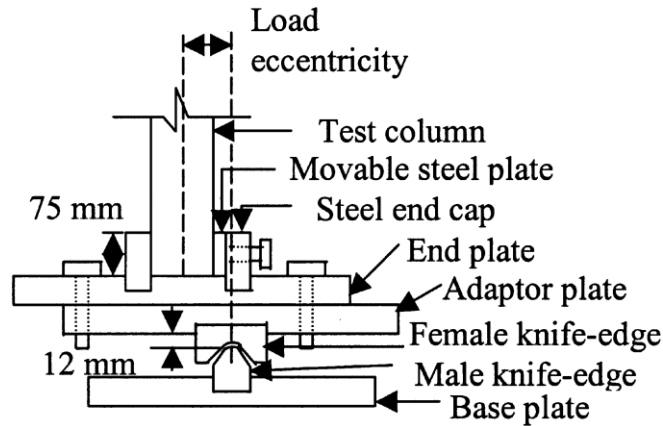


**Figure 1.6** Configuration used to apply eccentric load.

*Source: Sarkeret and Rangan (2003).*

In some cases of this experimental setup, uniaxial eccentricity varied at the top and bottom of the columns. For instance, for column C18, eccentricity in bottom of the column was 65 mm whereas the eccentricity in top of the column was -65 mm. It was found that analytical and test strengths correlated well in this investigation. The analytical method, therefore, was concluded by the authors to be useful to analyze reinforced concrete columns subjected to any combination of load eccentricities.

In a paper by Légerona and Paultre (2003), a new confinement model based on strain compatibility and transverse force equilibrium was presented. This approach, as suggested by the authors, was capable of predicting the effectiveness of transverse reinforcement, which is a key in modeling the behavior of high-strength concrete confined with high strength steel. The model was validated on test results from more than 200 circular and square large-scale columns tested under slow and fast concentric loading. In addition, results from about 50 square and circular large-scale columns tested under constant axial load and reversed cyclic bending were also used in the assessment of

the models adaptability to seismic-type loading. It was shown that all the hypotheses were in very good agreement with the experimental results.

Lu (2005) studied the stress-strain behavior of high strength concrete with and without steel fibers under uniaxial and triaxial compression. According to this research, under triaxial compression, there was no apparent advantage of steel fiber reinforced high strength concrete (SFHSC) over high strength concrete (HSC) in terms of triaxial strength, ductility and stress-strain behavior. The compressive median and the peak octahedral shear stress versus peak octahedral shear strain relationships for the two types of concrete can be expressed by a single expression. The results from the model analysis correlate with the experimental data fairly well under moderate confining pressures.

In an investigation by Pallarés, Bonet, Miguel, and Prada (2008), experimental research on high strength concrete columns subjected to compression and biaxial bending forces was presented. The considered parameters in this research were eccentricity, skew angle and slenderness of the test specimen, from which a total of 56 columns had been tested. The cross-sectional dimensions are  $200 \times 100$  mm, the lengths of the columns were 1, 2 and 3 m, and the average compression strength was 103 MPa (15 ksi).

To study the properties of high-strength concrete (HSC) circular columns confined by aramid fiber-reinforced polymer (AFRP) sheets under axial compression, a total of 60 specimens were tested by Wu, Wang, Yu, and Li (2009). In this study, the compressive strength of concrete, the number of AFRP layers, and the form of AFRP wrapping were presented. An analytical model to predict the stress–strain curves was also proposed based on the experimental results. Furthermore, a three-dimensional nonlinear finite element model with a Drucker–Prager plasticity model for the concrete core and an

elastic model for the AFRP sheets was developed using the finite-element code ANSYS. It was demonstrated that the strength and ductility of the columns with continuous AFRP wrapping were increased greatly. The strength of the columns with discontinuous AFRP wrapping was also increased, but the ductility was not always significantly increased. The analytical model and the finite-element model were validated against the experimental results.

A new concept was investigated in the study by Hadi and Zhao (2011) in order to reduce the cover spalling of high-strength concrete columns. To decrease the cover spalling, relatively cheap materials such as household fly screen and wire mesh were installed in the formwork of RC columns. Three materials were chosen in this study, and a total of 16 cylindrical specimens with a length of 36.4 in (925 mm) and a diameter of 8 in (205 mm) were cast and tested under concentric, eccentric, and pure bending loading. The testing results showed that the load-carrying capacity and ductility improved under both concentric and eccentric loading.

In an investigation by Ozbakkaloglu and Akin (2011) results of experimental tests of FRP-confined normal and high-strength concrete under axial compression were studied. A total of 24 aramid and carbon FRP-confined concrete cylinders with different concrete strengths and FRP jacket thicknesses were tested under monotonic and cyclic loading. They concluded that the residual plastic strain of FRP-confined concrete was linearly related to the unloading strain envelope, and this relationship did not appear to be influenced significantly by: i) the amount of confinement; ii) the type of FRP; and iii) the unconfined concrete strength. They also concluded that the presence of unloading/reloading cycles leads to an increase in the ultimate strength and strain of FRP-



confined concrete. Additionally, direct application of the existing FRP-confined NSC stress-strain models to FRP-confined HSC can lead to significant overestimation of the ultimate condition of FRP-confined HSC.

#### **1.4 Summary of Literature Review**

By studying the literature, it can be concluded that the behavioral analysis of cyclically loaded RC columns strengthened by CFRP composite fabrics requires further investigation. Additionally, the behavior of CFRP strengthened concrete columns under cyclic loading in biaxial directions has not been studied.

Analysis of both reinforced NSC columns and HSC columns wrapped with CFRP have been the subject of a number of research studies. Further, the application of CFRP on high-strength concrete columns can be found in the literature. Concrete columns in those works were subjected to monotonic axial load with unidirectional eccentricity. Therefore, there is a lack of studies with regard to the analysis of high-strength concrete columns under cyclic axial load and biaxial bending.

## **CHAPTER 2**

### **BEHAVIOR OF NSC COLUMNS WITH CFRP**

#### **2.1 Introduction**

In this chapter, a simplified method is introduced to study the behavior of concrete columns with and without CFRP jackets while subjected to constant axial load and variable lateral load. The lateral load will be applied in monotonic and cyclic form. This method can be utilized to analyze the strength and flexibility of concrete columns which are subject to considerable moment such as bridge substructure columns during earthquake events. To predict the behavior of concrete columns under monotonic and cyclic compressive loadings, a computer code has been developed to produce the moment-curvature diagram of any arbitrary concrete section. This code must be able to represent the general behavior of concrete columns based upon different stress-strain relationships so that sections with and without CFRP wraps can be analyzed. Then, the moment-curvature diagram can be input as a plastic hinge property in the commercial software package SAP2000 to study the behavior of concrete columns with different properties under monotonic and cyclic load patterns. The result of this method has been compared with test results which shows acceptable compliance with experimental results.

#### **2.2 Moment-Curvature Diagram of Concrete Sections**

With the development of performance-based design methods, there is an increasing need for simplified but reliable analytical tools capable of predicting the flexural behavior of reinforced concrete members. Design offices will be faced more and more with the need to predict the deformation capacity of concrete members. The most fundamental

requirement in predicting the moment curvature behavior of a flexural member is the knowledge of the behavior of its constituents (Srikanth, Rajesh Kumar, & Giri, 2007). Reinforced concrete design calculations normally assume a simple material model for the concrete and reinforcement to determine the moment capacity of a section. The Whitney stress block for concrete along with an elasto-plastic reinforcing steel behavior is the most widely used material model in American codes (**Figure 2.1**). However, the actual behavior of concrete is nonlinear and can be described by idealized stress-strain models (**Figure 2.2**).

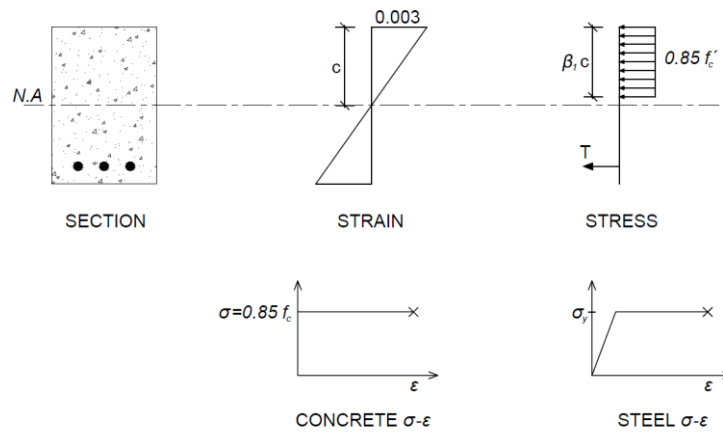


**Figure 2.1** Whitney stress block.

Moment curvature analysis is a method to accurately determine the load-deformation behavior of a concrete section using nonlinear material stress-strain relationships. For a given axial load there exists an extreme compression fiber strain and a section curvature ( $\phi = \epsilon/c$ ) at which the nonlinear stress distribution is in equilibrium with the applied axial load. A unique bending moment can be calculated at this section curvature from the stress distribution. The extreme concrete compression strain and section curvature can be iterated until a range of moment-curvature values are obtained.

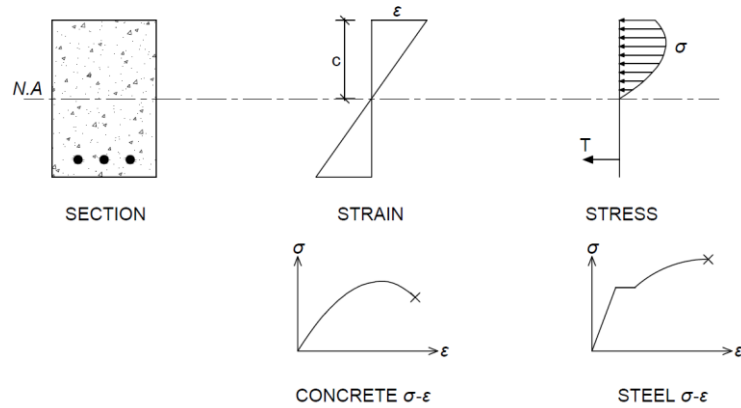


**Figure 2.2** Real stress block.

In deriving the expressions of the moments and curvatures for concrete sections with and without CFRP wrapping, the following assumptions are made:

1. Plane sections remain plane before and after bending.
2. The strain variation across the section is linear.
3. A bilinear stress-strain relationship is considered for steel in tension and compression.
4. The reinforcing steel is perfectly bonded to the concrete.
5. The effect of creep and any direct tension stresses due to shrinkage are neglected.
6. Shear deformation is neglected.

To determine the moment-curvature graph of a concrete section, a wide variety of extreme fiber concrete strains ( $\epsilon_c$ ) are selected to capture corresponding moments for each selected strain. These moment values are obtained by satisfying three basic relationships: equilibrium of forces, compatibility of strains, and the stress-strain relationship of steel and concrete.

Analysis is based on fiber modeling in which the section is divided into uniaxially stressed fibers along the longitudinal axis. This model has been used efficiently by many

in analysis of reinforced concrete columns subjected to different loading paths (Esmaily & Xiao, 2005). It is assumed that the stress in a fiber varies linearly and stress at the center of a fiber represents the fiber's equivalent stress. The stresses in concrete and steel fibers are determined from the stress-strain curves and are taken as the stress corresponding to the average strain of the fiber (Figure 2.3). Hence, utilizing a sufficient number of fibers for the compression zone of the concrete member will provide a more compatible compressive stress distribution with the assumed stress-strain model. This, consequently, will lead to more accurate results (Dundar, Tokgoz, Tanrikulu, & Baran, 2008).

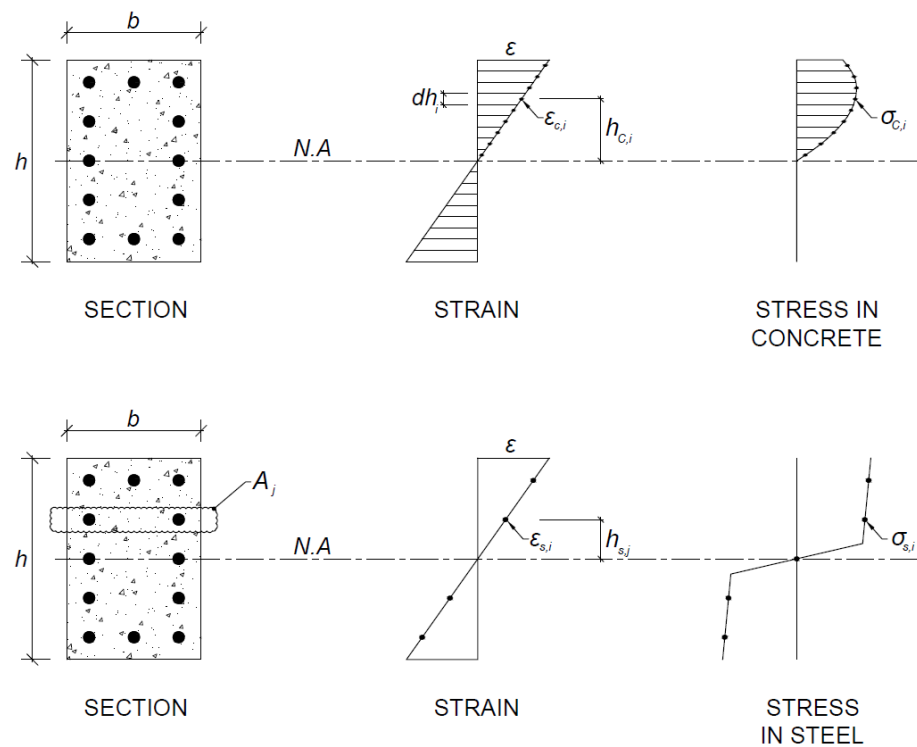


**Figure 2.3** Section strain and stress distribution for concrete and steel.

Section forces are determined from stresses and areas of the concrete and steel in each fiber, after performing iterations to satisfy equilibrium (Saadeghvaziri, 1997). The axial force and corresponding moments can be obtained as follows:

$$f_{c,i} = \sigma_{c,i} \times b \times dh_i \quad (2.1)$$

$$f_{s,j} = \sigma_{s,j} \times A_j \quad (2.2)$$

$$P = \sum_{i=1}^n f_{c,i} + \sum_{j=1}^k f_{s,j} \quad (2.3)$$

$$M = \sum_{i=1}^n f_{c,i} \times h_{c,i} + \sum_{j=1}^k f_{s,j} \times h_{s,j} \quad (2.4)$$

Where  $\sigma_{c,i}$  is the concrete stress in the  $i^{th}$  fiber,  $\sigma_{s,j}$  is the steel stress in the  $j^{th}$  row of reinforcement,  $b$  is the width of the section,  $dh_i$  is the height of the  $i^{th}$  fiber,  $A_j$  is the total area of the reinforcement in the  $j^{th}$  fiber,  $h_{c,i}$  is the distance of the  $i^{th}$  concrete fiber from the neural axis,  $h_{s,j}$  is the distance of the  $j^{th}$  row of reinforcement from the neutral axis,  $P$  is total axial load, and  $M$  is total moment of the section.

## 2.3 Material Models

### 2.3.1 Stress-Strain Model for Steel

A bilinear elastic-plastic material model is developed for the monotonic stress-strain relationship of steel. This model is detailed with 4 variables of  $f_y$ ,  $\varepsilon_y$ ,  $E$ , and  $E_p$  which are yield stress, yield strain, modulus of elasticity, and after yield slope, respectively.

**Figure 2.4** depicts the assumed stress-strain model for steel.

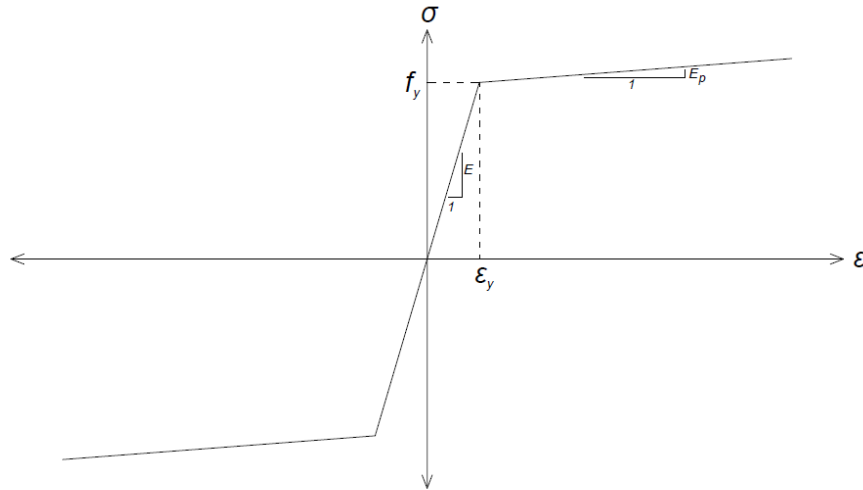


**Figure 2.4** Steel stress-strain relationship.

### 2.3.2 Stress-Strain Model for Plain Concrete

The model for the monotonic stress-strain relationship of concrete proposed by Carreira and Chu (1985) has been used for obtaining the moment-curvature diagram of the section. The numerical expression of this model is:

$$Y = \frac{\beta X}{\beta - 1 + X^\beta} \quad (2.3)$$

$$X = \frac{\varepsilon_c}{\varepsilon_o} \quad (2.4)$$

$$Y = \frac{f_c}{f'_c} \quad (2.5)$$

$$\beta = \frac{1}{1 - \frac{f'_c}{\varepsilon_o E_{it}}} \quad (2.6)$$

Where:

$\varepsilon_c$  = concrete strain

$f_c$  = concrete stress

$f'_c$  = maximum compressive strength of concrete

$\varepsilon_o$  = strain corresponding to peak stress,  $f'_c$

$\beta$  = material parameter

$E_{it}$  = initial tangent modulus of concrete, which is determined from the equation suggested in the ACI code (2011):

$$E_{it} = 57000\sqrt{f'_c} \quad (2.7)$$

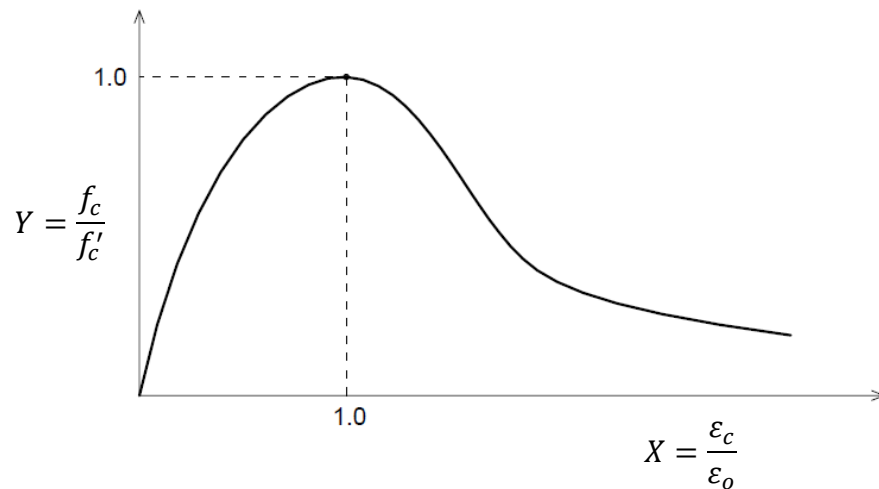


**Figure 2.5** Stress-strain model for unconfined concrete.

### 2.3.3 Stress-Strain Model for Concrete Confined with FRP

The design-oriented stress-strain model for FRP-confined concrete by Teng, Jiang, Lam, and Luo (2009) has been selected. This model is the result of a study conducted to refine the design-oriented stress-strain model originally established by Lam and Teng (2003) for FRP-confined concrete under axial compression based on an interpretation of test data and observations. This model is simple, which makes it suitable for direct use in design. Also, it captures all the main characteristics of the stress-strain behavior of concrete confined by different types of FRP. In the development of this model, a number of important issues were examined and resolved, including the actual hoop strains in FRP



jackets at ruptures, the sufficiency of FRP confinement for a significant strength enhancement, and the effect of jacket stiffness on the ultimate axial strain. It should be noted that this model is also applicable to stress-strain curves with a descending branch.

This model is described by the following expressions:

$$\rho_k = \frac{2E_{FRP}t}{(f'_{co}/\varepsilon_{co})D} \quad (2.8)$$

$$\rho_\varepsilon = \frac{\varepsilon_{h,rupt}}{\varepsilon_{co}} \quad (2.9)$$

where  $\rho_k$  is the confinement stiffness ratio which represents the stiffness of the FRP jacket relative to that of the concrete core and  $\rho_\varepsilon$  is the strain ratio which is a measure of the strain capacity of the FRP jacket. Additionally:  $E_{FRP}$  = elastic modulus of FRP in the hoop direction;  $t$  = thickness of FRP jacket;  $D$  = diameter of the confined concrete cylinder;  $f'_{co}$  = unconfined concrete strength;  $\varepsilon_{co}$  = corresponding axial strain to unconfined concrete strength;  $\varepsilon_{h,rupt}$  = hoop rupture strain of the FRP jacket.

The parabolic first portion and linear second portion of Lam and Teng's model is expressed as:

$$\sigma_c = \begin{cases} E_c \varepsilon_c - \frac{(E_c - E_2)^2}{4f'_{co}} \varepsilon_c^2 & (0 \leq \varepsilon_c \leq \varepsilon_t) \\ \begin{cases} f'_{co} + E_2 \varepsilon_c & \text{if } \rho_k \geq 0.01 \\ f'_{co} - \frac{f'_{co} - f'_{cu}}{\varepsilon_{cu} - \varepsilon_{co}} (\varepsilon_c - \varepsilon_{co}) & \text{if } \rho_k < 0.01 \end{cases} & (\varepsilon_t < \varepsilon_c \leq \varepsilon_{cu}) \end{cases} \quad (2.10)$$

where  $\sigma_c$  and  $\varepsilon_c$  = axial stress and the axial strain respectively;  $E_c$  = elastic modulus of unconfined concrete; and  $E_2$  = slope of the linear second portion. The parabolic first portion meets the linear second portion with a smooth transition at  $\varepsilon_t$ , which is given by

$$\varepsilon_t = \frac{2f'_{co}}{E_c - E_2} \quad (2.11)$$

The slope of the linear second portion  $E_2$  is given by

$$E_2 = \frac{f'_{cu} - f'_{co}}{\varepsilon_{cu}} \quad (2.12)$$

This model allows the use of test values or values specified by design codes for the elastic modulus of unconfined concrete  $E_c$ . Based on the ACI code, equation (2.7) can be used to estimate  $E_c$ .

The following equation is proposed to predict the ultimate axial strain  $\varepsilon_{cu}$  if the concrete is confined:

$$\frac{\varepsilon_{cu}}{\varepsilon_{co}} = 1.75 + 6.5\rho_k^{0.8}\rho_\varepsilon^{0.8} \quad (2.13)$$

where the strain at the unconfined concrete strength  $\varepsilon_{co}$  was taken to be 0.002.

This model's compressive strength equation,  $f'_{cu}$ , takes the following form:

$$\begin{aligned} \frac{f'_{cu}}{f'_{co}} &= 1 + 3.5(\rho_k - 0.01)\rho_\varepsilon && \text{if } \rho_k \geq 0.01 \\ \frac{f'_{cu}}{f'_{co}} &= 1 && \text{if } \rho_k < 0.01 \end{aligned} \quad (2.14)$$

**Figure 2.6** illustrates a schematic stress-strain model based on Lam and Teng's model.

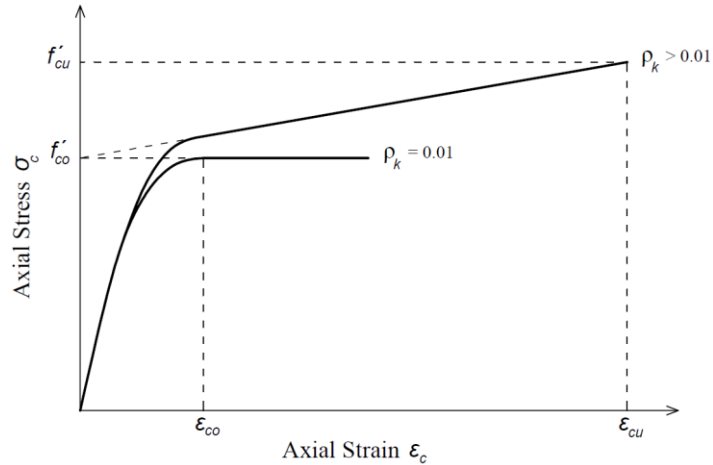


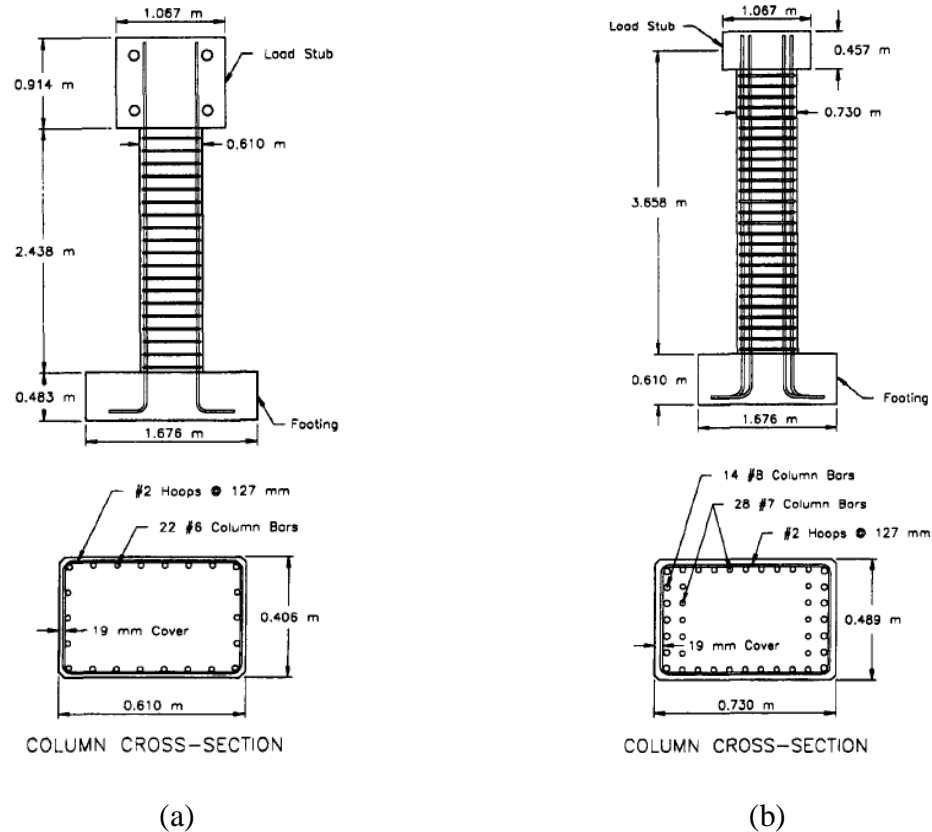
**Figure 2.6** Schematic Lam and Teng's stress-strain model for FRP-confined concrete.

## 2.4 Experimental Study

In a work by Seible, Priestley, Hegemier, and Innamorato (1997) the development, validation, and implementation of carbon fiber jackets as a retrofit system for reinforced concrete columns was described. This study included experimental results of circular and rectangular columns with variable carbon fiber thicknesses along the column height based on design models. The columns were loaded under constant axial load and monotonic and cyclic horizontal load at the tip of the column. Also, jacket design criteria for different seismic column failure modes were described. Large-scale bridge column models were tested and it was found that carbon fiber jacketing is effective in providing inelastic deformation capacity. The specimen geometry and reinforcement detailing are depicted in **Figure 2.7** while column section properties and jacket material properties are summarized in **Table 2.1**.

**Table 2.1** Summary of Column Specifications and Details

Element	Specification	Column #1	Column #2
Column geometry	Column height, $H$	2.438 m (96 in)	3.658 m (144 in)
	Shear span, $L$	1.219 m (48 in)	3.658 m (144 in)
	Column depth, $D$	0.610 m (24 in)	0.730 m (28.75 in)
	Column width, $B$	0.406 m (16 in)	0.489 m (19.25 in)
	Concrete cover, $cc$	19 mm (0.75 in)	19 mm (0.75 in)
	Concrete strength, $f_c'$	34.45 MPa (5 ksi)	34.45 MPa (5 ksi)
Longitudinal reinforcement	Bar diameter, $d_b$	22 x 19 mm (#6)	14 x 25 mm (#8) 28 x 22 mm (#7)
	Bar area, $A_s$	284 mm <sup>2</sup> (0.44 in <sup>2</sup> )	510 mm <sup>2</sup> (0.79 in <sup>2</sup> )
	Yield strength, $f_{sy}$	303.16 Mpa (44 ksi)	303.16 Mpa (44 ksi)
Column section properties	Axial load, $P$	507 kN (114 kip)	1,780 kN (400 kip)
	Moment capacity, $M_{yi}$	619 kN.m (457 kip.ft)	2,165 kN.m (1,597 kip.ft)
	Yield curvature, $\Phi_y$	$5.47e^{-3}$ 1/m ( $2.15e^{-4}$ 1/in)	$4.69e^{-3}$ 1/m ( $1.84e^{-4}$ 1/in)
	Neutral axis depth, $C_u$	116 mm (4.57 in)	208 mm (8.19 in)
Jacket material properties	Jacket modulus, $E_j$	124 Gpa (17,980 kip)	124 Gpa (17,980 kip)
	Ultimate strength, $f_{ju}$	1.3 GPa (188.5 kip)	1.3 GPa (188.5 kip)
	Ultimate strain, $\epsilon_{ju}$	1.0%	1.0%
	Jacket thickness, $t_j$	2.0 mm (0.0787 in)	10.2 mm (0.4016 in)

**Figure 2.7** Test column geometry and reinforcement: (a) Specimen 1, column in double bending; (b) Specimen 2, cantilever column.

Source: Seible, Priestley, Hegemier, and Innamorato (1997).

### 2.4.1 Moment-Curvature of the Experiment Column Section

In this section, concrete stress-strain curves of the columns which were tested by Seible, Priestley, Hegemier, and Innamorato (1997) have been depicted. These graphs include stress-strain behavior for both plain concrete and concrete confined with CFRP (**Figure 2.8, Figure 2.9, Figure 2.10, and Figure 2.11**).

Moment-curvature graphs for both column sections show that the CFRP jacket can enhance the flexibility and strength of the column. This enhancement is more pronounced for sections which are retrofitted with thicker layers of CFRP. Column #1 has a moment capacity of 483 kip-ft without CFRP jacket, whereas adding a CFRP jacket can increase this capacity to 714 kip-ft (48% increase in moment capacity). Column #2 without the CFRP jacket has a moment capacity equal to 1,522 kip-ft. This capacity is increased to 3,039 kip-ft (100% increase in moment capacity) when the section is wrapped with a 0.4 in (10 mm) thick layer of CFRP.

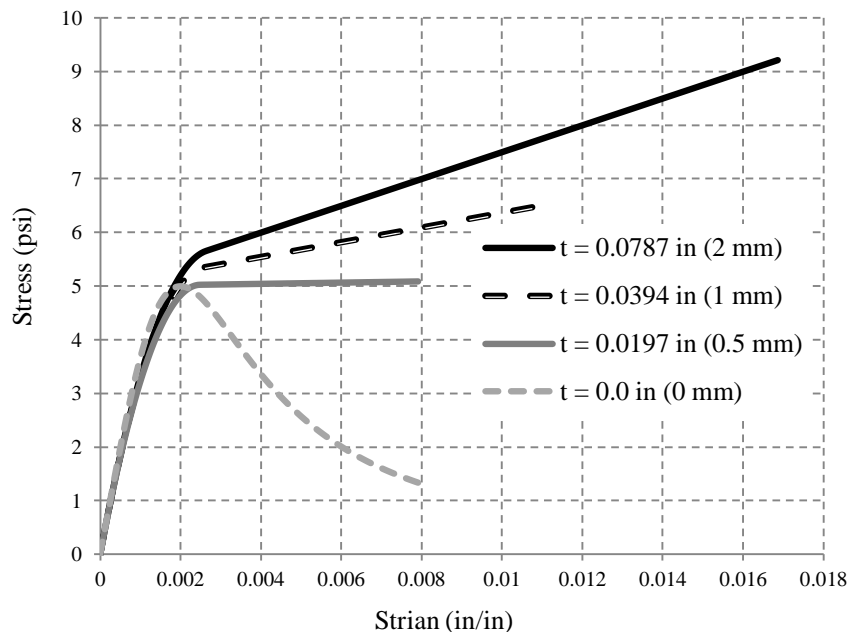


**Figure 2.8** Stress-strain relationship of Column #1's concrete with and without a CFRP jacket.

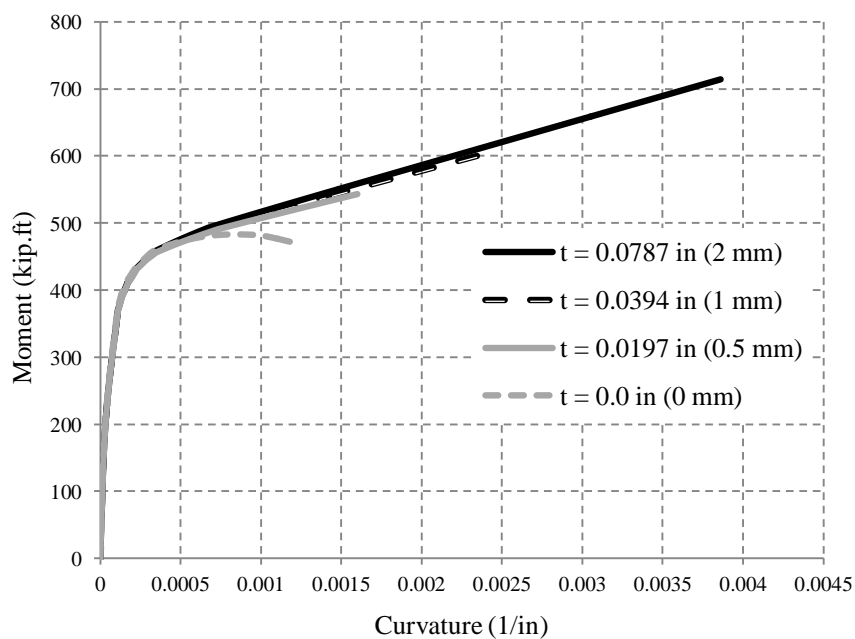


**Figure 2.9** Moment-curvature for Column #1's section with and without a CFRP jacket.

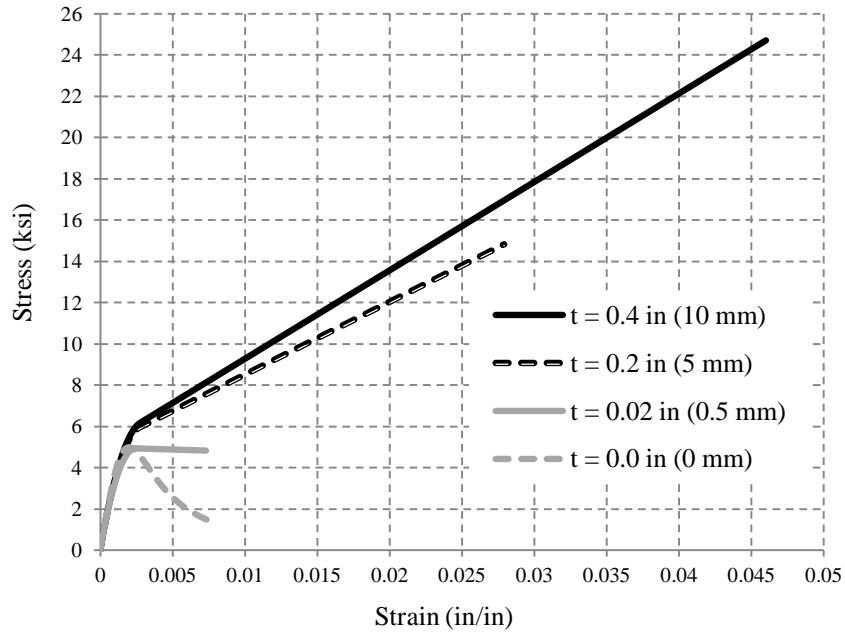


**Figure 2.10** Stress-strain relationship of Column #2's concrete with and without a CFRP jacket.

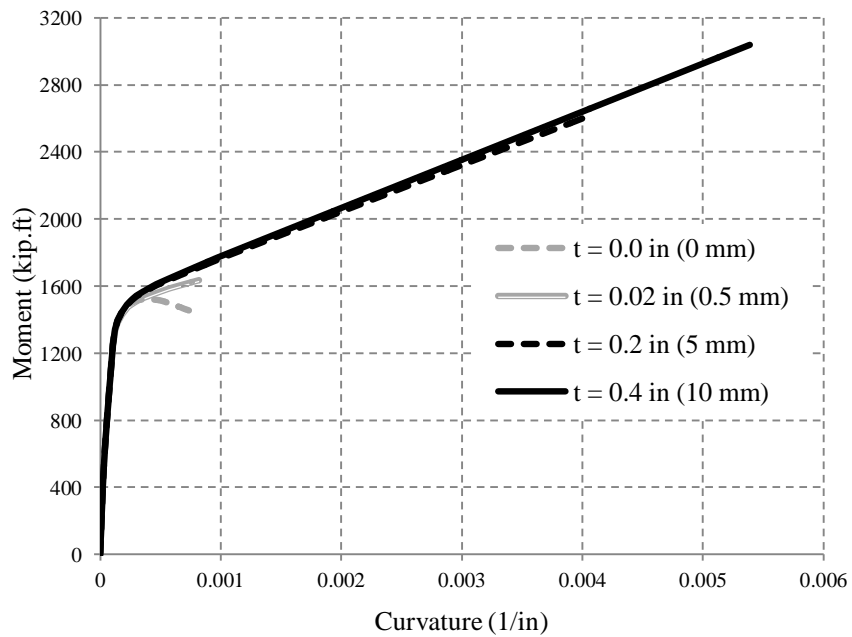


**Figure 2.11** Moment-curvature for Column #2's section with and without a CFRP jacket.

## 2.5 Monotonic and Cyclic Pushover Analysis

After obtaining the moment-curvature of column sections with and without CFRP, these graphs were input as plastic hinge properties in the commercial software package SAP2000 in order to study column behavior under constant axial load plus monotonic or cyclic lateral load applied at the top of the column. This behavior is shown with the mean of the load-displacement graph. The columns have been modeled in this software in accordance with the boundary conditions and loading applied in the tests done by Seible, Priestley, Hegemier, and Innamorato (1997). In the model, columns were divided into 10 segments. Division of the columns into segments facilitates the assignment of plastic hinge properties to the individual zone that yields first due to the maximum moment. Although tested columns are wrapped with CFRP jackets with different thicknesses along the full height of the column, the plastic hinge property is only assigned to one segment in the computer model in order to avoid convergence issues. Additionally, moment-curvature diagrams have been simplified with a bilinear graph rather than a curve prior to assignment as the plastic hinge property in the model. A second assumption is made regarding the unloading behavior of the columns in the second and fourth quadrants of load-displacement graph. In these quadrants, a line which connects the point with residual deformation and zero horizontal load to the point with zero deformation and intersection of “Y” axis represents the unloading behavior of the column. **Figure 2.12** to **Figure 2.17** illustrate test results for columns #1 and #2.



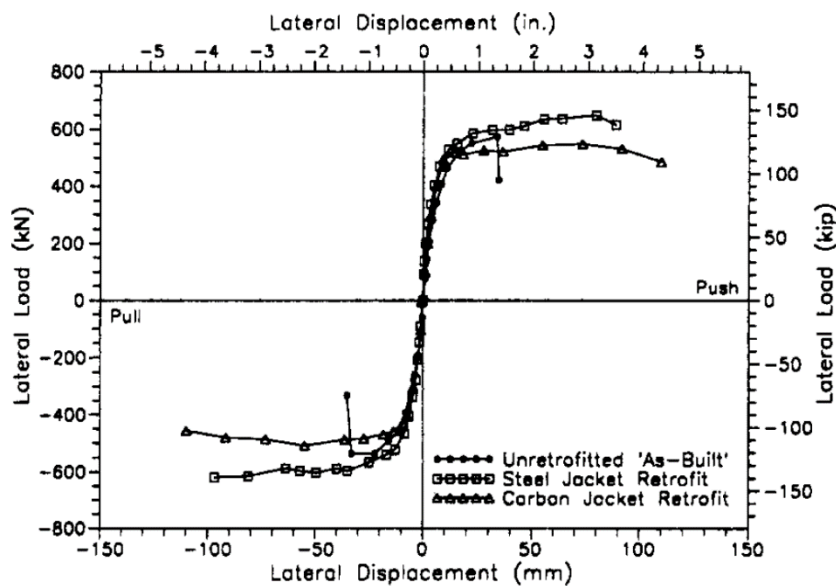


Figure 2.12 Monotonic load-displacement response of column #1.

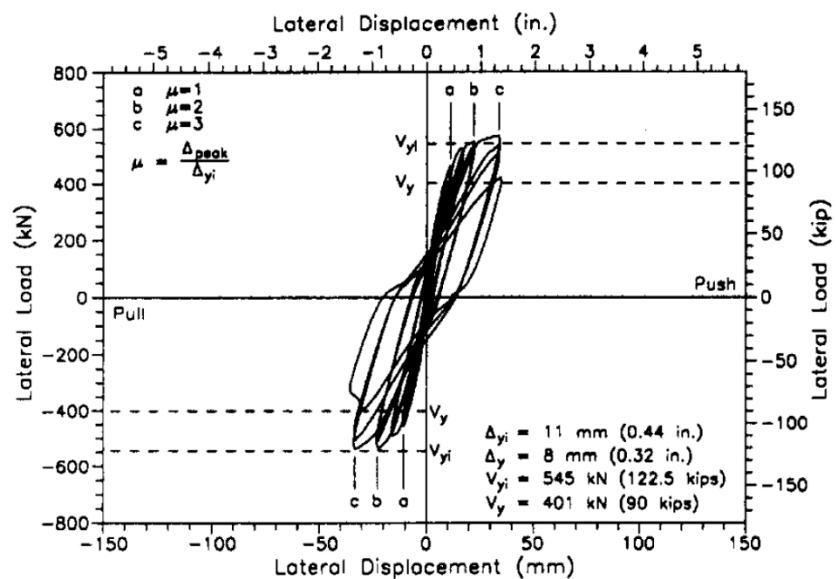


Figure 2.13 Cyclic load-displacement response of column #1 without CFRP.

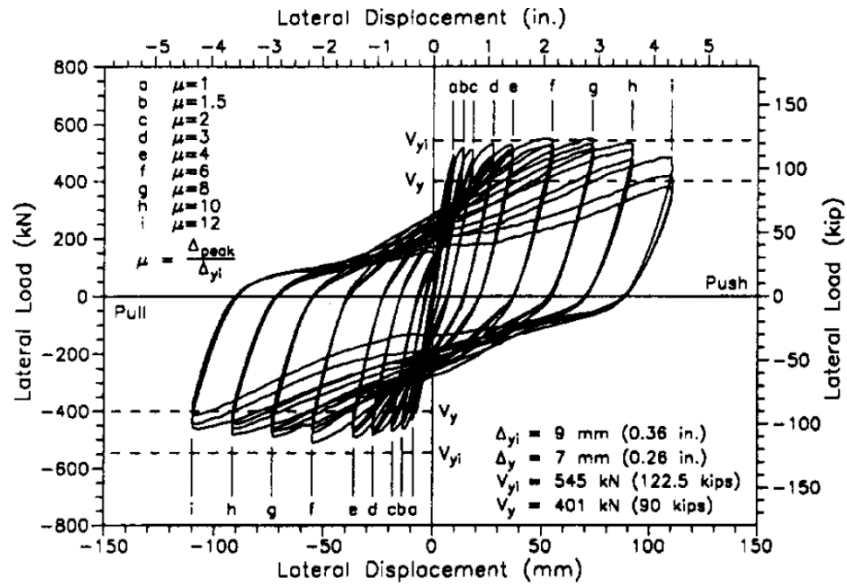


Figure 2.14 Cyclic load-displacement response of column #1 with CFRP.

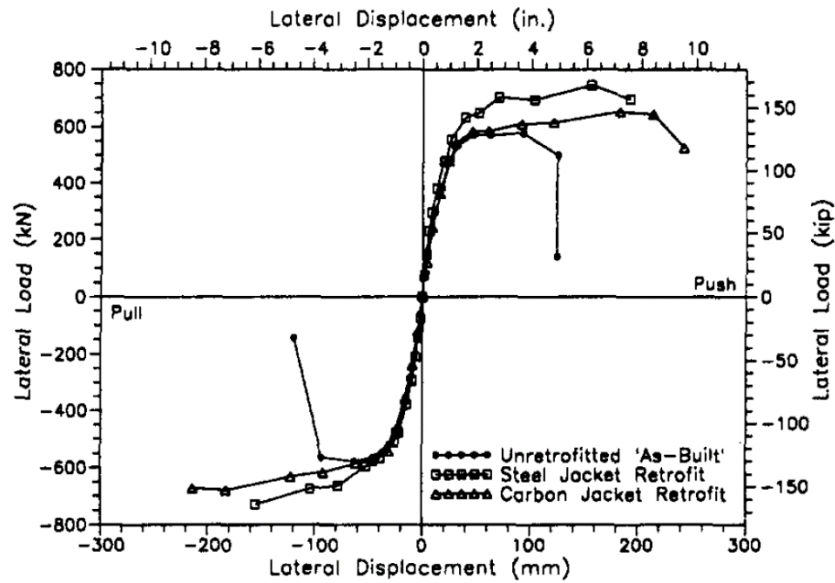
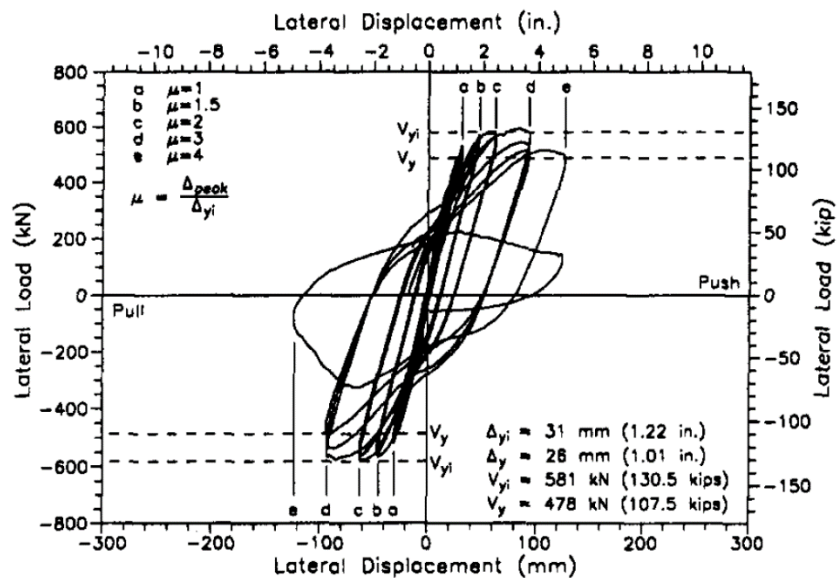
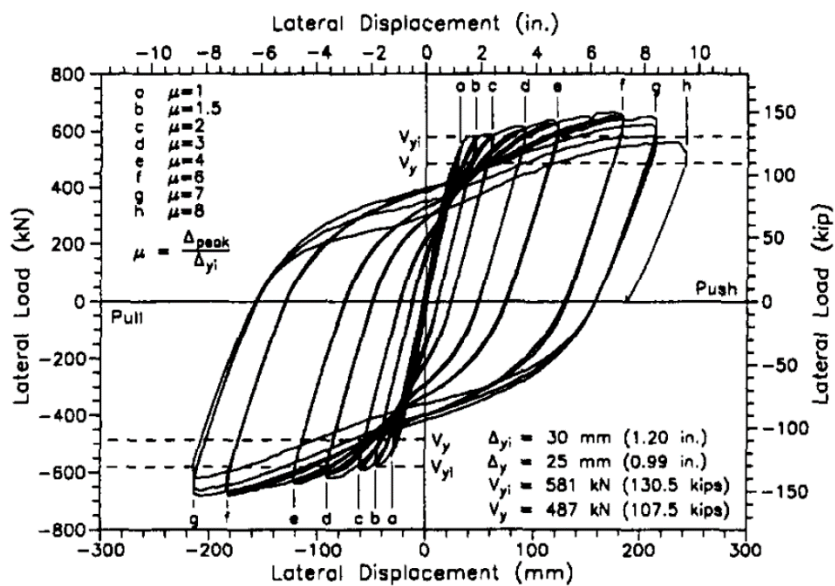


Figure 2.15 Monotonic load-displacement response of column #2.



**Figure 2.16** Cyclic load-displacement response of column #2 without CFRP.



**Figure 2.17** Cyclic load-displacement response of column #2 with CFRP.

In the following figures (**Figures 2.18 through 2.21**), the results of the computer analysis from SAP2000 are compared to experimental graphs.

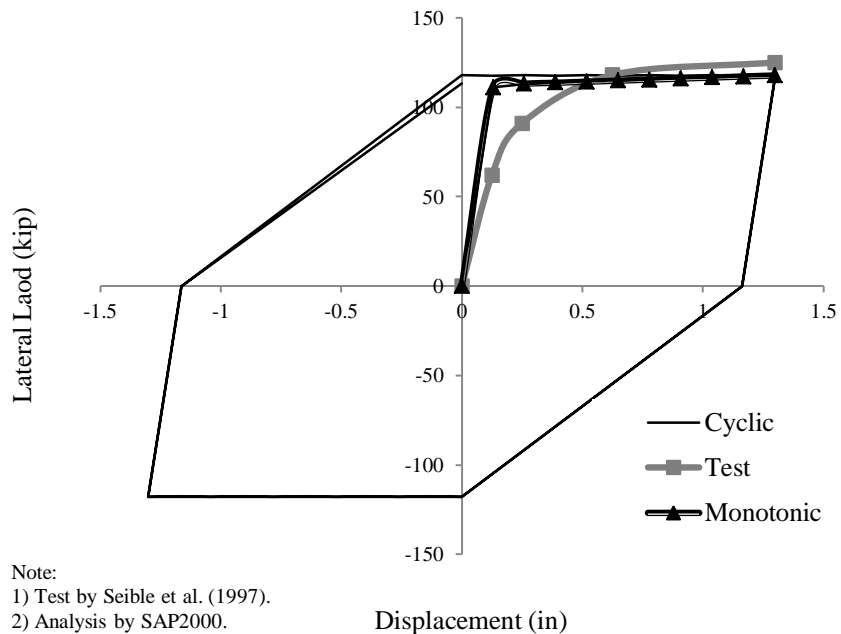


**Figure 2.18** Load-displacement response of column #1 without CFRP.

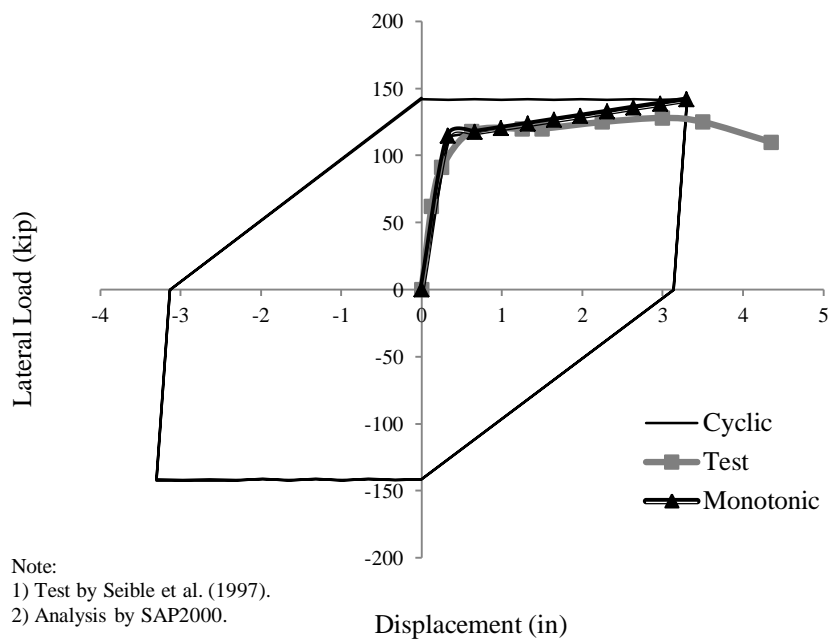


**Figure 2.19** Load-displacement response of column #1 with CFRP.

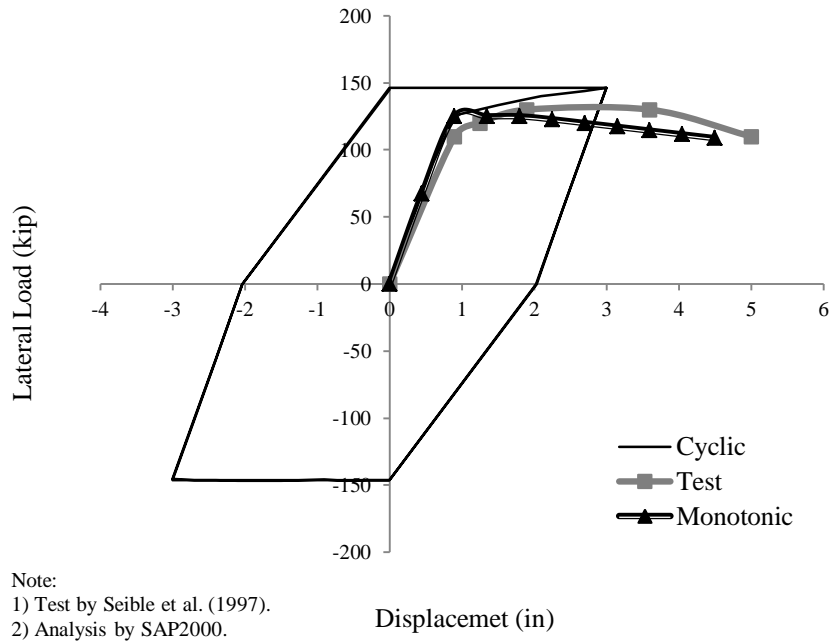


**Figure 2.20** Load-displacement response of column #2 without CFRP.

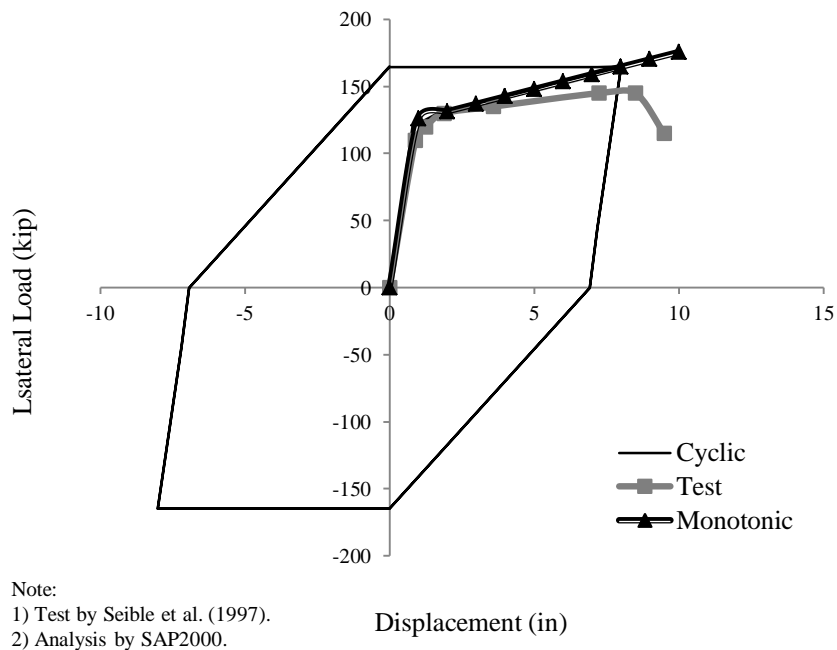


**Figure 2.21** Load-displacement response of column #2 with CFRP.

In **Figure 2.18**, which illustrates the result of monotonic and cyclic loading for column #1 without CFRP wrapping, the result of the computer analysis was compared with experimental results. The experimental load-displacement results yield a parabolic curve whereas the SAP2000 results were similar to a bilinear behavior. The slope within the elastic limit was found to be slightly greater for computer analysis than the test. However, the maximum horizontal loads determined from both the experimental testing and SAP2000 analysis were similar. The SAP2000 results for cyclic loading had the same trend as the monotonic results, and was similarly repeated for different load cycles. The test results of this column when wrapped with CFRP showed bilinear behavior as the computer analysis predicted. In this case, the slopes of these graphs in the elastic linear range were approximately the same. The maximum lateral load in SAP2000, however, was found to be slightly more than the value determined from the experimental tests. As was the case without a CFRP jacket, column behavior under cyclic load was found to be the same as monotonic loading and was similarly repeated for different cycles (**Figure 2.19**).

Computer analysis and test results for column #2 without CFRP wrapping were in good agreement when column was subjected to monotonic load (**Figure 2.20**). These results formed quasi bilinear graphs with almost equal slopes for the first portions or elastic region. The SAP2000 analysis results yielded 3 inches of deformation for the case of cyclic loading which was 33% less than determined through testing (4.5 inches approximately). Testing and SAP2000 results for column #2 when wrapped with CFRP also showed bilinear behavior (**Figure 2.21**). Slopes for the elastic region were identical as well as the start points of the second lines (yield points) . The SAP2000 analysis

predicted a steeper line with respect to the test results for the plastic portion of the graph. The cyclic result of the computer analysis showed a maximum deformation of 8 inches whereas the test cyclic loading had a maximum deformation of 10 inches (20% difference).

It can be said that there is an acceptable compliance between the computer analysis and test results. For CFRP wrapped sections under monotonic increasing lateral loading, SAP2000 slightly overestimates the column capacity. However, this software shows less flexibility for jacketed columns under cyclic lateral load. In conclusion, this proposed analysis method of concrete columns with or without CFRP jackets can accurately predict the load-deformation behavior of such columns under a combination of constant axial load and variable lateral load and can be utilized in design of these columns.

## **CHAPTER 3**

### **EXPERIMENTAL PROGRAM**

#### **3.1 Introduction**

An experimental investigation was carried out on slender RC columns to compare the ultimate load, load-deflection, and moment-curvature predicted by the proposed numerical method with those obtained experimentally. For the present study, six slender R/C columns were tested under cyclic axial compression with bidirectional eccentricities.

#### **3.2 Experimental Scheme**

##### **3.2.1 Design of Concrete Columns**

All the columns to be tested were designed to be slender columns. In basic terms, that means the cross-sectional dimensions of the columns have to be small relative to column length. Generally, the degree of slenderness is expressed in terms of the slenderness ratio  $l/r$ , where  $l$  is the unbraced length of the column and  $r$  is the radius of gyration of its cross section. Based on this concept, the same column dimensions from the experimental works of Tsao (1991), Bahn (1994), and Chen J. (2005) have been adopted for this research. Due to the size limitations of the testing machine, the total length of the column was set to 4 ft. Based on this column length, the nominal square cross section was set at 3.0 in.×3.0 in., which resulted in a slenderness ratio of 55. Two 7.0 in.×7.0 in.×8.0 in. concrete loading brackets were provided at the column ends to assist with the application of the biaxially eccentric load. All the columns were designed to resist a combination of both axial compression and biaxial bending. Based on the investigations by Tsao (1991), Bahn (1994), and Chen J. (2005), the column which has the same eccentricities at both



coordinate axes will have the most critical secondary moment. Therefore, eccentricities used in this research varied from 1.0 inch in the X and Y directions to 1.5 inches in the X and Y directions. The details of the test specimens can be seen in **Table 3.2** and **Figure 3.2**.

Four No. 3 steel reinforcing bars were designed as the main compression bars. The concrete cover of 0.5 in. thickness measured to the face of the longitudinal bars was provided to protect the steel bars. Twelve-gauge plain steel wire was also used at a 3 inch spacing for the lateral ties. The two brackets at each column end were heavily reinforced with No. 3 steel rebar to prevent any premature failure. The details of steel rebar can be found in **Figure 3.2**.

### 3.2.2 Materials

**3.2.2.1 Concrete.** The concrete used in the columns consisted of Type I cement satisfying ASTM 150, sand from a local source, crushed stone with a maximum aggregate size of 3/8 in., tap water, silica fume (SF) in powder form to achieve a higher strength, and a superplasticizer (SP) to maintain good workability. The mix designs of the columns used in this research are listed in **Table 3.1**.

**Table 3.1** Mix Design of Concrete Columns

Batch	Water/ Cement ratio	Cement (lbs)	Stones (lbs)	Sand (lbs)	Water (lbs)	Silica Fume	SP (mL)	Concrete Compressive Strength (psi)
1	0.48	52.44	128	87.7	25.18	N/A	N/A	7,250
2	0.28	64.32	141.02	90.2	18.1	3.25	375	18,100
3	0.29	64.48	141.8	90.2	18.48	3.25	375	21,100
4	0.29	64.48	141.8	90.2	18.48	3.25	375	18,450

**3.2.2.2 Reinforcement.** Four No. 3 bars were used in the columns to resist the combined force due to the axial compression and biaxial bending. The tensile tests for No. 3 steel bars were performed with the use of a material testing system (MTS) machine. An average yielding stress of 56.9 ksi was identified for the reinforcement with a modulus of elasticity of 28,670 ksi. The complete stress-strain behavior of the No. 3 bar is shown in Appendix A. The stirrups consist of 12-gauge steel wires. Six U-shape No. 3 steel bars were used to reinforce the loading brackets. The detailed steel arrangement can be seen in **Figure 3.1**.

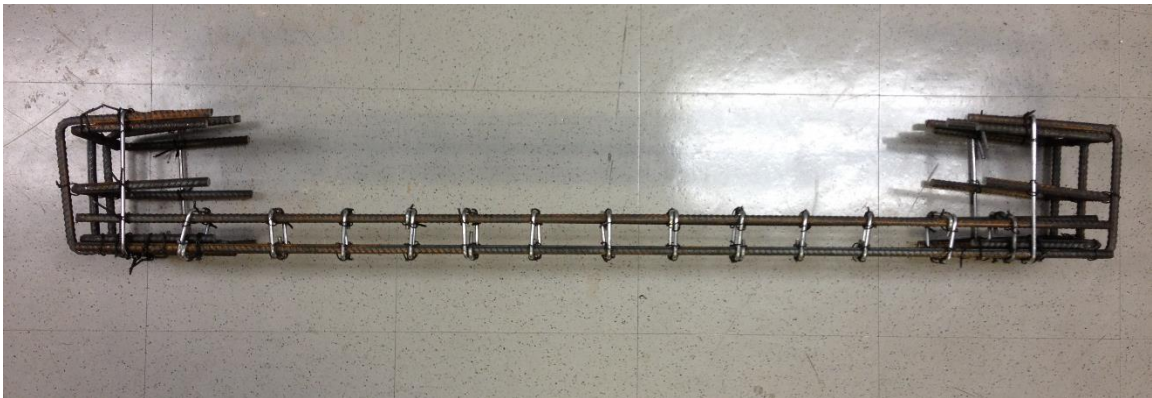


**Figure 3.1** Steel reinforcement for test columns.

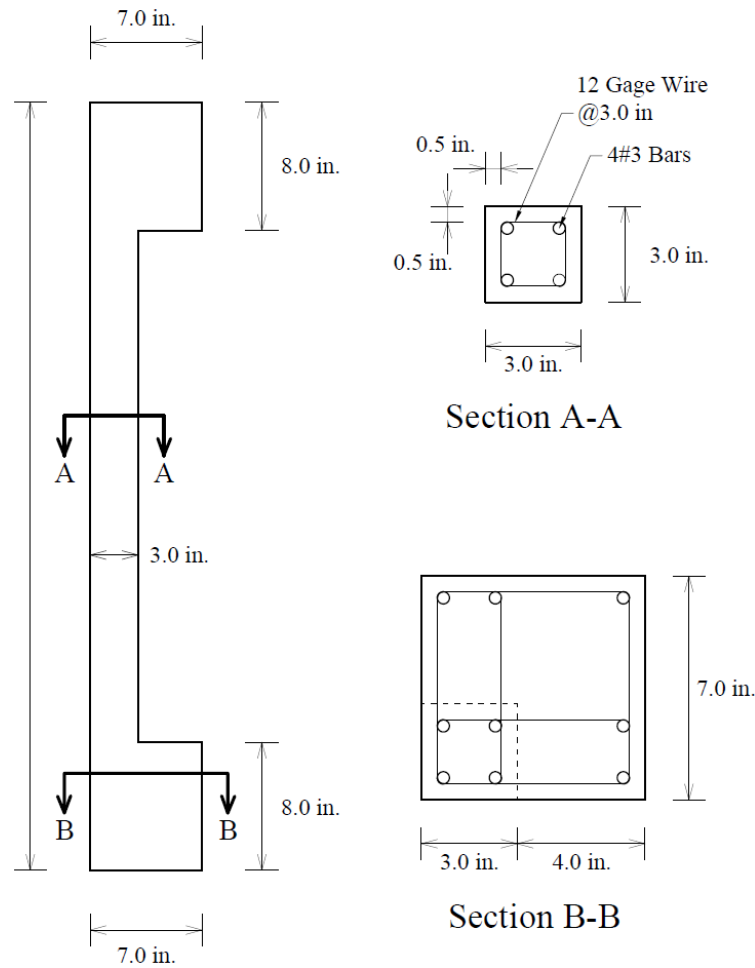


**Figure 3.2** Column configuration.

### 3.2.3 Cast and Cure of the Concrete Columns

To minimize scatter, all specimens followed the same procedures for material mixing, casting, and curing. A total of six slender RC columns were cast at the concrete laboratory of NJIT. They were divided into four batches. Wooden forms (**Figure 3.3**) and steel rebars (**Figure 3.1** and **Figure 3.2**) were prepared before the concrete was mixed.

All concrete materials described in the previous section were mixed by a rotary mixer. The 4 in. by 8 in. cylinder molds were prepared and lubricated with oil before the concrete was poured. The mixing sequence used was as follows: Firstly, the coarse and fine aggregates were loaded into the mixer and dry mixed for 2 to 3 minutes. Next, the

cement and silica fume were added and mixed for another 1 to 2 minutes. Then, 80% of the water was added to the cementitious material. The remainder of the water was first mixed with the superplasticizers and later was added to the cementitious material over a 2 minute period to form a uniform mixture. After all the materials were added, the small rotary mixer continued mixing for a few minutes until a homogeneous mixture was achieved. The resulting mixture was then molded into the wooden forms and 4 in. by 8 in. cylindrical specimens.

During casting, both electrical (table vibrator) and manual (steel bar) methods were used to compact the specimens. All specimens were demolded after 48 hours and cured in a standard curing room to achieve the desired strength. For each batch of concrete, multiple 4 in.  $\times$  8 in. cylinders were made at the same time to aid in the determination of the compressive strength of the concrete columns. The average stresses for the cylinders are listed in **Table 3.1**.

**Table 3.2** Test Outline of Column Specimens

Specimen	$f'_c$ (psi)	Main Bars	$e_x(e_y)$ (in.)	$l$ (in.)
C1	7,250	4#3	1.5	48
C2	18,450	4#3	1.5	48
C3	21,100	4#3	1.5	48
C4	18,100	4#3	1.5	48
C5	18,450	4#3	1.0	48
C6	21,100	4#3	1.0	48

Where  $f'_c$  = Compressive strength of concrete.

$e_x, e_y$  = Eccentricity along X-Axis and Y-Axis, respectively.

$l$  = Total length of column specimens.



**Figure 3.3** Wooden forms used for the test columns.

### **3.2.4 Experimental Setup**

The column tests were performed using an electro-hydraulic closed loop servo controlled MTS under stroke control. To obtain the complete ascending and descending branches of the biaxial load-deflection curve, loads were applied at very small increments of 0.05 in. per minute for stroke control.

In order to achieve the desired hinged end conditions, steel ball bearings were utilized at each end of the column. The desired eccentricities were obtained by moving the ball bearings to the proper positions relative to the center of the cross section. The column specimens were adjusted so that the centerline of the end bearing facing the load cell coincided with its center line. Subsequently, a small load was applied to keep the specimens in place. A typical test setup is shown in **Figure 3.4**.

Three linear voltage differential transducers (LVDT) were used to measure the deflections at mid-height of the column specimens in both X, Y, and 45° (respect to X and Y) directions. The LVDTs were connected to a computerized data acquiring system that was connected directly to the MTS machine. Then the deflections from LVDTs as well as axial load from the load cell were recorded to the computer at a rate of 10 times per second until the specimen failed. The LVDTs needed to be adjusted during the test process because the deflection in each direction could potentially exceed the limit of the reading range. Six mechanical strain gauges were provided to measure the vertical strain at the central portion of the column so that the average curvature in both the X and Y directions at mid-height could be attained. **Figure 3.5** shows the arrangement of mechanical gauges for the present slender column specimens. At maximum and minimum of every loading cycle, the strain values for each pair of mechanical gauges were recorded. If the concrete failed outside the 6 in. measured range, further measurements were not recorded. Measurements were not recorded in these cases because the plastic hinge rotated outside of the measured areas at mid-height.

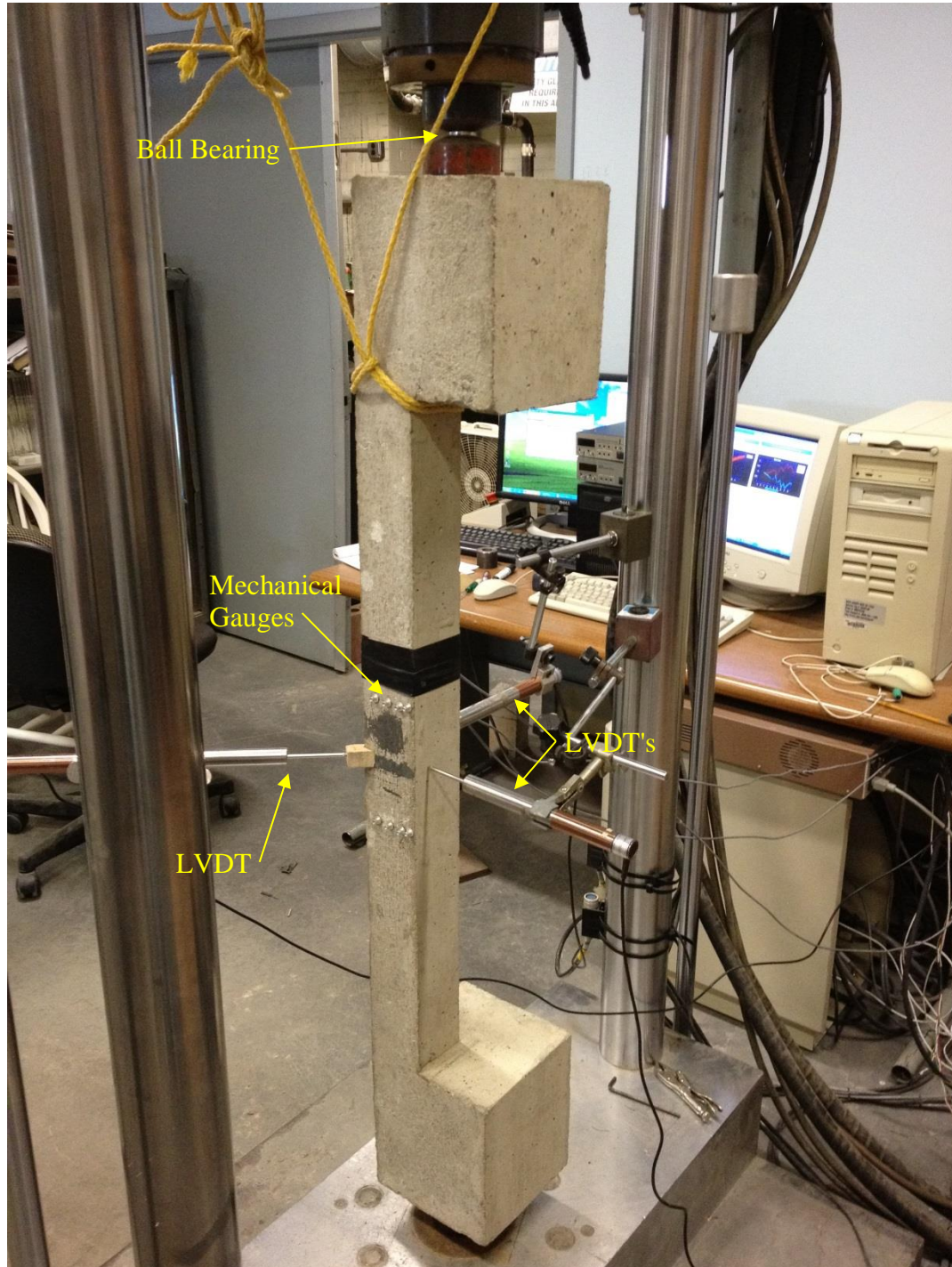


**Figure 3.4** Test setup.

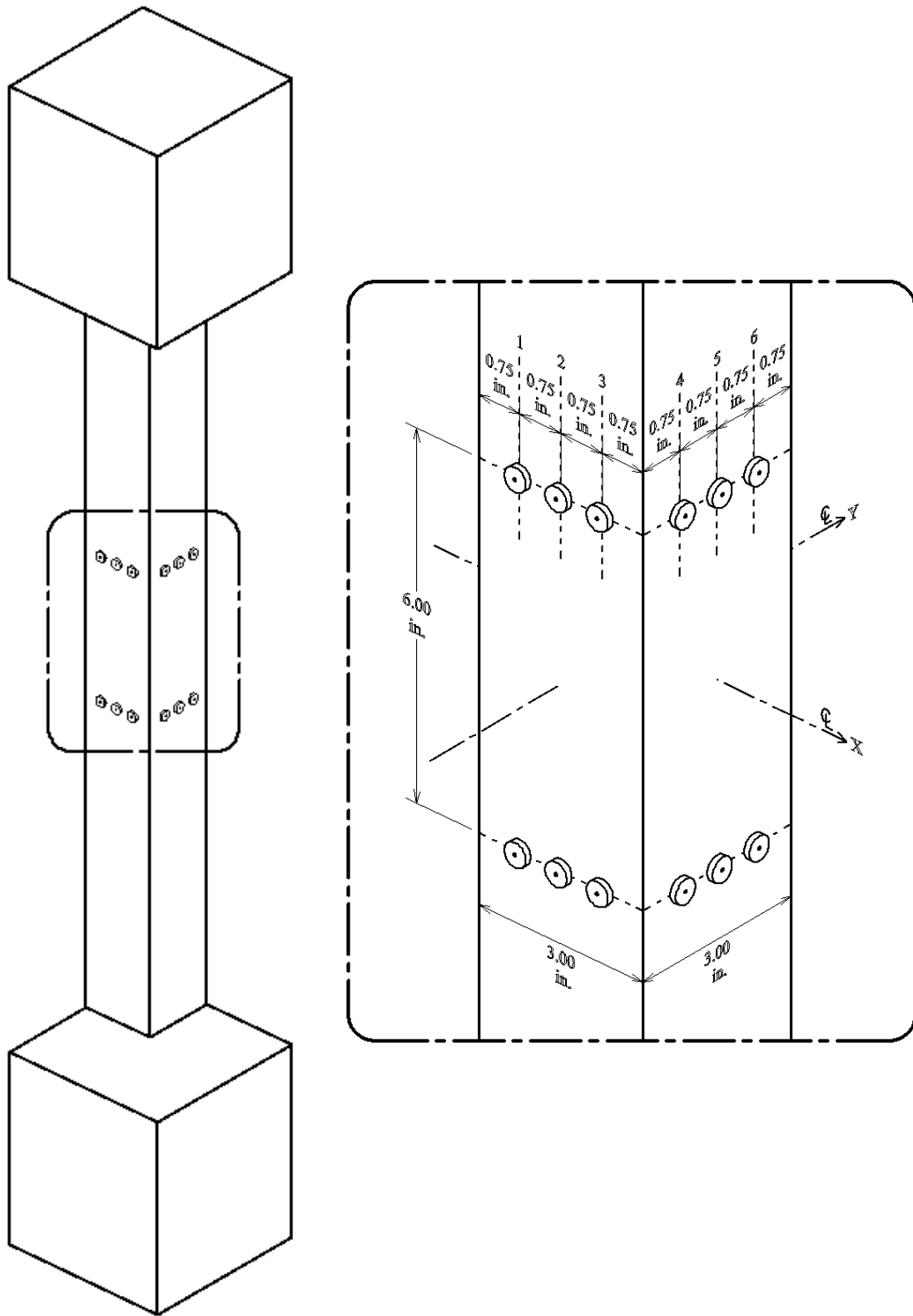


**Figure 3.5** Arrangement of mechanical strain gauges.



### 3.2.5 Test Procedures

**3.2.5.1 Column C1.** The first column tested was column C1. The eccentricities in both the X and Y directions for this column were 1.5 inches. When the load reached 8.1 kips, the first flexural crack occurred at the mid-height of the column. As the load increased, more cracks developed around the initial crack and at the top of the column. The plastic hinge occurred almost at the mid-height. When the load reached 11.1 kips, the load decreased as the deflection began to increase. When the load decreased to approximately 9 kips, the specimen failed due to crushing of the concrete in the compression zone (**Figure 3.6**). The test was terminated at a vertical displacement of 0.6 inches.



Column C1 at failure



Tension face



Compression face

**Figure 3.6** Failure of column C1.

**3.2.5.2 Column C2.** Column C2 was tested with eccentricities in both the X and Y directions equal to 1.5 inches. When the load reached approximately 12 kips, the initial crack occurred on the tension face around the center of the column. Another three flexural cracks developed near the top of the column as the load increased (**Figure 3.7**). The plastic hinge occurred at the top of the column. The load started to decrease after it reached 15.5 kips. There was no obvious buckling of the steel reinforcing bars. The test was terminated at a vertical displacement of 0.5 inches.



Column C2 at failure



Tension face



Compression face

**Figure 3.7** Failure of column C2.

**3.2.5.3 Column C3.** The next tested column was C3. The eccentricities in both the X and Y directions were 1.5 inches. The initial crack occurred on the tension face at the mid-height of the column at a load of 12.5 kips. As the load increased, more cracks developed around the initial crack which caused the formation of the plastic hinge almost at the mid-height. When the load reached 12.8 kips, the load started to decrease as the deflection started to increase. When the load decreased to approximately 11 kips, the specimen failed due to crushing of the concrete in the compression zone (**Figure 3.8**). The test was terminated at a vertical displacement of 0.6 inches.



Column C3 at failure



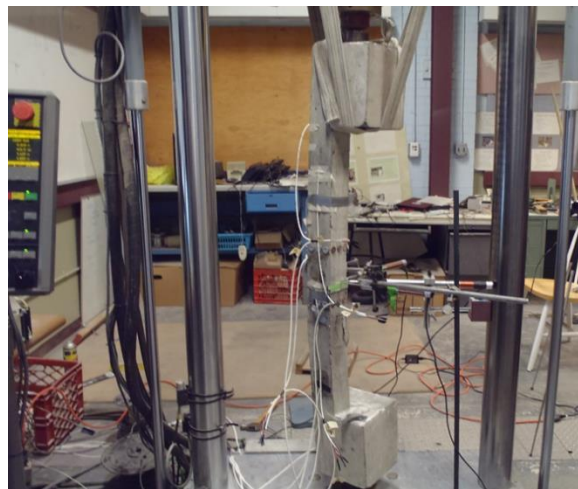
Tension face



Compression face

**Figure 3.8** Failure of column C3.

**3.2.5.4 Column C4.** The next column was C4. The eccentricities in both the X and Y directions were 1.5 inches. When the load reached approximately 12.5 kips, the initial crack occurred on the tension face, slightly below the mid-height of the column. As the load increased, more cracks developed which caused the formation of a plastic hinge below the lower mechanical gages. When the load reached 15.2 kips, the load started to decrease as the deflection started to increase. When the load decreased to approximately 10 kips, the specimen failed due to crushing of the concrete in the compression zone (**Figure 3.9**) and buckling of one of the reinforcing bars. The test was terminated at a vertical displacement of 0.6 inches.



Column C4 at failure



Tension face



Compression face

**Figure 3.9** Failure of column C4.

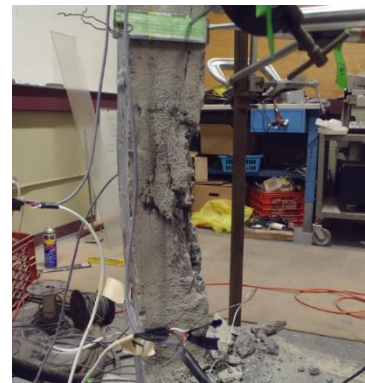
**3.2.5.5 Column C5.** The next column was C5. The eccentricities in both the X and Y directions were 1.0 inch. Initial cracks occurred on the tension face below the mid-height of the column when the load reached approximately 12.8 kips. As the load increased, additional cracks developed between the lower mechanical gages and the foot of the column. When the load reached 22.7 kips, the load started to decrease as the deflection started to increase. When the load decreased to approximately 14 kips, the specimen failed due to crushing of the concrete in the compression zone (**Figure 3.10**). The increase in the displacement resulted in buckling of the one of the reinforcing bars. The test was terminated at a vertical displacement of 0.4 inches.



Column C5 at failure



Tension face



Compression face

**Figure 3.10** Failure of column C5.

**3.2.5.6 Column C6.** The last column was C6. The eccentricities in both the X and Y directions were 1.0 inch for this column. In this test, when load reached approximately 15 kips, initial cracks occurred on the tension face above the upper mechanical gages. As the load increased, more cracks developed at this location. The load started to decrease as the deflection started to increase following a maximum axial load of 23.8 kips. The column specimen failed due to crushing of the concrete in the compression zone (**Figure 3.11**) and buckling of one of the reinforcing bars. The test was terminated at a vertical displacement of 0.4 inches.



Column C6 at failure



Tension face



Compression face

**Figure 3.11** Failure of column C6.

**Table 3.3** Condition of Column Specimens at Failure

Specimen	Location of Plastic Hinge	Exposed Steel Bars	Buckled Bars
C1	Mid-height	Yes	None
C2	Below the top bracket	None	None
C3	Mid-height	Yes	None
C4	Below the lower mechanical gauges	Yes	Yes
C5	Below the lower mechanical gauges	Yes	Yes
C6	Above the upper mechanical gauges	Yes	Yes



(From right to left: C1 to C6)

**Figure 3.12** Final conditions of column specimens.

### 3.3 Results and Discussions

#### 3.3.1 Analysis of Test Results

Six test columns (C1 to C6) are discussed in this research study. The applied load,  $P$ , can be determined directly from both the MTS system and the data acquisition system. The vertical and horizontal ( $d_x$ ,  $d_y$ , and  $d_{diagonal}$ ) deflections were also recorded directly from the data acquisition system that was connected to three LVDTs. Load-vertical deflection curves and load-deflection curves for columns C1 to C6 are presented in Appendix C. Since the eccentricities used were exactly the same for both the X and Y directions, the experimental results for both directions are expected to be similar. The minor differences in the results are attributed to measurement errors during testing. Therefore, only the results of one direction are discussed in this chapter. As an illustration, the load-vertical deflection curve and load-deflection curve for both the X and Y directions for column C5 are depicted in **Figures 3.13** and **3.14**, respectively.

The experimental values of bending moments in the X and Y directions,  $M_x$  and  $M_y$ , were computed using the experimental axial load values and the load eccentricities, ( $e_x$  and  $e_y$ ) which were corrected for the mid-height deflections of the column (i.e.,  $M_x = P(e_y + d_y)$  and  $M_y = P(e_x + d_x)$ ). The experimental ultimate load and moment capacities for all six columns are summarized in **Table 3.4**.

The longitudinal strain,  $\varepsilon$ , can be calculated by  $\varepsilon = (l_i - l_0) / l_0$ , when  $l_0$  represents the initial distance between mechanical strain gauges at zero loading and  $l_i$  represents the distance between the mechanical strain gauges at each loading. At present study,  $l_0 = 6$  in (152mm) as shown in **Figure 3.5**. After determining the strain from the mechanical strain gauge points located at 1, 2, and 3 for the X direction and at 4, 5, and 6 for the Y



direction (**Figure 3.5**), the strain-position curves can be drawn. These curves are shown in Appendix B. **Figure 3.15** shows a typical strain-position curve for column C5 in the X direction. The slope of the strain-position curve can be used to calculate its corresponding curvature. Usually, a strain distribution curve is linear. If the strain distribution curve is not linear, a straight line by a linear regression method is used to compute its curvature value.

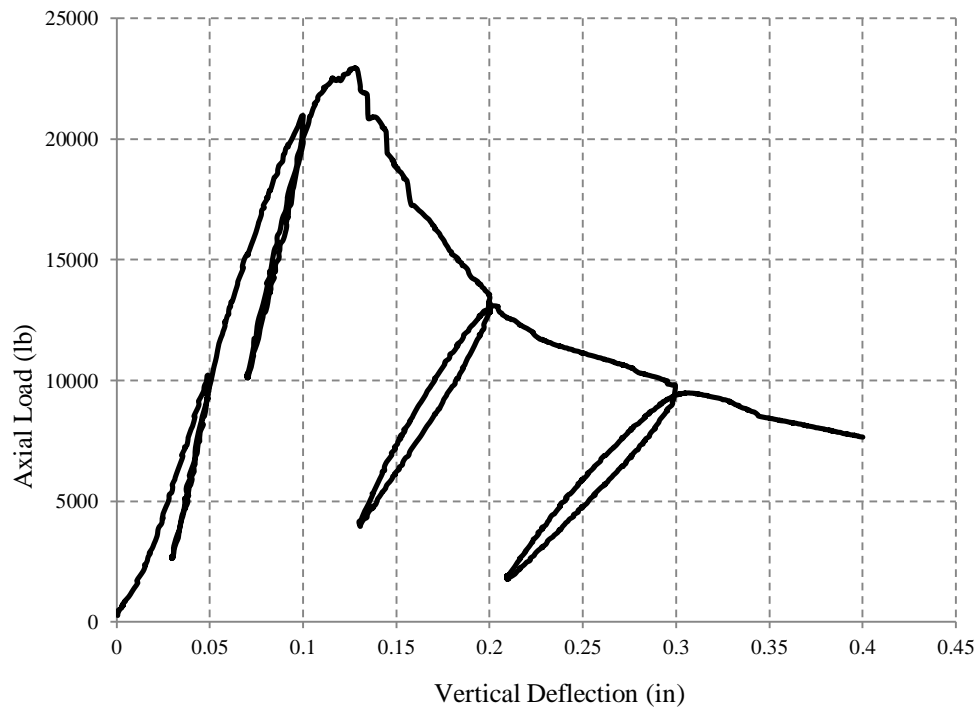


**Figure 3.13** Typical load-vertical deflection curve for column C5.

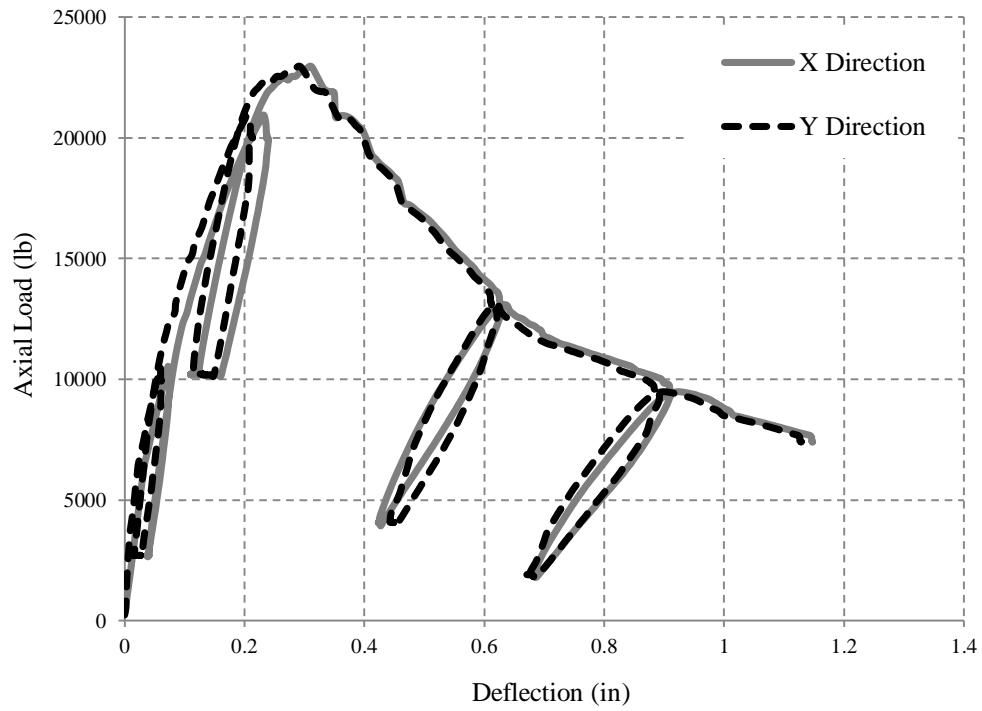


**Figure 3.14** Typical load-deflection curves for column C5.

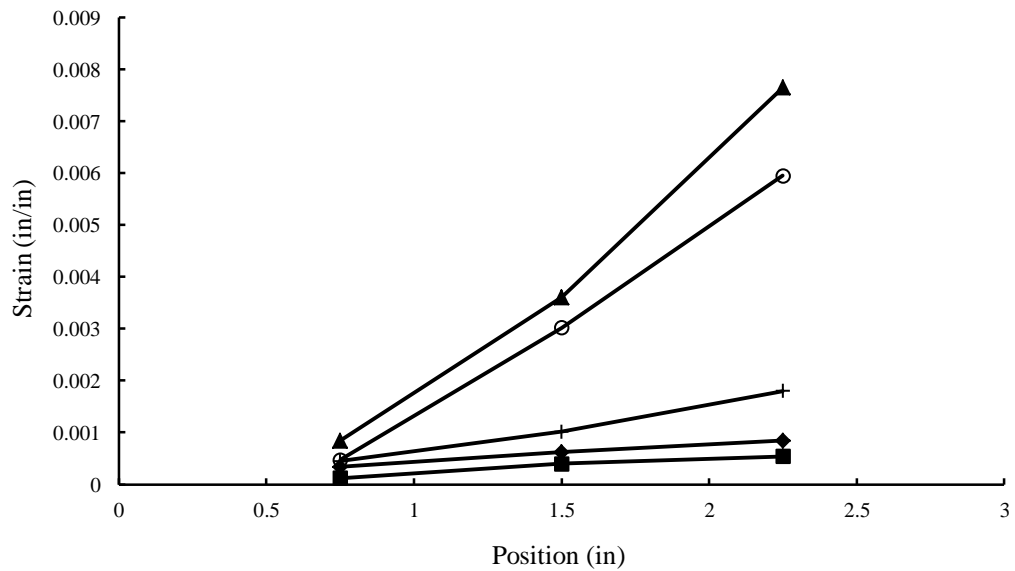


**Figure 3.15** Typical strain-position curve for column C5 in X direction.

**Table 3.4** Experimental Results of Test Columns

Tested Column	Ultimate Load P (kips)	Ultimate Moment $M_x$ ( $M_y$ ) (lb-in)	Corresponding Deflection $d_x$ ( $d_y$ ) (in)
C1	11,100	21,809	0.46
C2	15,450	30,915	0.50
C3	12,846	26,348	0.55
C4	15,192	28,299	0.36
C5	22,652	29,549	0.30
C6	23,765	31,813	0.34

## **CHAPTER 4**

### **ANALYSIS OF RC CONCRETE COLUMNS UNDER AXIAL LOADING WITH BIDIRECTIONAL ECCENTRICITIES**

#### **4.1 Introduction**

A numerical method was developed to study the behavior of bi-axially loaded slender RC columns, made of NSC and HSC, under monotonic and cyclic loads. This numerical procedure followed the study by Bahn (1994). In this approach, both material non-linearity (concrete) and geometrical non-linearity were considered. The latest concrete time-dependent models were also adopted. It is a generalized method in terms of loading history, column supports, material (concrete) stress-strain behavior and shapes of column sections (unchanged through length of column). Except for basic dimensions, loading history, support conditions, and material properties, no further manually input data are needed.

#### **4.2 Analysis Strategies**

##### **4.2.1 Description of Column Analysis**

The numerical procedures of the previous studies by Wang & Hsu (1990) and Tsao (1991) are based on the incremental deflection approach, where a deflection is assumed to be in a specific direction. This analytical procedure was effective only to increase the strain at the divided areas of steel and concrete in the column section under monotonically increasing load. The unloading in curvatures was not considered because the analytical formulations were expressed in terms of cross-sectional stiffness, strain at the coordinate origin, and deflection along the column. The convergencies were only confirmed for the strain at the coordinate origin, axial force and deflection. After the

deflections were determined, the corresponding curvatures were calculated from the finite difference method. Furthermore, the convergence criteria were difficult to reach the desired accuracy due to the assumption of increasing deflection for the subsequent stage of analysis. Thus, it can be concluded that a simple modification of the previous numerical procedure cannot handle the different loading paths needed in the present study.

Variations in loading can affect the stiffness and strength of the RC column, especially when loading and unloading occur. In addition, the axial load acting on a column section influences the flexural stiffness, the moment capacity, and the ductility of RC columns.

A finite segment method of analysis is extended here to predict the behavior of slender RC columns under cyclic loading with bidirectional eccentricities. The numerical procedure is designed to consider increasing or decreasing of the strain at discrete elements in the column under cyclic loading. The rate of convergence of the analysis depends on the proposed values of deflection and strain. The convergence of iterative procedures can be improved through either the interpolation or extrapolation method which utilizes the previous solutions.

The load-deflection curve, moment-curvature curve and ultimate load are predicted through the developed computer program. The computer model developed for the present study has the following capabilities:

1. General cross sections are possible to enable consideration of any arbitrary shapes.
2. Complex loading conditions, including cyclic compression with bidirectional eccentricities, can be considered.

3. Both material and geometrical nonlinearities can be considered.
4. Various end conditions can be considered, however, in this case, both ends of the column are assumed to be pinned-ended.

#### **4.2.2 Idealized Stress-Strain Relations for Column Analysis**

Once the strain in any discrete element is proposed, the corresponding stress can be obtained provided idealized stress-strain relationships are available. Therefore, a complete stress-strain curve for each column material is necessary for analysis. Generally, the complexity of the finite segment method in column analysis is a direct function of the material stress-strain relationships. The secant stiffness is defined as the secant slope of the stress-strain curve for a given strain. Here, the secant stiffness is used to study the column behavior for both ascending and descending branches. It should be noted that, in the case of stress computation, the stiffness must be derived by considering the strain history at certain elements along either the loading or unloading paths in the stress-strain curve.

To determine a reasonable result, the element stiffness should be updated whenever an event occurs at an individual element. This, however, can be computationally unfeasible especially if a highly complex material model is adopted. For this reason, material models should be idealized to be as simple as possible.

**4.2.2.1 Stress-Strain Relationship for Concrete.** An idealized concrete model should be able to represent the physical characteristics of stiffness on the envelope curve. In addition, the definition of stiffness on the unloading or reloading stress-strain paths must be reasonably established. Since the slope change of the unloading curve varies in the range from the envelope unloading point to the zero stress level, the stiffness cannot be adequately defined on the unloading stress-strain path. It can be concluded that the

stiffness on the unloading or reloading stress-strain paths is defined primarily by the slope on the reloading path of the cyclic stress-strain curve. The change in the slope of the reloading stress path is more stable than the change in the slope of unloading path.

In this study, a hysteretic stress-strain behavior of HSC under reversed cyclic loading by Konstantinidis, Kappos, and Izzuddin (2007) was employed to describe the cyclic stress-strain relationships for concrete. The envelope curve in this stress-strain behavior was derived from the results of uniaxial, monotonic, compression loading tests of 108 large-scale specimens. This model explicitly accounts for the effects of concrete compressive strength, the volumetric ratio of transverse reinforcement, the yield strength of the ties, tie spacing, and tie pattern. Comparisons with test results show that the proposed model provides a good fit for a wide range of experimentally established hysteresis loops.

Previous experimental investigations have concluded that the envelope (known also as a skeleton) stress-strain curve of NSC under repeated or cyclic compressive loading nearly coincides with the stress-strain response under uniaxial loading. A similar conclusion has also been drawn for HSC columns confined with high strength steel.

A three-branch stress-strain curve (**Figure 4.1**) to model the response of HSC under uniaxial loading forms an envelope curve to the cyclic loading stress-strain response, both for confined and unconfined HSC:

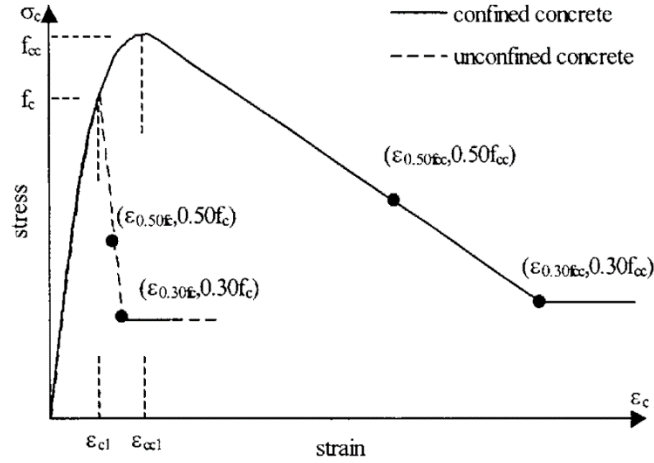


**Figure 4.1** Envelope curves for unconfined and confined HSC, Konstantinidis, Kappos, and Izzuddin (2007).

$$\text{Ascending branch: } 0 < \varepsilon_c \leq \varepsilon_{ccl}, \quad \sigma_c = \frac{f_{cc} \frac{\varepsilon_c}{\varepsilon_{ccl}} \frac{E_c}{E_c - E_{cl}}}{\frac{E_c}{E_c - E_{cl}} - 1 + \left(\frac{\varepsilon_c}{\varepsilon_{ccl}}\right)^{\frac{E_c}{E_c - E_{cl}}}} \quad (4.1)$$

$$\text{Descending branch: } \varepsilon_c > \varepsilon_{ccl}, \quad \sigma_c = f_{cc} \left[ 1 - 0.5 \frac{\varepsilon_c - \varepsilon_{ccl}}{\varepsilon_{0.50f_{cc}} - \varepsilon_{ccl}} \right] \geq 0.3f_{cc} \quad (4.2)$$

where  $\varepsilon_c$  is the axial concrete strain,  $\sigma_c$  is the concrete stress,  $\varepsilon_{ccl}$  is the axial concrete strain at peak stress of the confined concrete,  $f_{cc}$  is the maximum compressive strength of the concrete,  $E_c$  is the tangent modulus of elasticity of concrete,  $E_{cl}$  is the secant modulus of elasticity, and  $\varepsilon_{0.50f_{cc}}$  is the strain at which the stress in the confined concrete drops to  $0.5f_{cc}$ . The modulus of elasticity of concrete is given by the following relationship:

$$E_c = 22,000 \left( \frac{f_c}{10} \right)^{0.3} \quad (\text{MPa}) \quad (4.3)$$



Whereas the secant modulus of elasticity at peak stress is

$$E_{cl} = \frac{f_{cc}}{\varepsilon_{ccl}} \quad (\text{MPa}) \quad (4.4)$$

In the case of confined HSC members, the peak stress is given by the following equation, which assumes that the compressive strength in a full size member is 15% lower than the corresponding strength of a shorter test cylinder.

$$f_{cc} = 0.85f_c + 10.3(\alpha\rho_w f_{yw})^{0.4} \quad (\text{MPa}) \quad (4.5)$$

This assumption is a result of the difference in size and shape, less effective compaction, water segregation, etc., which more commonly occur in a full size member. The maximum stress for unconfined HSC is assumed to be that corresponding to the strength specified in standard sized cylinders (i.e., 150×300 mm). In equation (4.5),  $\alpha$  is a factor which takes into account the effectiveness of confinement, and which is represented by the following formula:

$$\alpha = \left(1 - \frac{\sum b_i^2}{6 b_c d_c}\right) \left(1 - \frac{s}{2 b_c}\right) \left(1 - \frac{s}{2 d_c}\right) \quad (4.6)$$

where  $b_i$  = center-to-center distance between laterally supported longitudinal bars;  $b_c$  = center-to-center width of the perimeter tie;  $d_c$  = center-to-center height of the perimeter tie; and  $s$  = spacing between the ties. The strain at peak stress of the confined HSC ( $\varepsilon_{ccl}$ ) is assumed to be given by

$$\frac{\varepsilon_{ccl}}{\varepsilon_{cl}} = 1 + 32.8(\alpha\omega_w)^{1.9} \quad (4.7)$$

where the mechanical ratio of transverse reinforcement is given by

$$\omega_w = \frac{\rho_w f_{yw}}{f_c} \quad (4.8)$$

and the strain at peak stress for unconfined HSC ( $\varepsilon_{cl}$ ) is given by

$$\varepsilon_{cl} = \frac{0.70 f_c^{0.31}}{1,000} \quad (4.9)$$

The strain corresponding to a drop in maximum stress by 50%, which determines the slope of the descending branch, is given by Equation (4.10) for confined HSC

$$\varepsilon_{0.50f_{cc}} = \varepsilon_{cl} + 0.091(\alpha\omega_w)^{0.8} \quad (4.10)$$

whereas for unconfined concrete, Equation (4.11) is adopted

$$\varepsilon_{0.50f_c} = \left[ \frac{E_c}{2E_{cl}} + 1 + \sqrt{\left( \frac{E_c}{2E_{cl}} + 1 \right)^2 - 2} \right] \quad (4.11)$$

**Figure 4.1** illustrates the envelope curves for confined and unconfined HSC. The “plastic” strain  $\varepsilon_{pl}$ , better referred to (in the case of concrete) as the non-recoverable strain, is the strain corresponding to zero stress along the compressive unloading or reloading curves reflecting the accumulation of damage in a member and defining the strength and stiffness degradation due to cyclic loading.

The response of concrete is essentially elastic when unloading occurs within the range of strains from the origin up to the strain corresponding to a stress equal to 35% of maximum strength ( $\varepsilon_{0.35f_{cc}}$ ) along the ascending branch (**Figure 4.2**). Therefore, plastic strains can be obtained by

$$0 \leq \varepsilon_{un} \leq \varepsilon_{0.35f_{cc}} \quad , \quad \varepsilon_{pl} = \varepsilon_{un} - \frac{\sigma_{un}}{E_c} \quad (4.12)$$

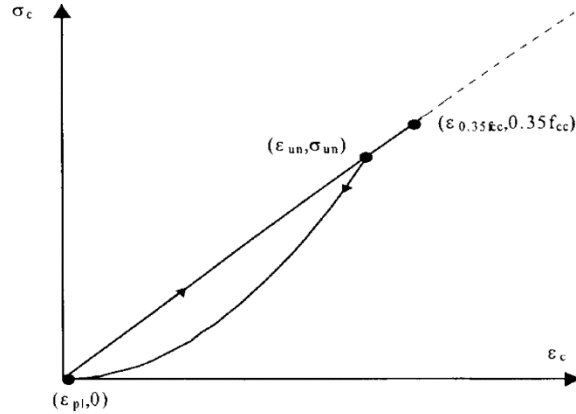


**Figure 4.2** Plastic strain in the low strain range.  
Source: Konstantinidis, Kappos, & Izzuddin (2007).

**Figure 4.3** shows the proposal for the determination of plastic strain for the intermediate strain range, i.e., for  $\varepsilon_{0.35f_{cc}} \leq \varepsilon_{un} \leq 2.5 \varepsilon_{ccl}$ . It is seen from the figure that point  $(\varepsilon_{pl}, 0)$  lies on the line connecting the reversal point from the envelope  $(\varepsilon_{un}, \sigma_{un})$  and the focal point  $(\varepsilon_a, \sigma_f)$ . In addition, the focal point lies on the line passing through the origin with a slope equal to the tangent modulus ( $E_c$ ). By combining the equations for the two lines, plastic strain can be specified as follows:

$$\varepsilon_{0.35f_{cc}} < \varepsilon_{un} \quad , \quad \varepsilon_{pl} = \varepsilon_{un} - \frac{\sigma_{un}(\varepsilon_{un} + \varepsilon_a)}{\sigma_{un} + E_c \varepsilon_a} \quad (4.13)$$

where  $\varepsilon_a$  is given by the following equation:

$$\varepsilon_a = a\sqrt{\varepsilon_{un}\varepsilon_{ccl}} \quad (4.14)$$

where  $a$  = maximum value of the two ratios presented in Equation 4.15, which, in the absence of more refined values, are also adopted for HSC.

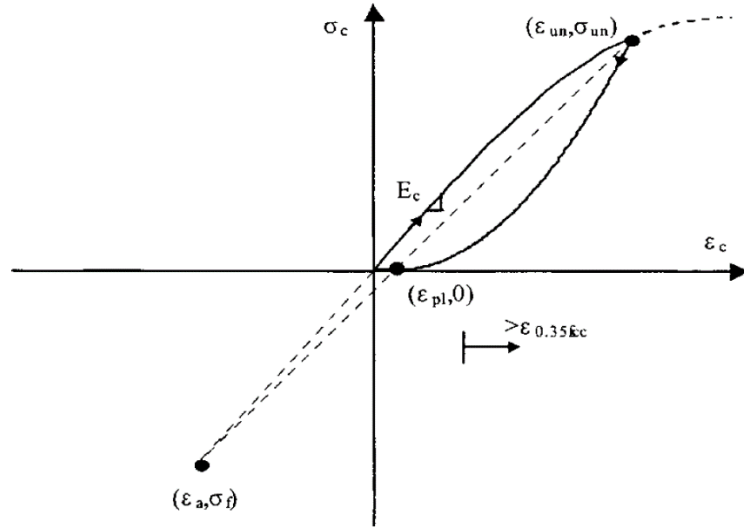


**Figure 4.3** Plastic strain in the intermediate and high-strain range.  
*Source: Konstantinidis, Kappos, & Izzuddin (2007).*

$$a = \max \left\{ \begin{array}{l} \frac{\varepsilon_{ccl}}{\varepsilon_{ccl} + \varepsilon_{un}} \\ \frac{0.09 \varepsilon_{un}}{\varepsilon_{ccl}} \end{array} \right. \quad (4.15)$$

The equation describing the unloading branch is a second-degree parabola passing through the reversal point from the envelope  $(\varepsilon_{un}, \sigma_{un})$  and the current plastic strain point  $(\varepsilon_{pl}, 0)$ , as shown in **Figure 4.3**.

$$\sigma_c = \sigma_{un} \left( \frac{\varepsilon_c - \varepsilon_{pl}}{\varepsilon_{un} - \varepsilon_{pl}} \right)^2 \quad (4.16)$$

Reloading is assumed to occur along a straight line passing through the reloading point from the unloading curve  $(\varepsilon_{r0}, \sigma_{r0})$  and the returning point  $(\varepsilon_{re}, \sigma_{re})$ , which coincides with the unloading from the envelope point  $(\varepsilon_{un}, \sigma_{un})$ . For strains smaller than the strain  $\varepsilon_{un}$  at which unloading from the envelope commences, a straight line is fitted between the reloading point  $(\varepsilon_{r0}, \sigma_{r0})$  and the degrading strength point  $(\varepsilon_{new}, \sigma_{new})$ . For

strains larger than  $\varepsilon_{un}$ , a straight line is fitted between the reduced strength point  $(\varepsilon_{new}, \sigma_{new})$  and the returning point  $(\varepsilon_{re}, \sigma_{re})$ . The inconvenience of such a formulation (i.e., significant increase in computer based computation time when modeling involves a large number of elements) and the fact that empirical data used have not been verified for HSC, led to simplification of the reloading branch, as illustrated in **Figure 4.4**.

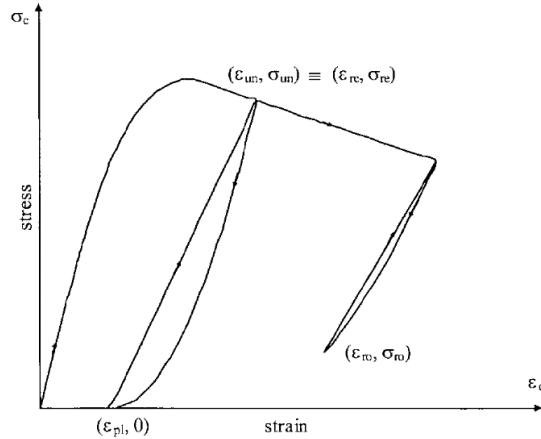


**Figure 4.4** Reloading branches.

*Source: Konstantinidis, Kappos, & Izzuddin (2007).*

The relationship for tensile concrete stress ( $\sigma_{ct}$ ), when unloading from a compressive branch is given by

$$\sigma_{ct} = f'_{ct} \left( 1 - \frac{\varepsilon_{pl}}{\varepsilon_{ccl}} \right) \quad (4.17)$$

where  $f'_{ct}$  is the tensile concrete strength. If  $\varepsilon_{pl} > \varepsilon_{ccl}$  then  $\sigma_{ct} = 0$  and when  $\varepsilon_{pl} < \varepsilon_{ccl}$ , the stress-strain relation becomes

$$\sigma_c = E_t (\varepsilon_c - \varepsilon_{pl}) \quad (4.18)$$

where

$$E_t = \frac{\sigma_{ct}}{\varepsilon_t} \quad (4.19)$$

$$\varepsilon_t = \frac{f'_{ct}}{E_c} \quad (4.20)$$

When the tensile strain is exceeded for any corresponding tensile strength, *i.e.*,  $\varepsilon_t > (\varepsilon_t - \varepsilon_{pl})$ , cracks open and the tensile strength of the concrete for the subsequent loading is assumed to be zero (**Figure 4.5**).

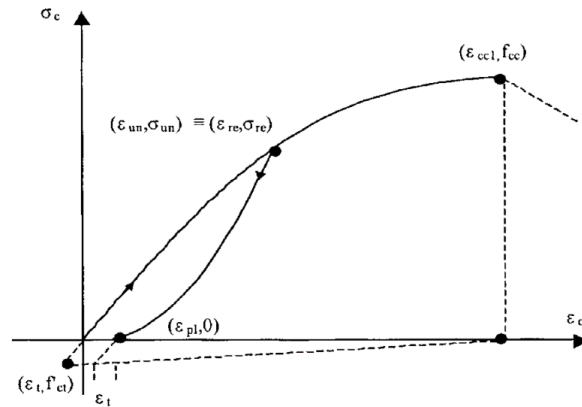


**Figure 4.5** Deterioration in tensile concrete strength due to prior compression loading.

Source: Konstantinidis, Kappos, & Izzuddin (2007).

#### 4.2.2.2 Stress-Strain Relationship for Steel.

In this study, a kinematic hardening model (Bahn (1994)) was employed to describe the cyclic stress-strain relationships for steel reinforcement. The elastic range was assumed to be unchanged during strain hardening. The center of the elastic region moved along the straight line *aa'* (see **Figure 4.6**). The envelope curve was determined by subjecting the steel reinforcement to a tensile test under a monotonically increasing load until failure. The unloading and reloading curves follow along a stress-strain path that is generally assumed to be parallel to the initial elastic portion of the curve. Thus, it is assumed that no stiffness degradation occurs as seen in **Figure 4.6**.

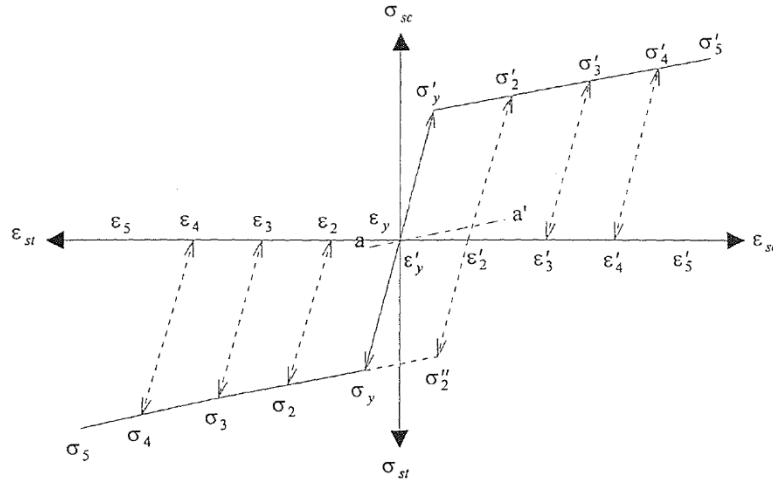


**Figure 4.6** Idealized cyclic stress-strain curve for steel.

*Source: Bahn (1994).*

### 4.2.3 Extended Finite Segment Method for Analysis

The original numerical procedures proposed by Tsao (1991) have been modified in this Chapter. In this modified computer analysis, the column was considered as a three dimensional structure after segmentation. The column section was divided into small elements of reinforcement and concrete in order to calculate the cross-sectional stiffness at different levels of strain. The analysis was based on the behavior of the cross-section at each segment point along the column. The modified computer analysis was based on the following assumptions:

1. Plane sections remain plane before and after bending.
2. There exists a perfect bond between concrete and steel.
3. No twisting occurs and the effects of axial and shear deformation are ignored.
4. Effects of creep and shrinkage are neglected.
5. There is no initial deflection in the undeformed columns.

The cross section of any slender column can be divided into several small elements as shown in **Figure 4.7**. Using the assumption that plane sections remain plane

during bending, the strained plane in the cross-section can be described by the strain at the coordinate origin  $\epsilon_0$ , as well as curvatures  $\phi_x$ , and  $\phi_y$  about both axes, respectively. Thus the strain  $\epsilon_k$  at any element  $k$  under combined biaxial bending and axial compression is given by [Hsu (1974), Wang and Hsu (1990)]:

$$\epsilon_k = \epsilon_0 + \phi_x y_k + \phi_y x_k \quad (4.21)$$

where

$\epsilon_0$ : strain at the coordinate origin.

$\phi_x$ : curvature produced by bending moment  $M_x$ .

$\phi_y$ : curvature produced by bending moment  $M_y$ .

$M_x$  and  $M_y$ : moment about the x-axis and y-axis, respectively.

$x_k$  and  $y_k$ : coordinates of the centroid of an element  $k$  relative to both principal axes X and Y, respectively.

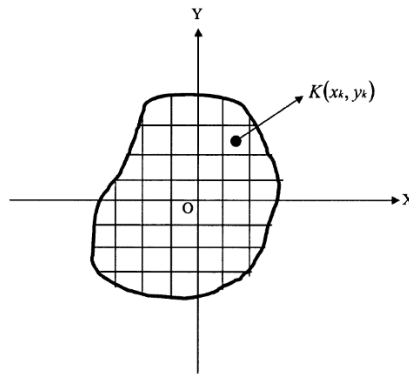


**Figure 4.7** Cross section and coordinate system.

*Source: Chen, J. (2005).*

For any value of strain  $\epsilon_k$ , a value of the secant modulus of elasticity  $E_{sk}$  can be found by an idealized stress-strain relationship of the steel reinforcement or concrete elements. The equilibrium equations for a in the cross section with  $n$  elements subjected



to axial load  $P_c$ , and bending moments  $M_{xc}$ , and  $M_{yc}$  can be expressed in the following forms:

$$P_c = \sum_{k=1}^n E_{sk} \epsilon_k a_k \quad (4.22)$$

$$M_{xc} = \sum_{k=1}^n E_{sk} \epsilon_k a_k y_k \quad (4.23)$$

$$M_{yc} = \sum_{k=1}^n E_{sk} \epsilon_k a_k x_k \quad (4.24)$$

where  $a_k$  is a small area of a discrete element  $k$  where subscript  $c$  denotes the calculated values in an iteration cycle.

Considering Equations (4.23) and (4.24) for calculated moments  $M_{xc}$ , and  $M_{yc}$ , the formulas are only valid when the areas of divided elements are comparatively small. This implies that the mechanical behavior of a unit element should be estimated more accurately. Thus, Equations (4.25) and (4.26) have been used here to reduce an accumulation of error when at coarse mesh is used for analyzing the column section.

$$M_{xc} = \sum_{k=1}^n E_{sk} \epsilon_k a_k y_k + \sum_{k=1}^n \phi_x E_{sk} I'_{x_0k} \quad (4.25)$$

$$M_{yc} = \sum_{k=1}^n E_{sk} \epsilon_k a_k x_k + \sum_{k=1}^n \phi_y E_{sk} I'_{y_0k} \quad (4.26)$$

where  $I'_{x_0k}$  and  $I'_{y_0k}$  are the moments of inertia (second moment) of an element  $k$  about the elemental centroidal  $x_o$  and  $y_o$  axes which are parallel to both reference  $x$  and  $y$  axes, respectively (**Figure 4.8**).

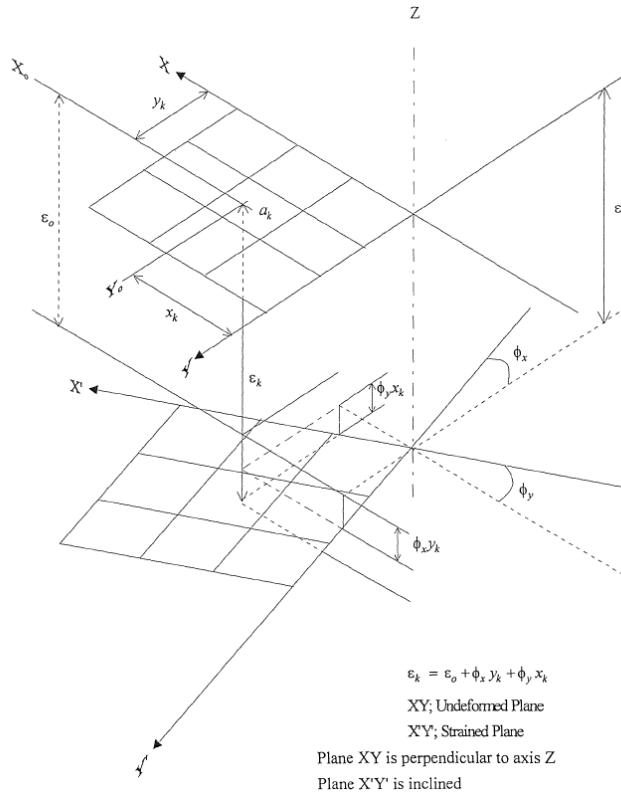


**Figure 4.8** Strain plane of combined biaxial bending and axial load.  
*Source: Bahn (1994).*

Substituting Equation (4.21) in Equations (4.22), (4.25), and (4.26), one has the following matrix form:

$$\begin{Bmatrix} P_c \\ M_{xc} \\ M_{yc} \end{Bmatrix} = \begin{bmatrix} \sum_{k=1}^n E_{sk} a_k & \sum_{k=1}^n E_{sk} a_k y_k & \sum_{k=1}^n E_{sk} a_k x_k \\ \sum_{k=1}^n E_{sk} a_k y_k & \sum_{k=1}^n (a_k y_k^2 + I'_{x_0 k}) E_{sk} & \sum_{k=1}^n E_{sk} a_k x_k y_k \\ \sum_{k=1}^n E_{sk} a_k x_k & \sum_{k=1}^n E_{sk} a_k x_k y_k & \sum_{k=1}^n (a_k x_k^2 + I'_{y_0 k}) E_{sk} \end{bmatrix} \begin{Bmatrix} \epsilon_0 \\ \phi_x \\ \phi_y \end{Bmatrix} \quad (4.27)$$

and let

$$C_{11} = \sum_{k=1}^n E_{sk} a_k \quad (4.28)$$

$$C_{12} = C_{21} = \sum_{k=1}^n E_{sk} a_k y_k \quad (4.29)$$

$$C_{13} = C_{31} = \sum_{k=1}^n E_{sk} a_k x_k \quad (4.30)$$

$$C_{22} = \sum_{k=1}^n (a_k y_k^2 + I'_{x_0k}) E_{sk} \quad (4.31)$$

$$C_{23} = C_{32} = \sum_{k=1}^n E_{sk} a_k x_k y_k \quad (4.32)$$

$$C_{33} = \sum_{k=1}^n (a_k x_k^2 + I'_{y_0k}) E_{sk} \quad (4.33)$$

For a short column, we can directly use Equation (4.27) due to the negligible effects of deflection. For a slender column, however, second order effects must be taken into account. Let  $d_x$  and  $d_y$  represent the deflections of the column in the  $x$  and  $y$  axis, respectively. Equation (4.27) becomes:

$$\begin{Bmatrix} P_c \\ P_c(e_y + d_y) \\ P_c(e_x + d_x) \end{Bmatrix} = \begin{bmatrix} C_{11} & C_{12} & C_{13} \\ C_{21} & C_{22} & C_{23} \\ C_{31} & C_{32} & C_{33} \end{bmatrix} \begin{Bmatrix} \epsilon_0 \\ \phi_x \\ \phi_y \end{Bmatrix} \quad (4.34)$$

The general formula of the graph curvature relates the curvature of the column to its lateral displacement derivations:

$$\frac{y''}{(1 + y'^2)^{3/2}} = -\phi \quad (4.35)$$

In previous studies, the lateral displacements of the column were assumed to be small, so that the total curvature in the two major bending planes could be represented in the form of second derivatives of the displacement ( $y'' = -\phi$ ). In this study, however, the first derivative of the displacement in the denominator of the curvature has been considered. This results in more accurate results, especially due to the large deflection at the center of the column following crack development.

By defining  $A$  and  $B$  as functions of  $y'$  with respect to  $y$  and  $x$  directions

$$A_{(i)} = \left(1 + y'_{y(i)}\right)^{3/2} \quad (4.36)$$

$$B_{(i)} = \left(1 + y'_{x(i)}\right)^{3/2} \quad (4.37)$$

Equation (4.35) can be written as:

$$y''_y = -\phi_x A \quad (4.38)$$

$$y''_x = -\phi_y B \quad (4.39)$$

The finite difference method is hereby introduced to solve the three dimensional behavior of columns. As shown in **Figure 4.9**, slender columns have been divided into several segments. The fundamental basis of this method is to replace the differential equation of the deflection curve by its finite difference approximation, and then to algebraically solve the finite difference equations obtained at several segments along the column. For the segment ( $i$ ) with a length of  $SL$ :

$$\frac{d^{y(i+1)} - d^{y(i-1)}}{2(SL)} = y'_{y(i)} \quad (4.40)$$

$$\frac{d^{x(i+1)} - d^{x(i-1)}}{2(SL)} = y'_{x(i)} \quad (4.41)$$

$$\frac{d^{y(i+1)} - 2d^{y(i)} + d^{y(i-1)}}{(SL)^2} = y''_{y(i)} \quad (4.42)$$

$$\frac{d^{x(i+1)} - 2d^{x(i)} + d^{x(i-1)}}{(SL)^2} = y''_{x(i)} \quad (4.43)$$

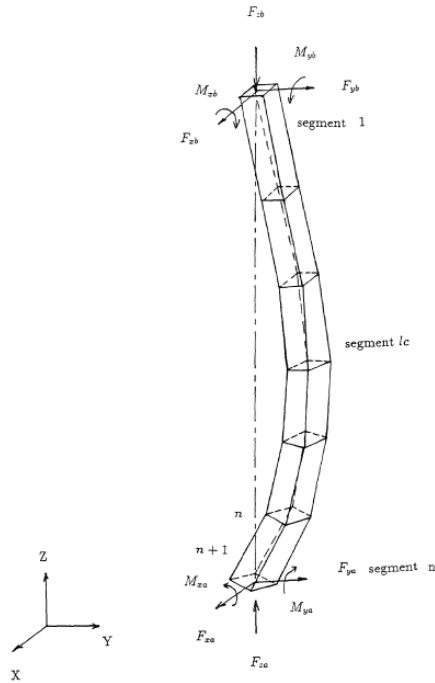


**Figure 4.9** Column divided into  $n$  segments.

Substituting Equations (4.38) and (4.39) into Equations (4.42) and (4.43), one has the following:

$$\frac{d^{y(i+1)} - 2d^{y(i)} + d^{y(i-1)}}{A_{(i)}(SL)^2} = -\phi_{x(i)} \quad (4.44)$$

$$\frac{d_{x(i+1)} - 2d_{x(i)} + d_{x(i-1)}}{B_{(i)}(SL)^2} = -\phi_{y(i)} \quad (4.45)$$

Incorporating Equations (4.44) and (4.45) into Equation (4.34), one has

$$\begin{Bmatrix} P_c \\ P_c(e_y + d_y) \\ P_c(e_x + d_x) \end{Bmatrix} = \begin{bmatrix} C_{11} & C_{12} & C_{13} \\ C_{21} & C_{22} & C_{23} \\ C_{31} & C_{32} & C_{33} \end{bmatrix} \begin{Bmatrix} \epsilon_0 \\ \frac{d_{y(i+1)} - 2d_{y(i)} + d_{y(i-1)}}{A_{(i)}(SL)^2} \\ \frac{d_{x(i+1)} - 2d_{x(i)} + d_{x(i-1)}}{B_{(i)}(SL)^2} \end{Bmatrix} \quad (4.46)$$

By expanding and rearranging Equation (4.46) for segment  $(i)$ , it can be written

as:

$$(SL)^2 \begin{Bmatrix} P_c \\ P_c(e_y + d_y) \\ P_c(e_x + d_x) \end{Bmatrix} = \begin{bmatrix} (SL)^2 C_{11(i)} & -C_{12(i)} & -C_{13(i)} & 2C_{12(i)} & 2C_{13(i)} & -C_{12(i)} & -C_{13(i)} \\ (SL)^2 C_{21(i)} & -C_{22(i)} & -C_{23(i)} & 2C_{22(i)} & 2C_{23(i)} & -C_{22(i)} & -C_{23(i)} \\ (SL)^2 C_{31(i)} & -C_{32(i)} & -C_{33(i)} & 2C_{32(i)} & 2C_{33(i)} & -C_{32(i)} & -C_{33(i)} \end{bmatrix} \begin{Bmatrix} \epsilon_0 \\ \frac{d_{y(i-1)}}{A_{(i)}} \\ \frac{d_{x(i-1)}}{B_{(i)}} \\ \frac{d_{y(i)}}{A_{(i)}} \\ \frac{d_{x(i)}}{B_{(i)}} \\ \frac{d_{y(i+1)}}{A_{(i)}} \\ \frac{d_{x(i+1)}}{B_{(i)}} \end{Bmatrix} \quad (4.47)$$

$$(SL)^2 \begin{Bmatrix} P_c \\ P_c(e_y + d_y) \\ P_c(e_x + d_x) \end{Bmatrix} = \quad (4.48)$$

$$\begin{bmatrix}
0 & -\frac{C_{12(i)}}{A_{(i)}} & -\frac{C_{13(i)}}{B_{(i)}} & (SL)^2 C_{11(i)} & 2\frac{C_{12(i)}}{A_{(i)}} & 2\frac{C_{13(i)}}{B_{(i)}} & 0 & -\frac{C_{12(i)}}{A_{(i)}} & -\frac{C_{13(i)}}{B_{(i)}} \\
0 & -\frac{C_{22(i)}}{A_{(i)}} & -\frac{C_{23(i)}}{B_{(i)}} & (SL)^2 C_{12(i)} & 2\frac{C_{22(i)}}{A_{(i)}} & 2\frac{C_{23(i)}}{B_{(i)}} & 0 & -\frac{C_{22(i)}}{A_{(i)}} & -\frac{C_{23(i)}}{B_{(i)}} \\
0 & -\frac{C_{32(i)}}{A_{(i)}} & -\frac{C_{33(i)}}{B_{(i)}} & (SL)^2 C_{13(i)} & 2\frac{C_{32(i)}}{A_{(i)}} & 2\frac{C_{33(i)}}{B_{(i)}} & 0 & -\frac{C_{32(i)}}{A_{(i)}} & -\frac{C_{33(i)}}{B_{(i)}}
\end{bmatrix}
\begin{pmatrix}
\epsilon_{0(i-1)} \\
\frac{d_{y(i-1)}}{A_{(i)}} \\
\frac{d_{x(i-1)}}{B_{(i)}} \\
\epsilon_{0(i)} \\
\frac{d_{y(i)}}{A_{(i)}} \\
\frac{d_{x(i)}}{B_{(i)}} \\
\epsilon_{0(i+1)} \\
\frac{d_{y(i+1)}}{A_{(i)}} \\
\frac{d_{x(i+1)}}{B_{(i)}}
\end{pmatrix}$$

Let

$$J_{(i)} = \begin{bmatrix}
0 & -\frac{C_{12(i)}}{A_{(i)}} & -\frac{C_{13(i)}}{B_{(i)}} \\
0 & -\frac{C_{22(i)}}{A_{(i)}} & -\frac{C_{23(i)}}{B_{(i)}} \\
0 & -\frac{C_{32(i)}}{A_{(i)}} & -\frac{C_{33(i)}}{B_{(i)}}
\end{bmatrix} \quad (4.49)$$

$$H_{(i)} = \begin{bmatrix}
(SL)^2 C_{11(i)} & 2\frac{C_{12(i)}}{A_{(i)}} & 2\frac{C_{13(i)}}{B_{(i)}} \\
(SL)^2 C_{12(i)} & 2\frac{C_{22(i)}}{A_{(i)}} & 2\frac{C_{23(i)}}{B_{(i)}} \\
(SL)^2 C_{13(i)} & 2\frac{C_{32(i)}}{A_{(i)}} & 2\frac{C_{33(i)}}{B_{(i)}}
\end{bmatrix} \quad (4.50)$$

The boundary conditions for the pinned-ended column are  $d_{y(1)} = d_{x(1)} = 0$  and

$d_{y(n+1)} = d_{x(n+1)} = 0$ . Adding  $i = 2$  to  $i = n$ , one has

$$\begin{aligned}
 & (SL)^2 P_c \left\{ \begin{array}{c} 1 \\ e_y + d_{y(2)} \\ e_x + d_{x(2)} \\ \vdots \\ 1 \\ e_y + d_{y(i)} \\ e_x + d_{x(i)} \\ \vdots \\ 1 \\ e_y + d_{y(n)} \\ e_x + d_{x(n)} \end{array} \right\} = \\
 & \left[ \begin{array}{cccccccc} H_{(2)} & J_{(2)} & & & & & & \\ J_{(3)} & H_{(3)} & J_{(3)} & & & & & \\ & J_{(4)} & H_{(4)} & J_{(4)} & & & & \\ & & \ddots & \ddots & \ddots & & & \\ & & & J_{(i)} & H_{(i)} & J_{(i)} & & \\ & & & & \ddots & \ddots & \ddots & \\ & & & & & J_{(n-1)} & H_{(n-1)} & J_{(n-1)} \\ & & & & & & J_{(n)} & H_{(n)} \end{array} \right] \left\{ \begin{array}{c} \epsilon_{0(2)} \\ d_{y(2)} \\ d_{x(2)} \\ \vdots \\ \epsilon_{0(i)} \\ d_{y(i)} \\ d_{x(i)} \\ \vdots \\ \epsilon_{0(n)} \\ d_{y(n)} \\ d_{x(n)} \end{array} \right\} \quad (4.51)
 \end{aligned}$$

For the symmetrical case, the analysis can be simplified by letting  $NC = (n / 2) + 1$  (where  $n$  is the number of column segments and  $NC$  is the node number at the middle of the column),  $d_{y(NC+1)} = d_{y(NC-1)}$ ,  $d_{x(NC+1)} = d_{x(NC-1)}$ , and  $\epsilon_{0(NC+1)} = \epsilon_{0(NC-1)}$ .

Equation (4.51) can be expressed as the following:



$$\begin{aligned}
 & (SL)^2 P_c \left\{ \begin{array}{c} 1 \\ e_y + d_{y(2)} \\ e_x + d_{x(2)} \\ \vdots \\ 1 \\ e_y + d_{y(i)} \\ e_x + d_{x(i)} \\ \vdots \\ 1 \\ e_y + d_{y(NC)} \\ e_x + d_{x(NC)} \end{array} \right\} = \\
 & \left[ \begin{array}{cccccccc} H_{(2)} & J_{(2)} & & & & & & \\ J_{(3)} & H_{(3)} & J_{(3)} & & & & & \\ & J_{(4)} & H_{(4)} & J_{(4)} & & & & \\ & & \ddots & \ddots & \ddots & & & \\ & & & J_{(i)} & H_{(i)} & J_{(i)} & & \\ & & & & \ddots & \ddots & \ddots & \\ & & & & & J_{(NC-1)} & H_{(NC-1)} & J_{(NC-1)} \\ & & & & & & 2J_{(NC)} & H_{(NC)} \end{array} \right] \left\{ \begin{array}{c} \epsilon_{0(2)} \\ d_{y(2)} \\ d_{x(2)} \\ \vdots \\ \epsilon_{0(i)} \\ d_{y(i)} \\ d_{x(i)} \\ \vdots \\ \epsilon_{0(NC)} \\ d_{y(NC)} \\ d_{x(NC)} \end{array} \right\} \quad (4.52)
 \end{aligned}$$

Select the deflection  $d_{y(NC)}$  as the control increment for each iteration step and interchange  $d_{y(NC)}$  and  $P_c$  from Equation (4.52), thus yielding

$$-d_{y(NC)} \left\{ \begin{array}{c} 0 \\ 0 \\ 0 \\ \vdots \\ \frac{C_{12(NC-1)}}{A_{(NC-1)}} \\ \frac{C_{22(NC-1)}}{A_{(NC-1)}} \\ \frac{C_{32(NC-1)}}{A_{(NC-1)}} \\ 2 \frac{C_{12(NC)}}{A_{(NC)}} \\ 2 \frac{C_{22(NC)}}{A_{(NC)}} \\ 2 \frac{C_{32(NC)}}{A_{(NC)}} \end{array} \right\} = \quad (4.53)$$

$$\left[ \begin{array}{ccc} H_{(2)} & J_{(2)} & \dots \\ \vdots & \vdots & \\ \dots & (SL)^2 C_{11(NC)} & -SL^2 \\ \dots & (SL)^2 C_{12(NC)} & -SL^2(e_y + d_{y(NC)}) \\ \dots & (SL)^2 C_{13(NC)} & -SL^2(e_x + d_{x(NC)}) \end{array} \right] \left[ \begin{array}{ccc} -SL^2 & 0 & \\ -SL^2(e_y + d_{y(2)}) & 0 & \\ -SL^2(e_x + d_{x(2)}) & 0 & \\ \vdots & \vdots & \vdots \\ -SL^2 & 2 \frac{C_{13(NC)}}{B_{(NC)}} & \\ -SL^2(e_y + d_{y(NC)}) & 2 \frac{C_{23(NC)}}{B_{(NC)}} & \\ -SL^2(e_x + d_{x(NC)}) & 2 \frac{C_{33(NC)}}{B_{(NC)}} & \end{array} \right] \left\{ \begin{array}{c} \epsilon_{0(2)} \\ d_{y(2)} \\ d_{x(2)} \\ \vdots \\ \epsilon_{0(i)} \\ d_{y(i)} \\ d_{x(i)} \\ \vdots \\ \epsilon_{0(NC)} \\ P_c \\ d_{x(NC)} \end{array} \right\}$$

Define vectors  $F$  and  $X$  and the matrix  $K$ :

$$F = -d_{y(NC)} \left\{ \begin{array}{c} 0 \\ 0 \\ 0 \\ \vdots \\ \frac{C_{12(NC-1)}}{A_{(NC-1)}} \\ \frac{C_{22(NC-1)}}{A_{(NC-1)}} \\ \frac{C_{32(NC-1)}}{A_{(NC-1)}} \\ 2 \frac{C_{12(NC)}}{A_{(NC)}} \\ 2 \frac{C_{22(NC)}}{A_{(NC)}} \\ 2 \frac{C_{32(NC)}}{A_{(NC)}} \end{array} \right\} \quad (4.54)$$

$$X = \left\{ \begin{array}{c} \epsilon_{0(2)} \\ d_{y(2)} \\ d_{x(2)} \\ \vdots \\ \epsilon_{0(i)} \\ d_{y(i)} \\ d_{x(i)} \\ \vdots \\ \epsilon_{0(NC)} \\ P_c \\ d_{x(NC)} \end{array} \right\} \quad (4.55)$$

$$K = \begin{bmatrix} H_{(2)} & J_{(2)} & \cdots & & -SL^2 & 0 \\ \vdots & \vdots & & & -SL^2(e_y + d_{y(2)}) & 0 \\ & & & & -SL^2(e_x + d_{x(2)}) & 0 \\ & & & \vdots & \vdots & \vdots \\ \cdots & (SL)^2 C_{11(NC)} & & -SL^2 & 2 \frac{C_{13(NC)}}{B_{(NC)}} \\ \cdots & (SL)^2 C_{12(NC)} & -SL^2(e_y + d_{y(NC)}) & & 2 \frac{C_{23(NC)}}{B_{(NC)}} \\ \cdots & (SL)^2 C_{13(NC)} & -SL^2(e_x + d_{x(NC)}) & & 2 \frac{C_{33(NC)}}{B_{(NC)}} \end{bmatrix} \quad (4.56)$$

Equation (4.52) becomes:

$$F = K X \quad (4.57)$$

#### 4.2.4 Incremental Procedure and Flowchart

In Equation (4.57), matrix  $K$  and vector  $F$  are functions of the displacement vector  $X$  due to first and second order effects of the slender column and nonlinear constitutive relationships of the column materials. An incremental approach using the secant modulus was used to solve the member stiffness equation. One reason to adopt the secant-modulus approach instead of the tangent-modulus approach is based on the fact that the secant-modulus approach allows for a more stable computation process and avoids divergence due to a small tangent stiffness of the section. In order to determine the entire load-deflection or moment-curvature curves, displacement or deformation may be chosen as

the incremental parameter. The complete, incremental path consists of many steps which correspond to individual points in plotting the entire curves (Wang, 1995).

The large deformation effect was taken into account by incorporating the first derivation of the slender column's lateral deformations into the curvature formula. Therefore, vector  $F$  and matrix  $K$  have to be updated not only for arrays that are affected by changes in element strain but also for changes in the segment lateral deformation. Thus, a more robust numerical solver was needed for this study than was available via previously available computer codes.

There was a need to develop a forecasting procedure to determine a more reasonable proposed starting value for the strain and displacement. Thus, the initial values for strain and deformation of the column segments at each step were calculated by extrapolation of the results of the previous steps. It should be noted that an inadequate difference in the strain components may cause a considerable change in the stress of the stress-strain curve. The extrapolated values are likely to be the answers of the next step in the iteration, especially when the column is still behaving linearly. In each step, an iterative process was repeatedly used until it reached convergence. The convergence was checked for three variables at each segment (one strain value and two lateral deformation values). Thus, at each iteration there were  $(3 \times NC) - 1$  equations needed in order to converge, with a determination of the solution following after convergence of all these equations. The differences between the result values and initial assumptions were calculated for each iteration. These differences must be smaller than the considered error limit. This guaranteed sufficient accuracy of the present computed solution. After satisfying the convergence criteria, the load  $P_c$ , deflections  $d_{x(i)}$ ,  $d_{y(i)}$  and strain at the

origin  $\varepsilon_{0(i)}$  were obtained. The biaxial bending moment  $M_{x(NC)}$ ,  $M_{y(NC)}$  at the middle segment can be calculated as follows:

$$M_{x(NC)} = P_c (e_y + d_{y(NC)}) \quad (4.58)$$

$$M_{y(NC)} = P_c (e_x + d_{x(NC)}) \quad (4.59)$$

In order to deal with loading or reloading and unloading, it is necessary to maintain a strain history for all the discrete elements along the column segments. As each successive solution is found, the strain in each element should be calculated and compared with the latest value in the strain history. If the current magnitude of strain is less than the strain history value, the unloading has occurred. If the magnitude of calculated strain is greater than the strain history value, the loading has occurred and the strain history is replaced by the current strain.

The incremental procedure was terminated when the strain at the point of extreme compressive bar reached the strain that corresponded to crushing of concrete. This was based on the assumption that crushing of the concrete at that moment was immediately followed by concrete spalling. Subsequently, buckling of the compression reinforcement occurred in a region where the concrete had spalled.

The flowchart of the present computational process used for RC slender columns is shown in **Appendix E**.

#### **4.2.5 Accuracy and Convergence**

Numerical solutions are approximate, thus their accuracy and convergence must be studied thoroughly. There are several possibilities that may cause computational errors.

Some of them affect the results very slightly and may be ignored. But some of these errors significantly affect the results and must be taken into account in the model. Modeling errors refer to the difference between a physical system and its mathematical model. It should be noted that, due to the small change of strain and deformation in this study, model components have to be sufficiently small in order to satisfy convergence criteria. The present slender RC column model was established based on assumptions given in Section 4.2.3. Previous studies from many researchers have shown that the errors due to these assumptions are minor and can be ignored. Therefore, discretization of the cross section and along the column represents the major sources of computational errors.

Errors can arise from the idealization of the cross section into elements in which the stress distribution pattern is approximately assumed. This error can be reduced by increasing the number of elements in the cross section.

Analysis of a slender column involves first and second order effects, so that the column has to be divided into finite segments for analysis. Accuracy can be improved as more segments are introduced to model the column.

Two reinforced concrete loading brackets, monolithic with the column and heavily reinforced to prevent premature failure, were provided at each end of the tested columns to assist with the application of biaxially eccentric loads. The effect of these brackets on the behavior of slender column was neglected in the present computer analysis.

In general, the present proposed procedures converge rapidly, especially where solutions being sought are in the ascending branch of load-deformation curve. However, there were occasions where the determinant of the matrix  $K$  approached zero which

caused numerical problems in determining the vector  $X$ . This was more likely to occur at the instance in which loading changed to unloading or vice versa. The determinant of the matrix  $K$  was calculated after this matrix was assembled in each iteration in the developed computer code. If this value was close to zero, new values for the strain and deformation components were considered. Another issue was that the number of iterations were not initially sufficient for some steps. As a solution to this problem, the steps were divided into smaller substeps to assure convergence.



### 4.3 Procedure of Numerical Analysis

The present computer program was written in MATLAB. This software utilizes a high-level programming language which is used by scientists and engineers worldwide. The developed computer model consisted of a main routine and two subroutines for concrete and steel stress-strain behavior.

The input data was created in an Excel file. This simplified changes in geometry and material properties values. The code then wrote the results of the analysis to a few output files. The analysis procedure is described in detail below:

1. Define all the variables used in the code.
2. Read the input file and save all the input values to corresponding variables.
3. Generate the coordinates and areas of discrete elements for each segment point along the column.
4. Estimate the initial deformations and strain of each segment point based on incremental deformation.
5. Calculate the first and second derivations of deformation with respect to each  $X$  and  $Y$  axes.
6. Calculate each elements strain based on the segments strain and curvatures.
7. Find element stresses and secant modulus corresponding to the calculated strains by calling the concrete and steel stress-strain behavior subroutines.
8. Calculate arrays of matrices  $C$ ,  $J$ , and  $H$ .
9. Assemble matrix  $K$  and vector  $F$ .
10. Solve for vector  $X$ .
11. Calculate differences (errors) between the assumed and solved values of strains and components of deformation for each segment point.
12. Proceed to stage 13 if the calculated errors are less than the maximum permitted error; otherwise perform another iteration starting at stage 6 and using recently solved values of strains and components of deformation.

13. Save strain, stress, components of deformation,  $P_c$ ,  $M_x$ , and  $M_y$  for this step.
14. Assume the saved values as initial values of the next stage and proceed to stage 5.

#### 4.4 Comparison of Experimental and Analytical Results

In this section, the validity of the developed computer model is confirmed by the comparison with the experimental results of the columns for the present study. Load-deflection and moment-curvature curves were computed using the proposed computer program. Based on the analysis results from Bahn (1994) and Tsao (1991), the number of segments selected only had a slight influence on the stress-strain curve of the slender column. They suggested that a column with eight segments would have the most satisfactory results. Therefore, a total of 16 segments along the column were used in this program. In previous studies, cross sections were divided into 64 members. In this computer code, however, 100 elements in the cross section were used. The representative stress in each element has been based upon the stress at the center of that element. Thus, a section with more elements resulted in higher accuracy due to the nonlinearity of the stress-strain behavior of the involved materials. **Figure 4.10** shows a general cross section of the slender column for computer analysis.

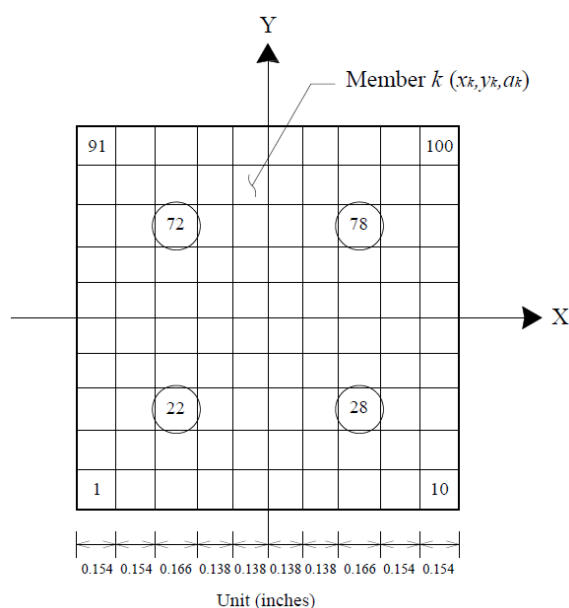


**Figure 4.10** Cross section of slender column for computer analysis.

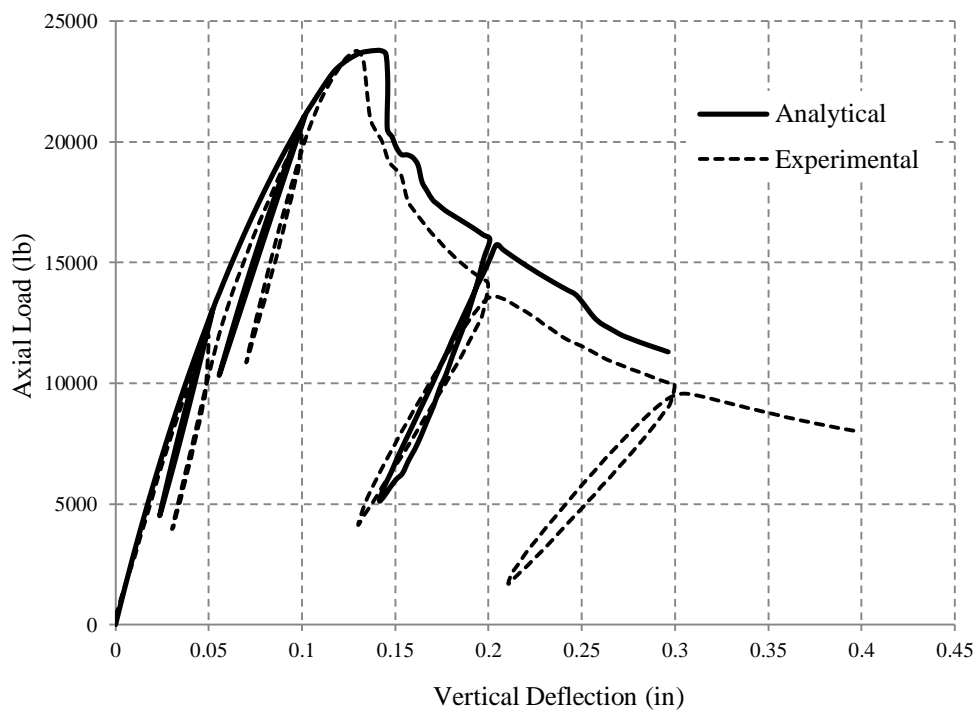


**Figure 4.11** Comparison of load-vertical deflection curves for column C6.

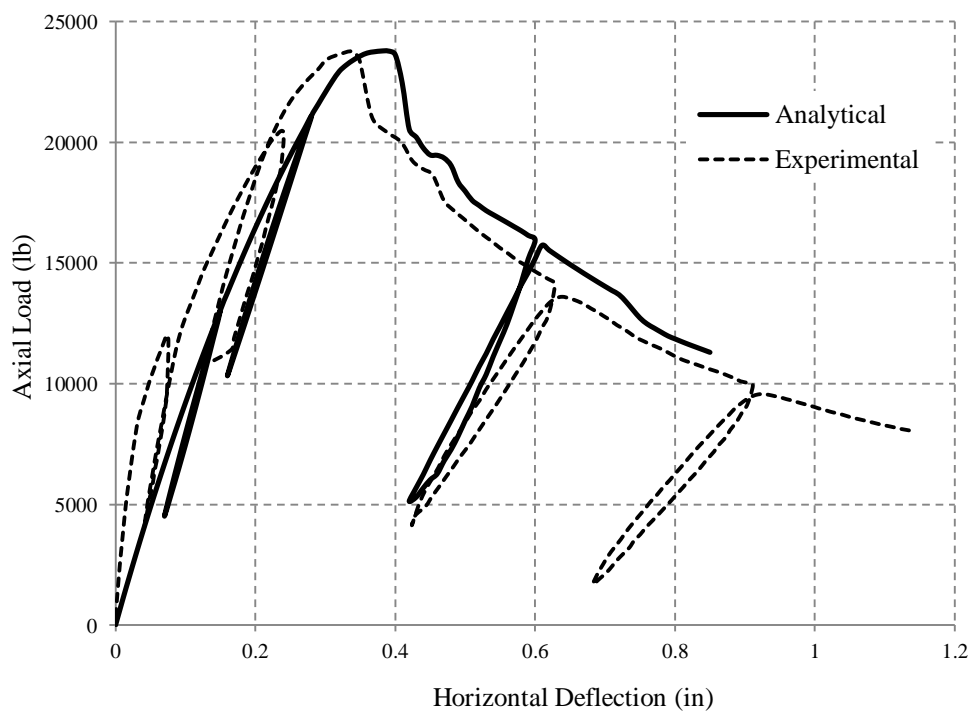


**Figure 4.12** Comparison of load-deflection curves in the X-direction for column C6.

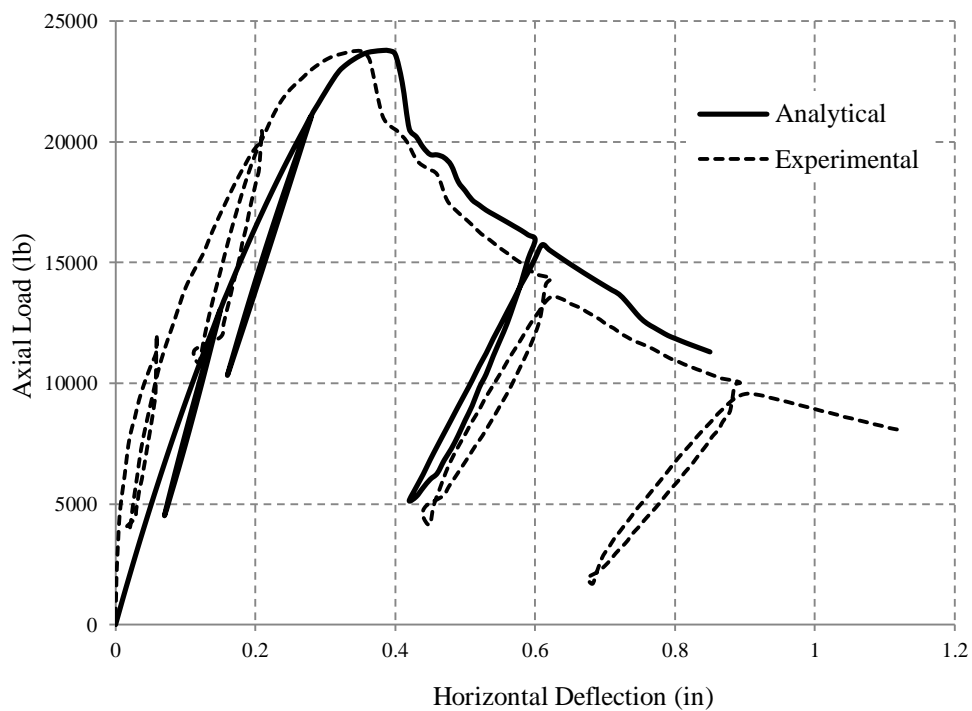


**Figure 4.13** Comparison of load-deflection curves in the Y-direction for column C6.

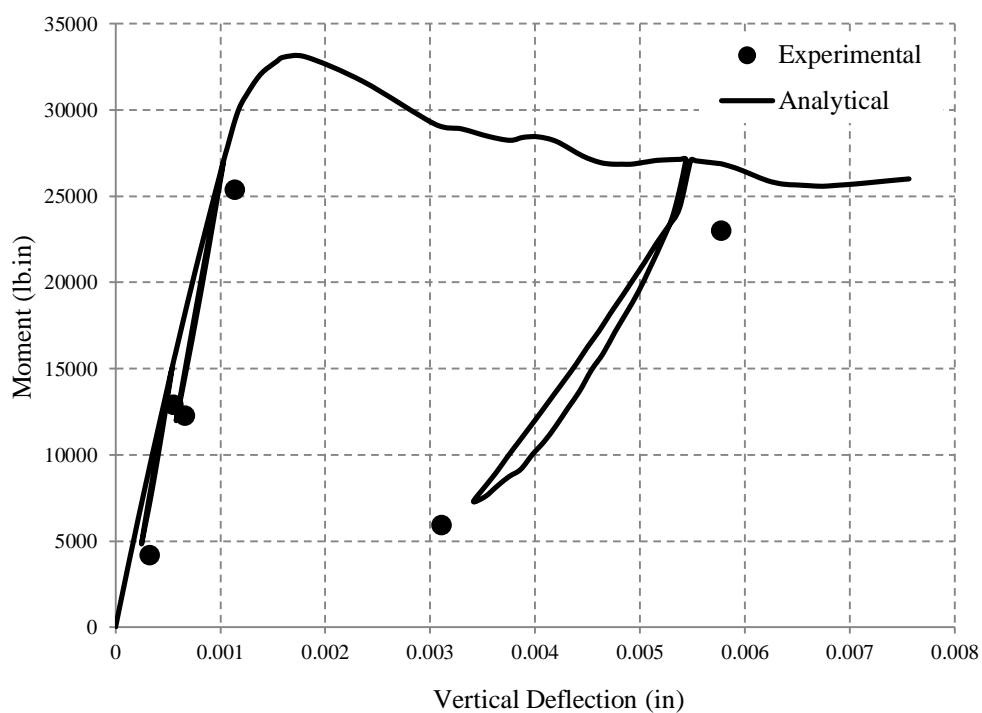


**Figure 4.14** Moment-curvature curve in the X-direction for column C6.

**Figure 4.11** to **Figure 4.14** gives the experimental versus analytical results for a typical column specimen (column C6). The comparisons for other specimens are listed in **Appendix D**. From the figures, the predicted curves from the present computer analysis are in an excellent agreement with the experimental results. The major difference between the experimental and analytical load-displacement graphs occurs at the descending branch. This discrepancy may be due to the bond deterioration in the column specimens. Additionally, the proposed stress-strain equation for high-strength concrete predicted a constant stress ( $0.3f_{cc}$ ) for strain values higher than the failure strain which caused the analytical results to be slightly higher than the experimental results for the descending branch. Also, the brittle failure of the column makes the measurement of the deflection and curvature a very difficult task after the peak load.

Four cycles of unloading and reloading have been considered for the present column experiments. Two of these cycles were within the linear portion of the column behavior which occurred before the peak load. The other two cycles occurred after the peak load. In the analysis, however, only three cycles were induced due to the fact that all the concrete elements surrounding the compression rebar crushed prior to the last cycle of loading-reloading. This is the criterion that indicates the failure of the column since the compression rebar begins to buckle at this point. The buckling of the compression rebar was observed in all tested columns.

The overall trend of experimental results in unloading-reloading cycles was satisfactorily simulated. For cycles that occur after the peak load, the unloading-reloading lines have a greater slope compared to the experimental results.

**Tables 4.1** and **4.2** present a comparison of maximum loads and moments between the experimental and analytical results. The comparison shows that the proposed analysis closely predicts the experimental maximum loads. The predicted ultimate loads were essentially equal to the experimental values with a 4% tolerance. The tolerance for the maximum predicted moments was 6%. It should be mentioned that the theoretical values of the maximum moments which were obtained through analysis need not necessarily be equal to the ultimate load due to second order effects. Therefore, one can conclude that the proposed computer analysis is valid and effective in analyzing high-strength reinforce concrete columns under combined cyclic axial loading with biaxial bending.

**Table 4.1** Maximum Axial Load and Corresponding Deflection Results

Tested Column	Experimental		Analytical		$P_{Exp.} / P_{Ana.}$
	$P$ (lb)	$d_x (d_y)$ (in)	$P$ (lb)	$d_x (d_y)$ (in)	
C1	11,100	0.46	10,659	0.40	1.04
C2	15,450	0.50	14,931	0.43	1.03
C3	12,846	0.52	15,688	0.47	0.82
C4	15,192	0.36	14,832	0.43	1.02
C5	22,652	0.31	22,639	0.37	1.00
C6	22,765	0.34	22,783	0.38	1.00

**Table 4.2** Maximum Moment Results

Tested Column	Experimental	Analytical	$M_{Exp.} / M_{Ana.}$
	$M_x (M_y)$ (lb.in)	$M_x (M_y)$ (lb.in)	
C1	21,809	20,485	1.06
C2	30,915	29,118	1.06
C3	26,348	30,820	0.85
C4	28,299	28,910	0.98
C5	29,549	31,209	0.95
C6	31,813	33,082	0.96



## **CHAPTER 5**

### **CONCLUSION**

A review of literature indicated that the behavior of CFRP strengthened concrete columns under cyclic loading had not been the subject of any previous work. Monotonic axial load with unidirectional eccentricity had been applied to predict the behavior of high-strength concrete columns in previous studies. The analysis of such columns under cyclic axial load and biaxial bending therefore needed to be carried out.

A simplified method was introduced to study the behavior of concrete columns with and without CFRP jackets under constant axial load and variable lateral load. The lateral load was applied both monotonically and cyclically. A computer code was developed to produce the moment-curvature diagram of any arbitrary section and which accounted for the nonlinear stress-strain relationship of concrete. The code assumed a bilinear behavior for reinforcing steel. The design-oriented stress-strain model for FRP-confined concrete by Teng, Jiang, Lam, and Luo (2009) was selected for use in this investigation. This model captures all the main characteristics of the stress-strain behavior of concrete confined by different types of FRP. Important factors including the actual hoop strains in FRP jackets at rupture, the sufficiency of FRP confinement for a significant strength enhancement, and the effect of jacket stiffness on the ultimate axial strain were examined and resolved in this model. Moment-curvature graphs of circular and rectangular columns tested by Seible, Priestley, Hegemier, and Innamorato (1997) have been depicted. These columns were wrapped with variable carbon fiber thicknesses along the column height. Moment-curvature graphs for tested columns sections showed

that CFRP jackets can increase the flexibility and strength of the column. Sections which were retrofitted with thicker layers of CFRP showed a more pronounced enhancement in the behavior of the concrete section. Additionally, the moment capacities of jacketed columns were increased 48% to 100% when the section was wrapped with 0.4 in-thick layer of CFRP.

Six 4-ft long slender columns were tested under combined axial load and biaxial bending. Silica fume was added to the mix to produce high-strength concrete. The compressive strength of the concrete in five of the columns was more than 18,000 psi while the remaining column was made of concrete with 7,250 psi compressive strength. The columns were reinforced with 4 - #3 longitudinal reinforcing bars with 12 gage wire stirrups spaced at 3 inches. The tests were performed using an MTS machine under stroke control. Steel ball bearings were placed at each end of the columns to simulate a pin-ended condition. The axial load was applied with the same eccentricities in both the X and Y directions. LVDTs were installed to determine the horizontal displacement at mid-height of the column. Additionally, six mechanical strain gages were mounted at two perpendicular sides of the column to measure vertical strains and curvature. The strain measurements were performed at the beginning of each loading or unloading ramp. Both the load-vertical deflection of the stroke and load-deflection of LVDTs of the specimens were recorded in this study. The failure occurred at the mid-height of the column due to concrete crushing and subsequent exposure and buckling of the longitudinal reinforcing bars.

A finite segment method of analysis was also developed to predict the behavior of RC slender columns under cyclic loading with bidirectional eccentricities. The

computational method considered the nonlinear behavior of the materials and included the second order effects due to the additional eccentricity of the applied axial load when the columns deformed laterally. In this study, a hysteretic stress-strain behavior of high-strength concrete (HSC) under reversed cyclic loading by Konstantinidis, Kappos, and Izzuddin (2007) was employed in order to describe the cyclic stress-strain relationships for concrete. This model explicitly accounted for the effects of concrete compressive strength, volumetric ratio of transverse reinforcement, yield strength of ties, tie spacing, and tie pattern. The envelope stress-strain curve of HSC under repeated or cyclic compressive loading nearly coincided with the stress-strain response under uniaxial loading. Thus, this computer code can be readily used for analysis of HSC columns under monotonic load as well. A kinematic hardening model was employed to describe the cyclic stress-strain relationships for steel reinforcement. Geometrical non-linearity was more accurately modeled by taking into account the first derivation of the column deflection in the curvature formula (Equation 4.35).

Compared to the actual experimental results, the proposed computer analysis was reasonably accurate in predicting the actual load-deformation behavior of the HSC slender column under combined axial loading and biaxial bending. Both the ascending and descending branches of the analytical curves have achieved a satisfactory agreement with the experimental results. It can be concluded that the proposed computer analysis is valid and can be used in practical engineering designs.

## **APPENDIX A**

### **STRESS-STRAIN CURVES OF STEEL BARS**

In Appendix A, each figure presents the experimental tensile stress-strain curves of steel bars used in this research. A total of three tests were conducted in the NJIT Structural Laboratory.

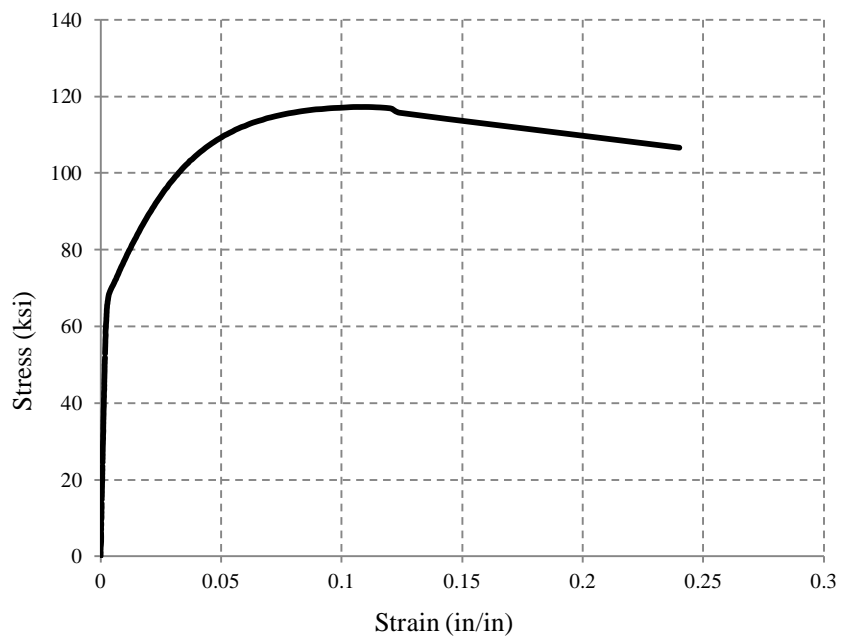


**Figure A.1** Stress-Strain curve of No. 3 bar (test1).

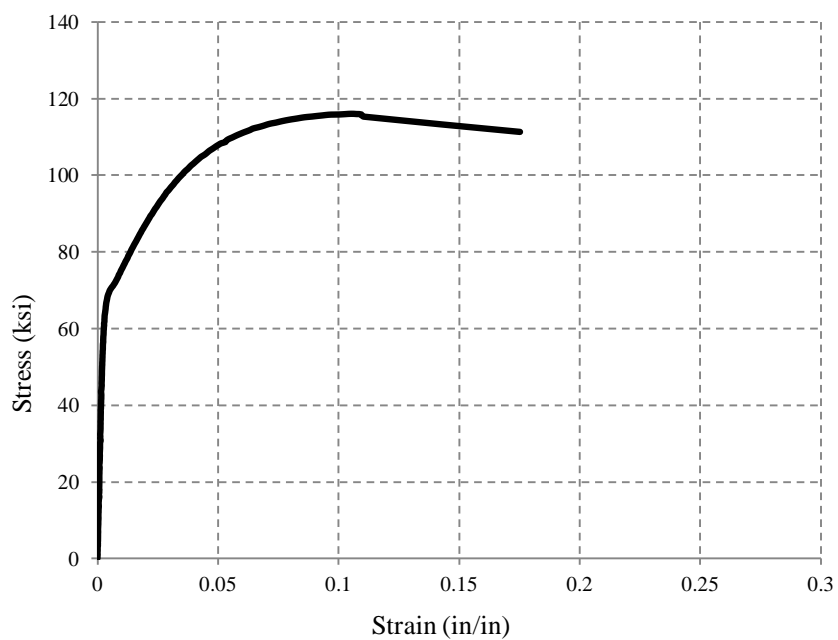


**Figure A.2** Stress-Strain curve of No. 3 bar (test2).

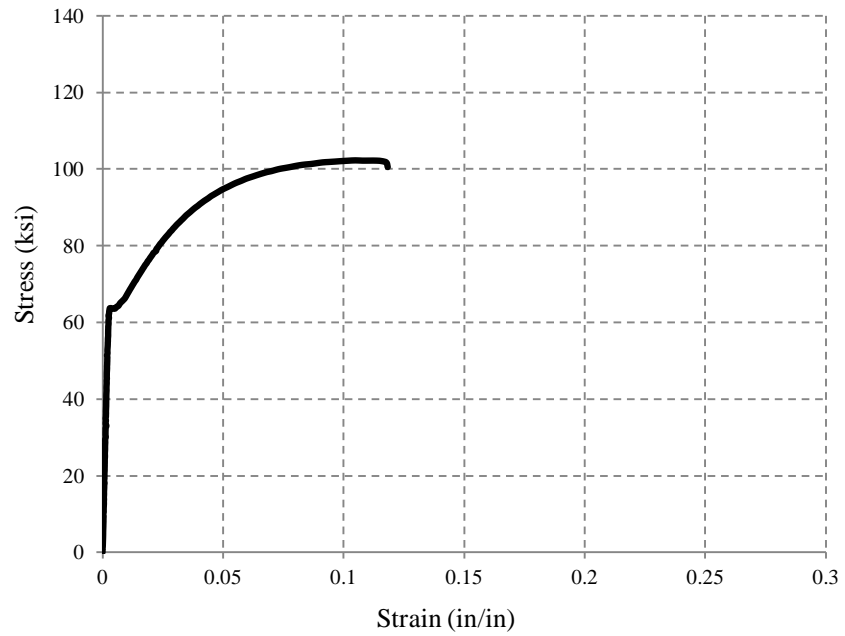


**Figure A.3** Stress-Strain curve of No. 3 bar (test3).

## **APPENDIX B**

### **STRAIN-POSITION CURVES FOR COLUMN SPECIMENS**

In Appendix B, **Figures B.1-B.12** present the experimental strain-position curves for the concrete column specimens.

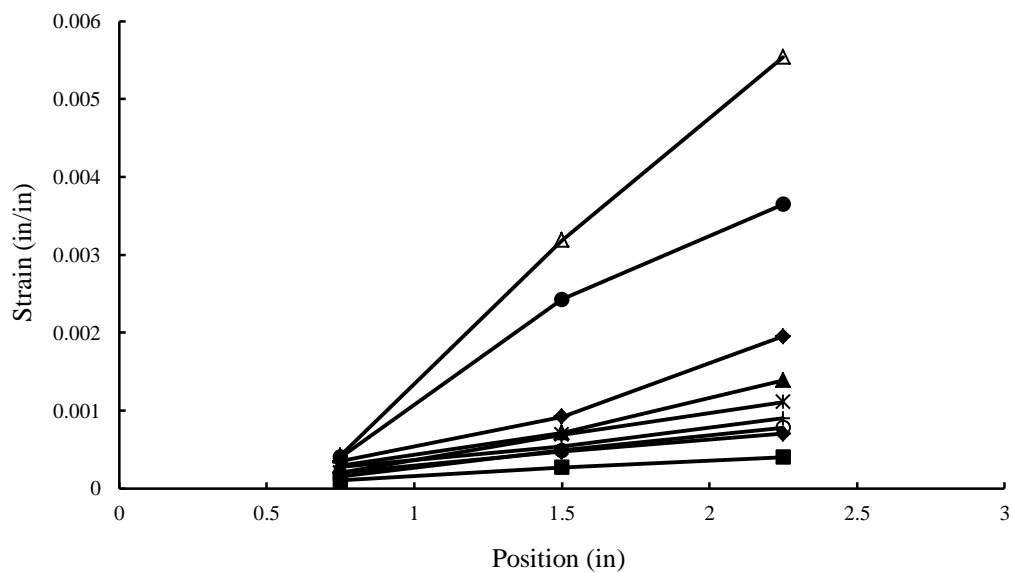


**Figure B.1** Strain-position curve for control column C1 in the X direction.

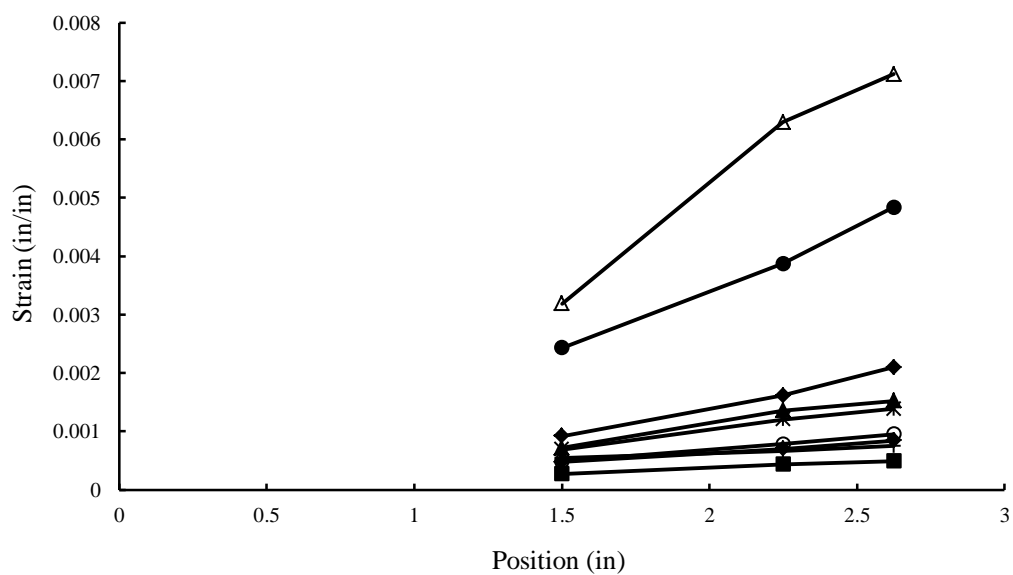


**Figure B.2** Strain-position curve for control column C1 in the Y direction.



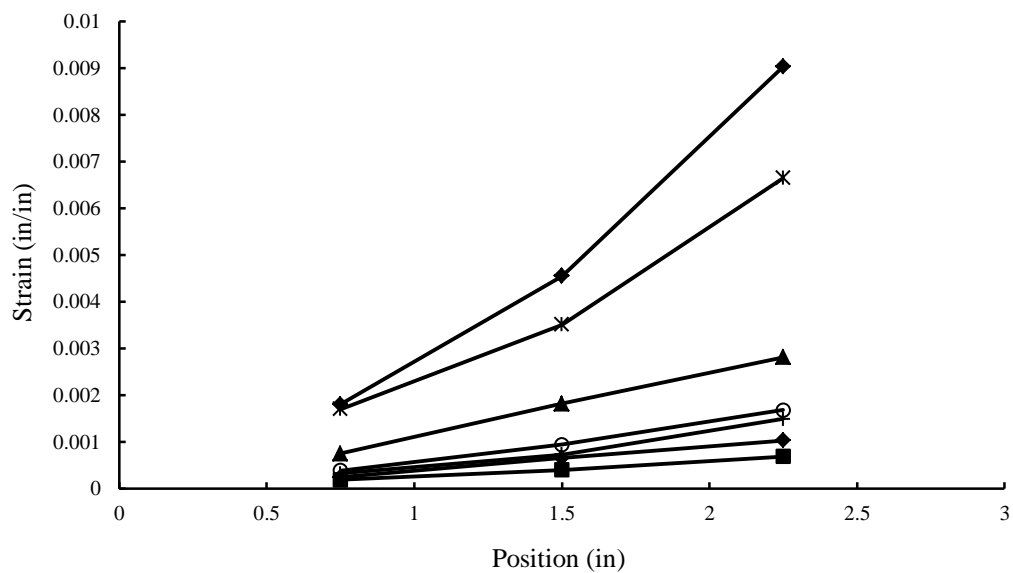


**Figure B.3** Strain-position curve for control column C2 in the X direction.

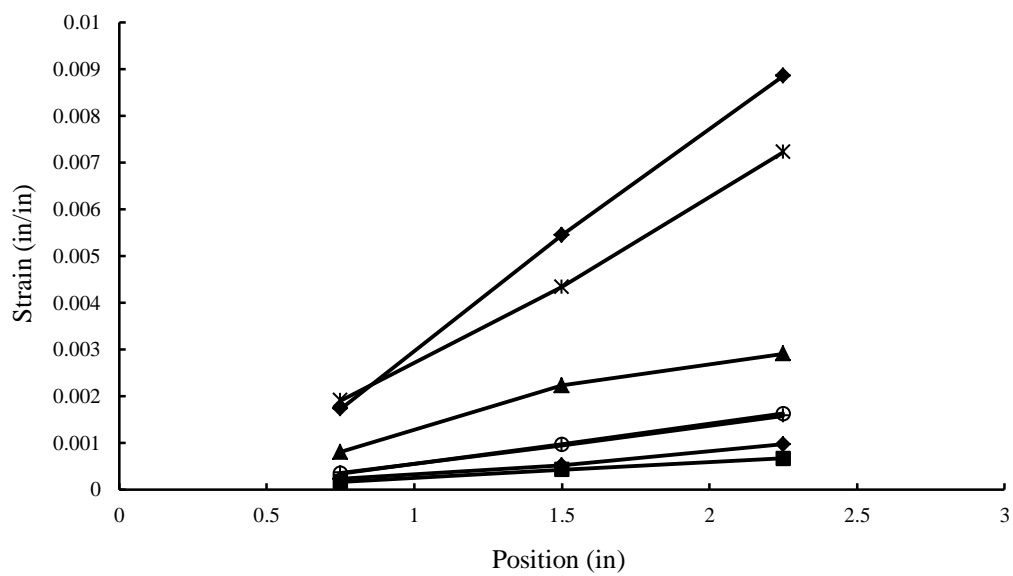


**Figure B.4** Strain-position curve for control column C2 in the Y direction.

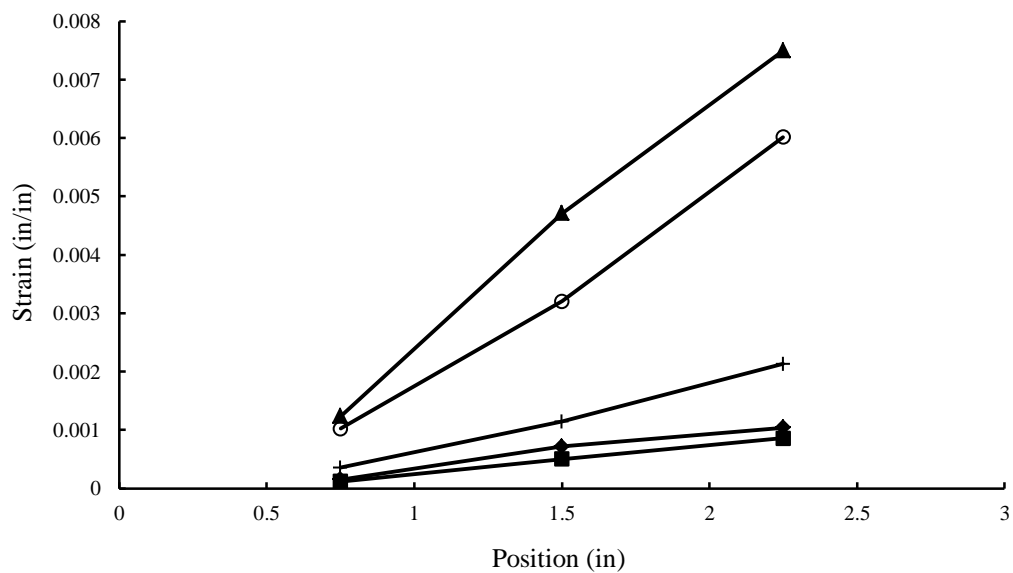


**Figure B.5** Strain-position curve for control column C3 in the X direction.

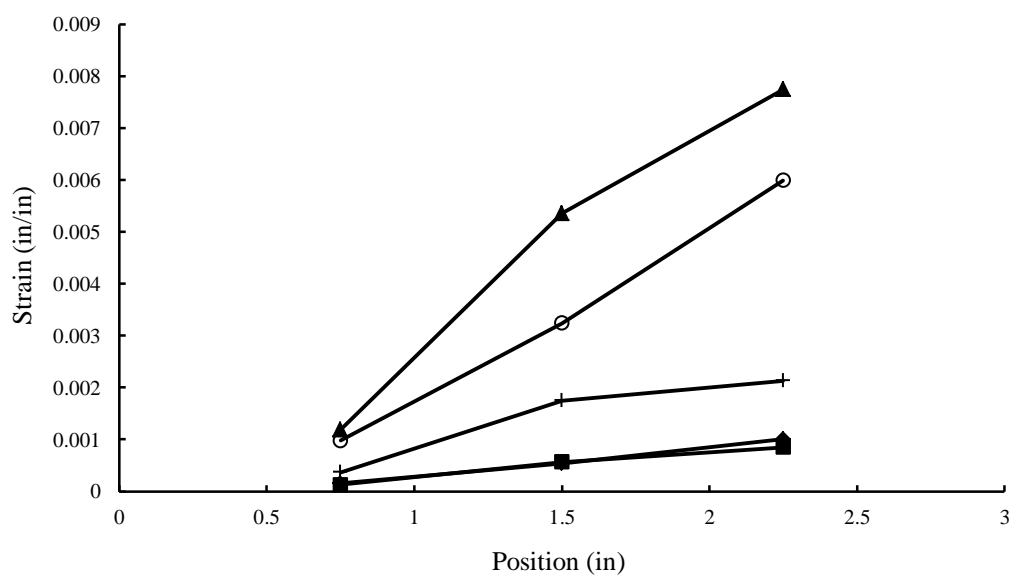


**Figure B.6** Strain-position curve for control column C3 in the Y direction.

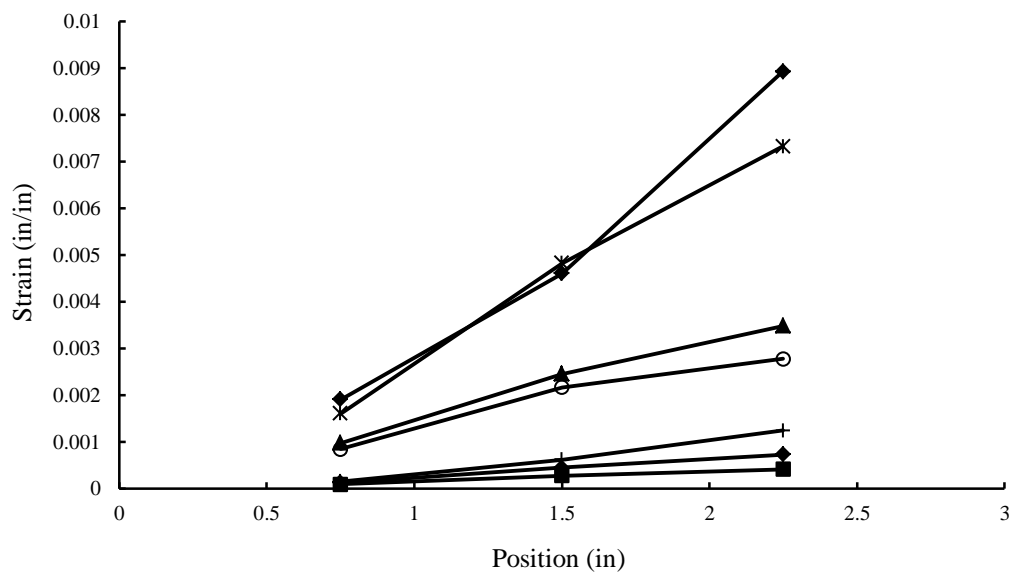


**Figure B.7** Strain-position curve for control column C4 in the X direction.

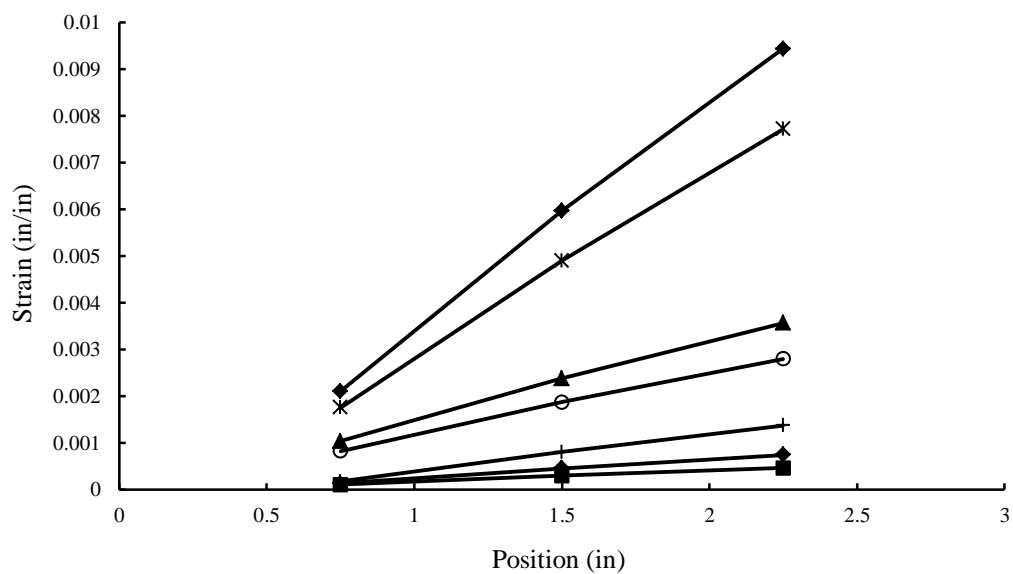


**Figure B.8** Strain-position curve for control column C4 in the Y direction.

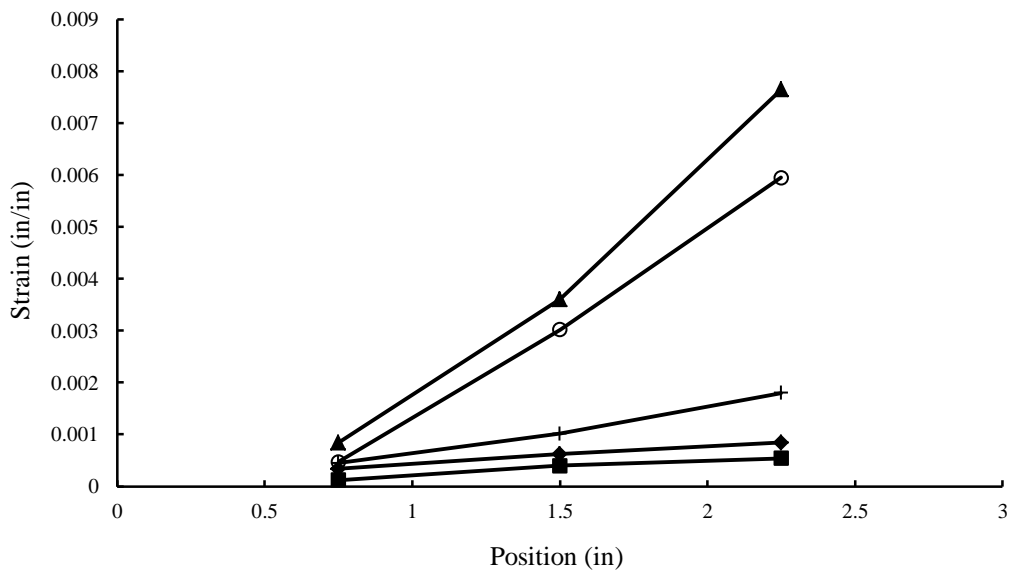


**Figure B.9** Strain-position curve for control column C5 in the X direction.

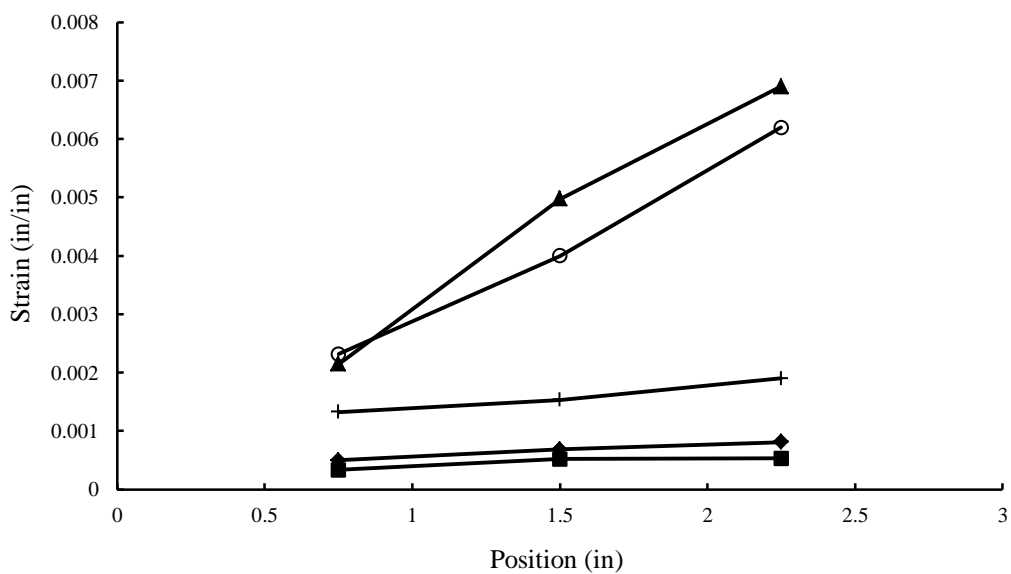


**Figure B.10** Strain-position curve for control column C5 in the Y direction.

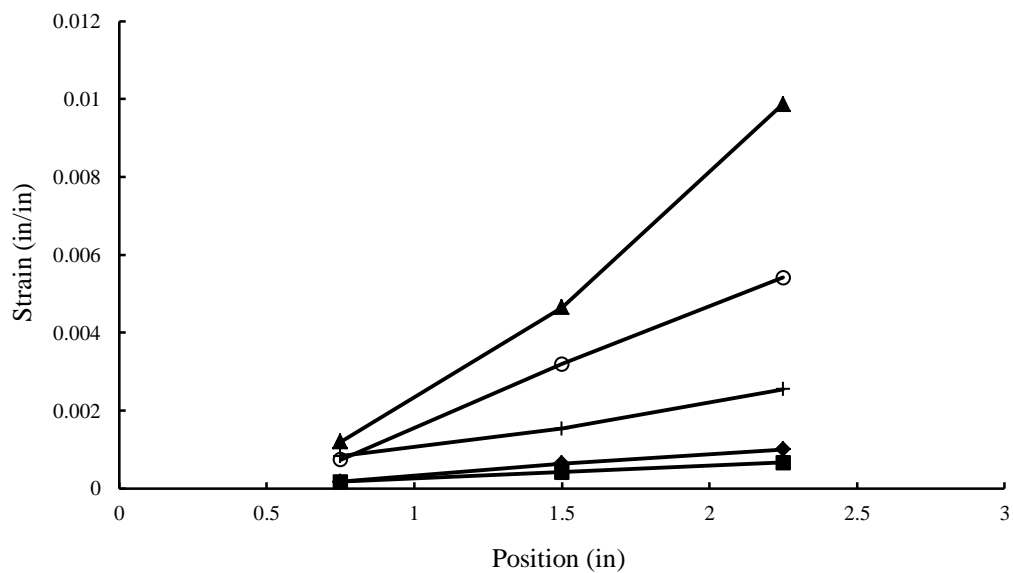


**Figure B.11** Strain-position curve for control column C6 in the X direction.

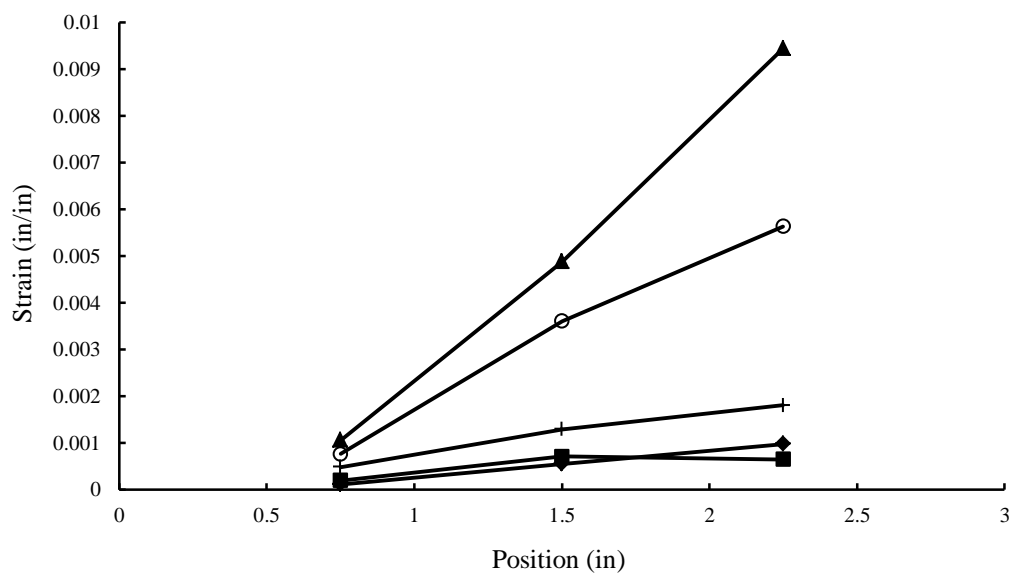


**Figure B.12** Strain-position curve for control column C6 in the Y direction.

## **APPENDIX C**

### **LOAD-DEFLECTION CURVES OF COLUMN SPECIMENS**

In Appendix C, **Figures C.1-C.12** present the experimental load-deflection curves of the concrete column specimens.

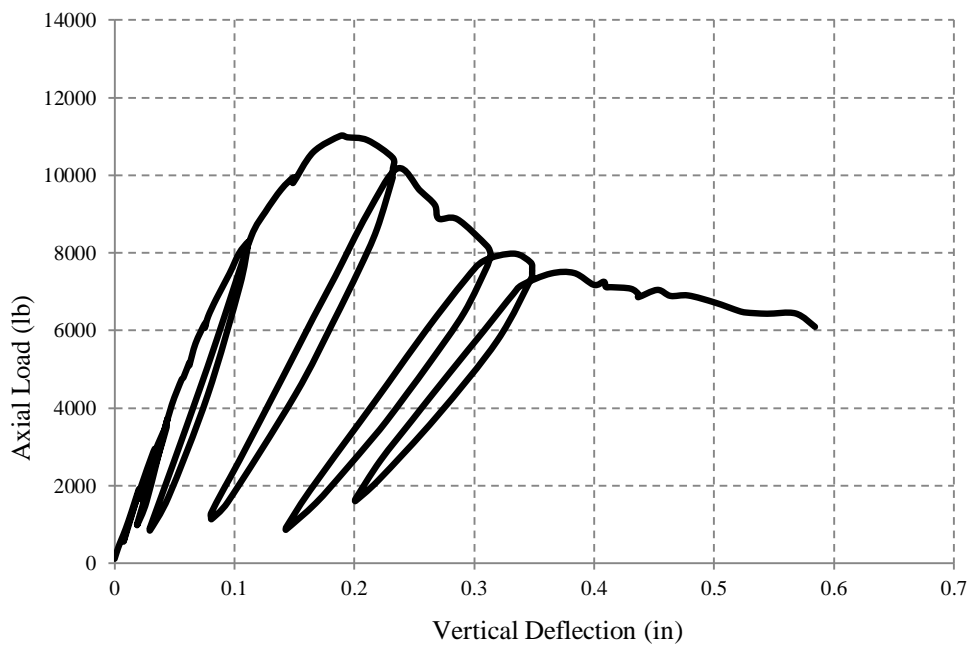


**Figure C.1** Experimental load-vertical deflection for column C1.

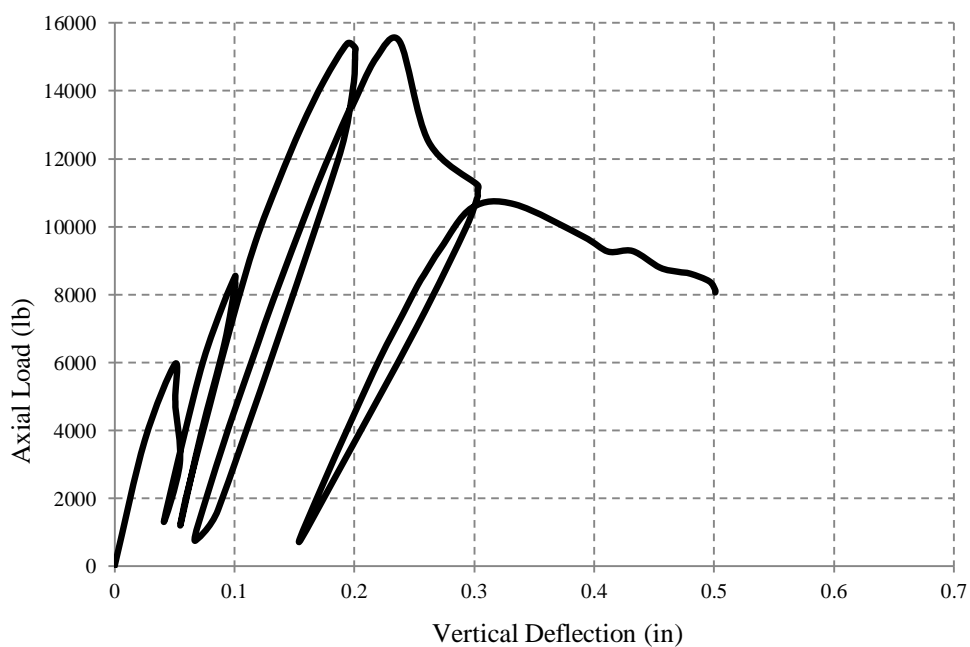


**Figure C.2** Experimental load-vertical deflection for column C2.

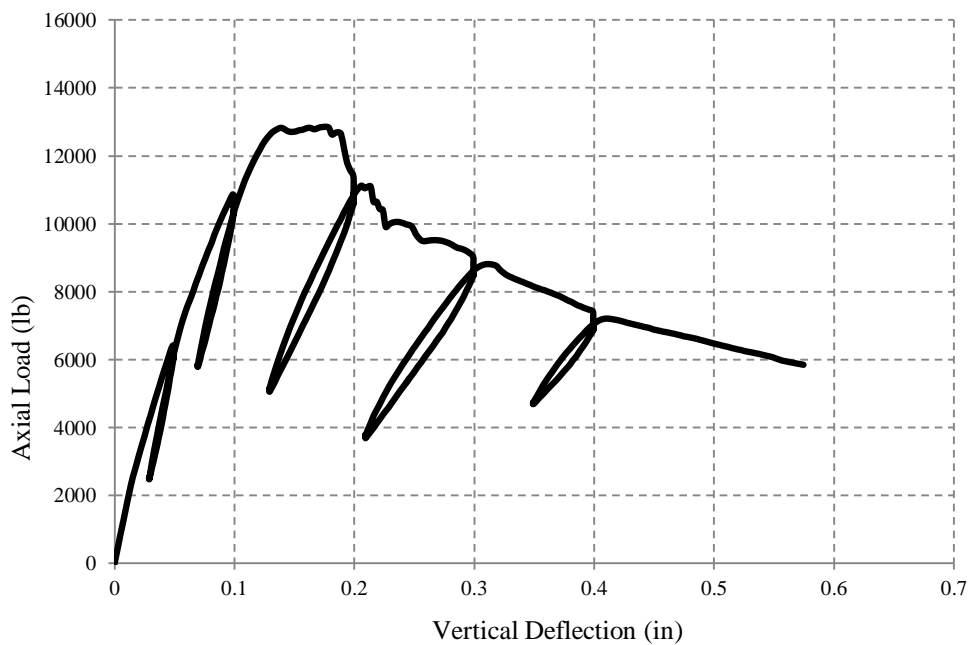


**Figure C.3** Experimental load-vertical deflection for column C3.

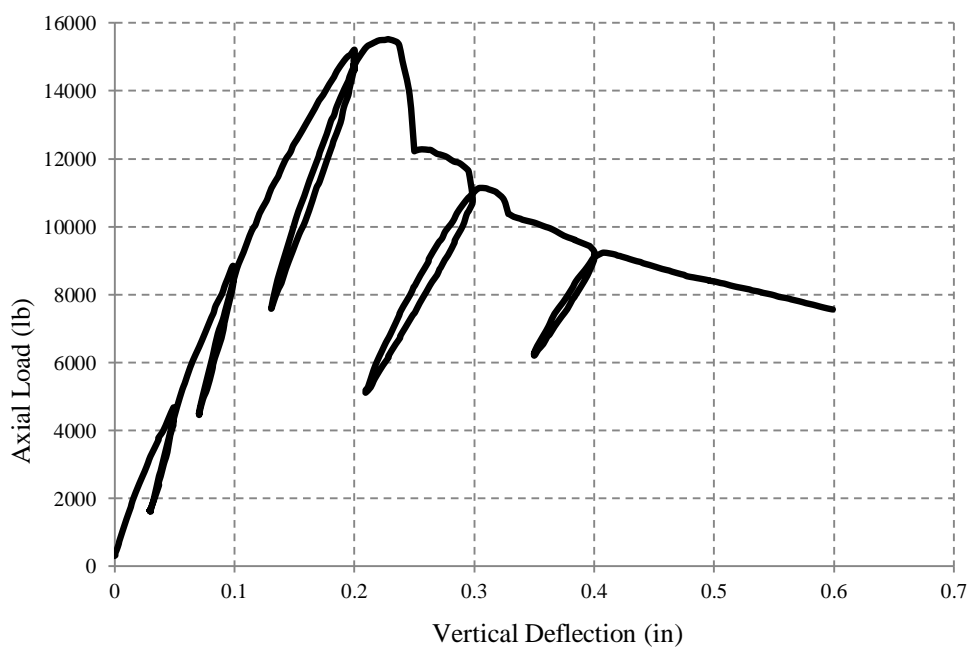


**Figure C.4** Experimental load-vertical deflection for column C4.



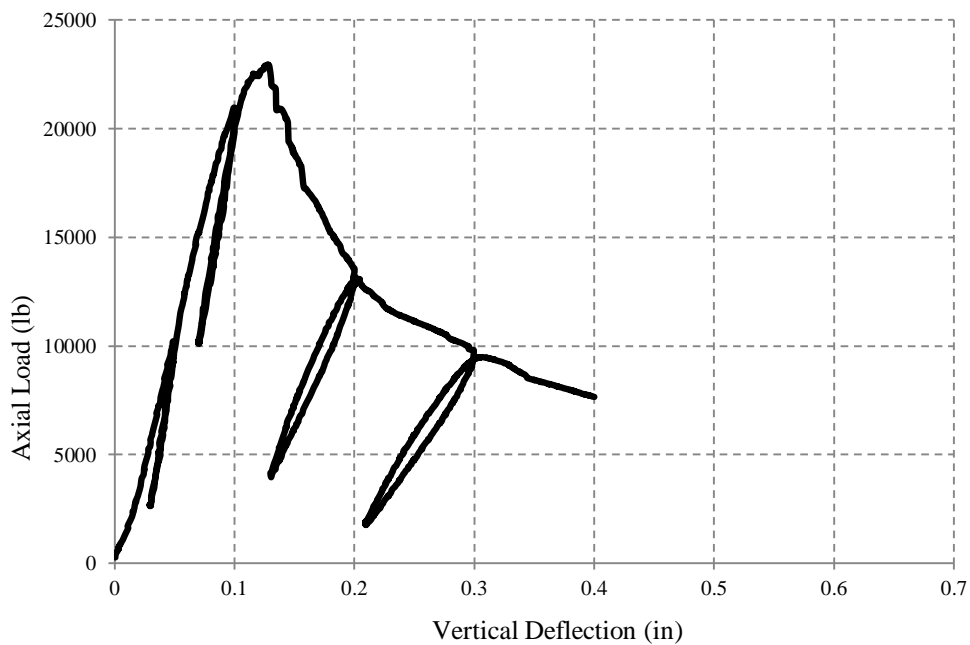


**Figure C.5** Experimental load-vertical deflection for column C5.

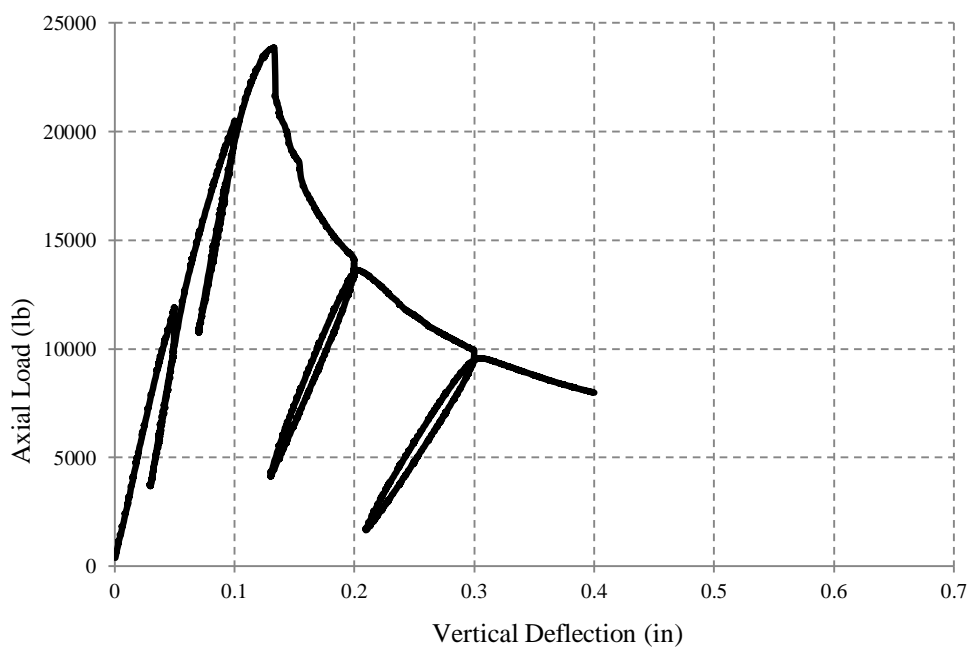


**Figure C.6** Experimental load-vertical deflection for column C6.

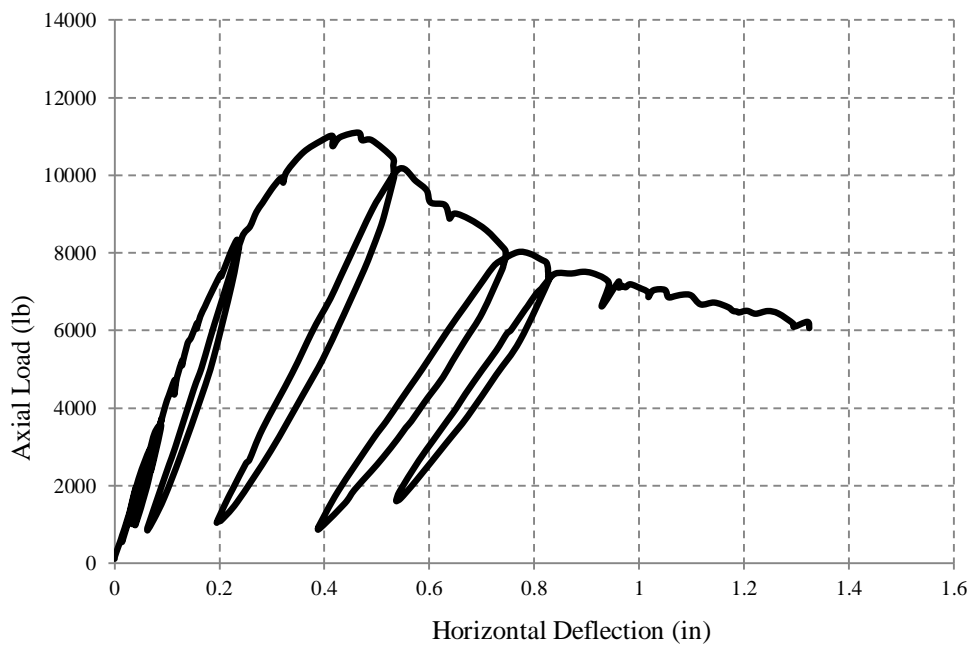


**Figure C.7** Experimental load-deflection in the X direction for column C1.

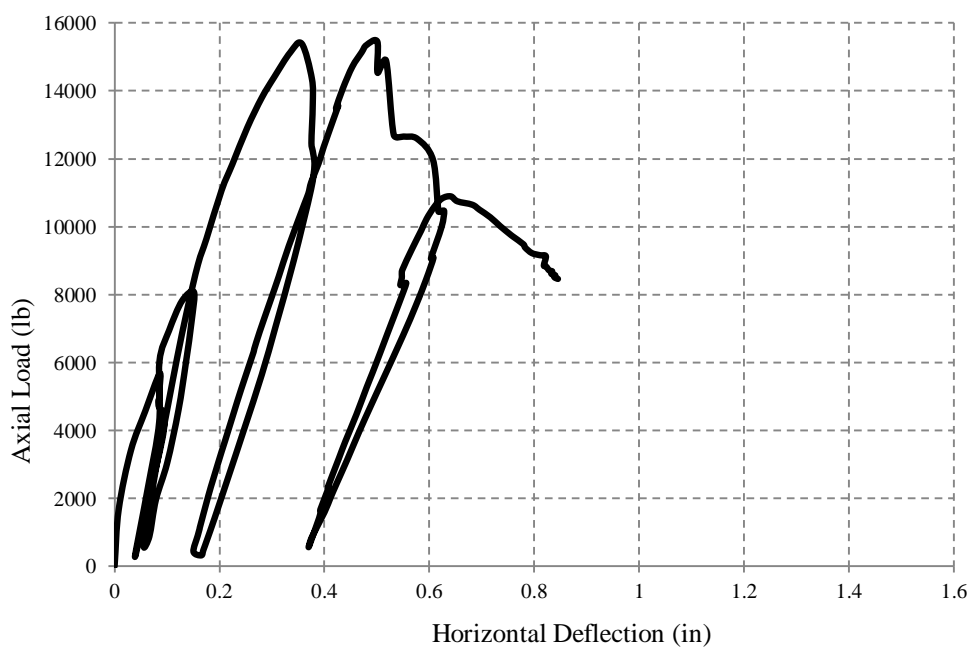


**Figure C.8** Experimental load-deflection in the X direction for column C2.

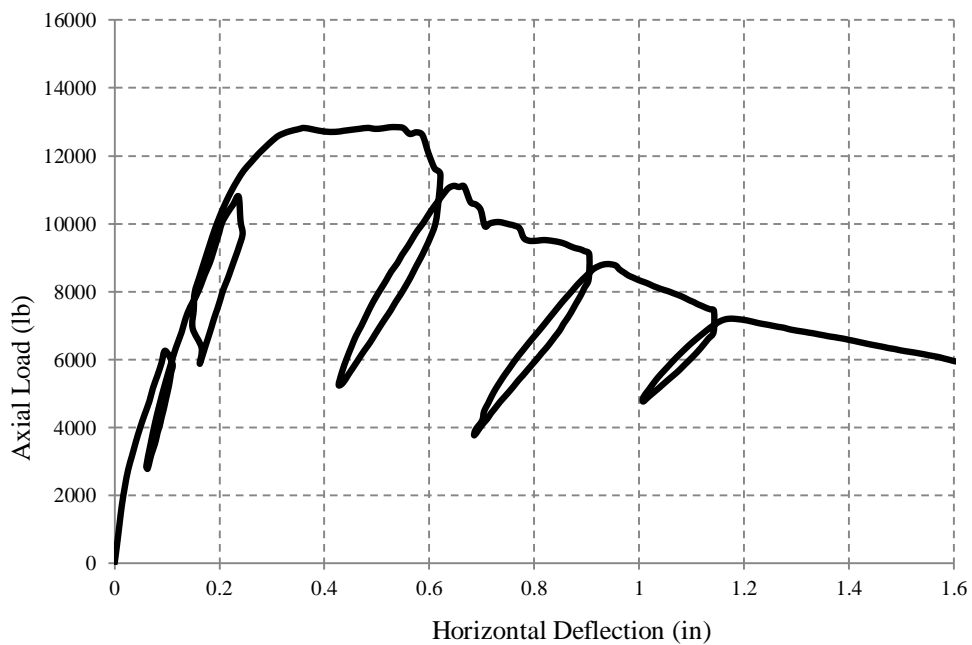


**Figure C.9** Experimental load-deflection in the X direction for column C3.

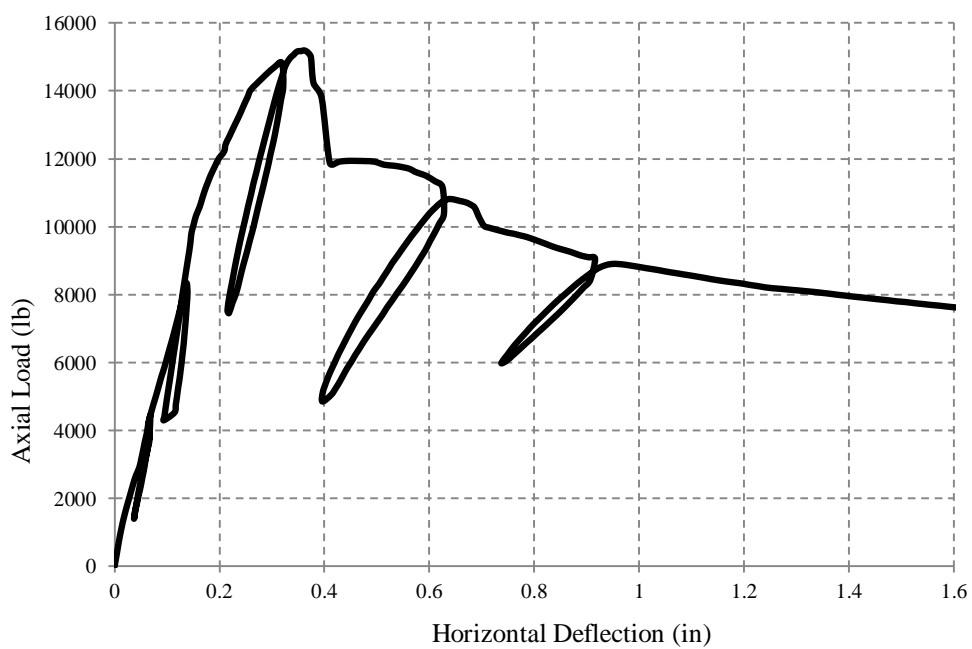


**Figure C.10** Experimental load-deflection in the X direction for column C4.

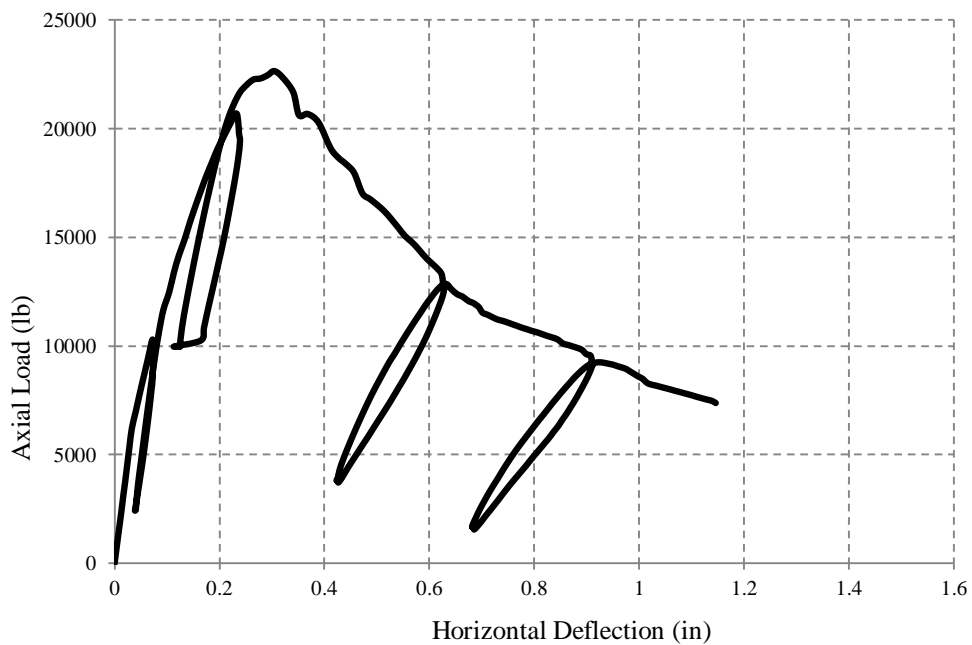


**Figure C.11** Experimental load-deflection in the X direction for column C5.

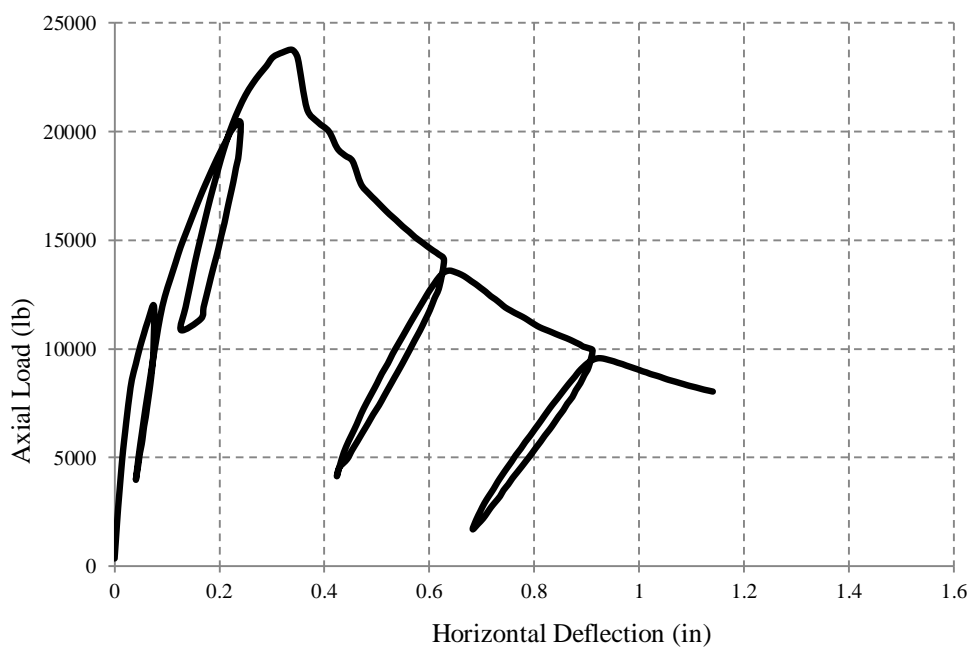


**Figure C.12** Experimental load-deflection in the X direction for column C6.

## **APPENDIX D**

### **ANALYTICAL LOAD-DEFLECTION AND MOMENT-CURVATURE CURVES**

In Appendix D, **Figures D.1-D.18** present the analytical load-deflection and moment-curvature curves of the concrete column specimens. **Figures D.19-D.33** compare the experimental results to the results computed from the proposed computer program.

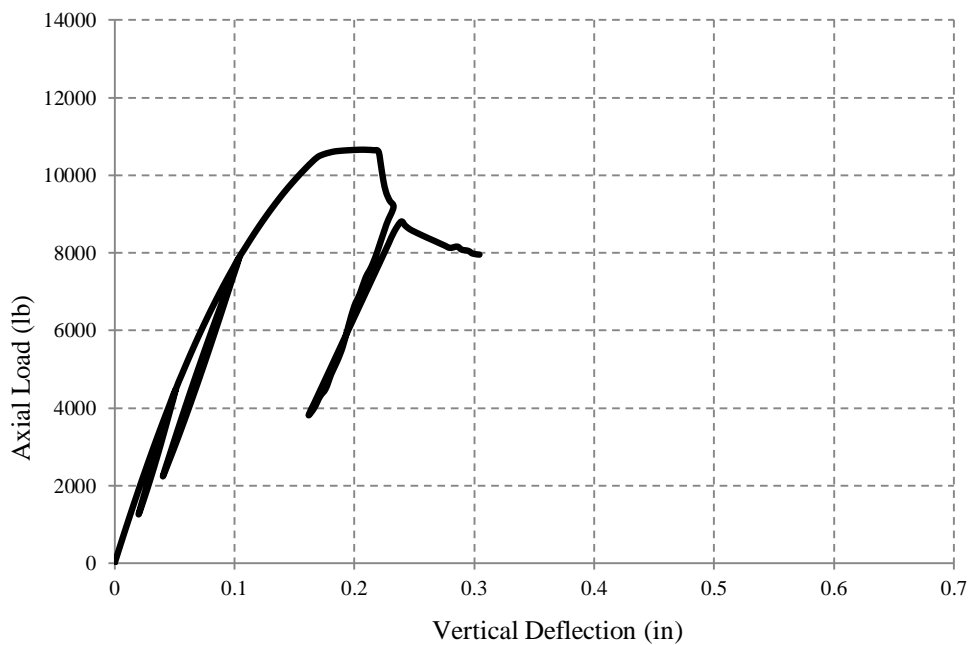


**Figure D.1** Analytical load-vertical deflection for column C1.

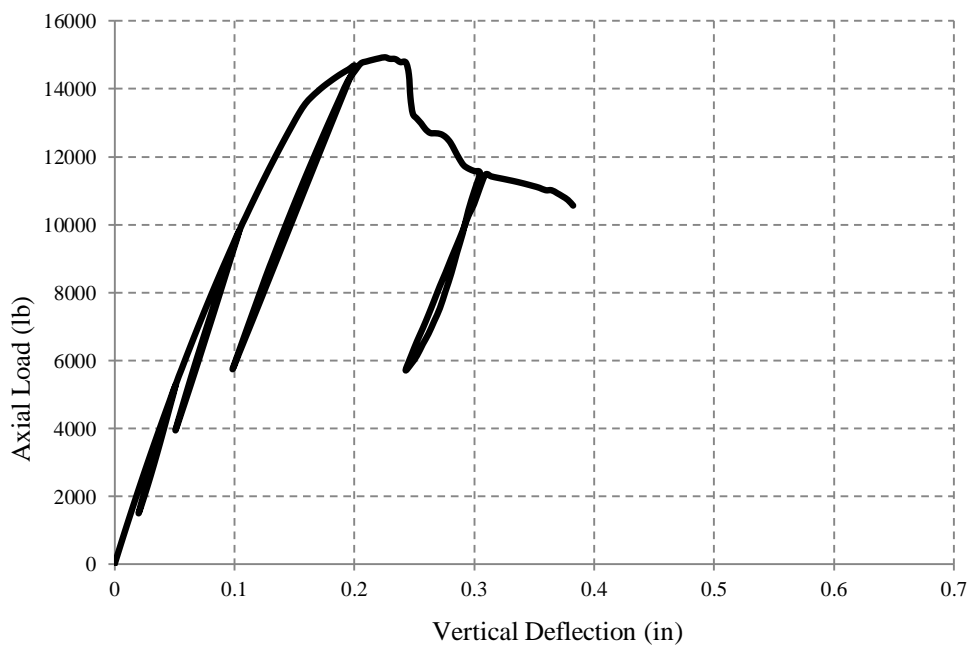


**Figure D.2** Analytical load-vertical deflection for column C2.

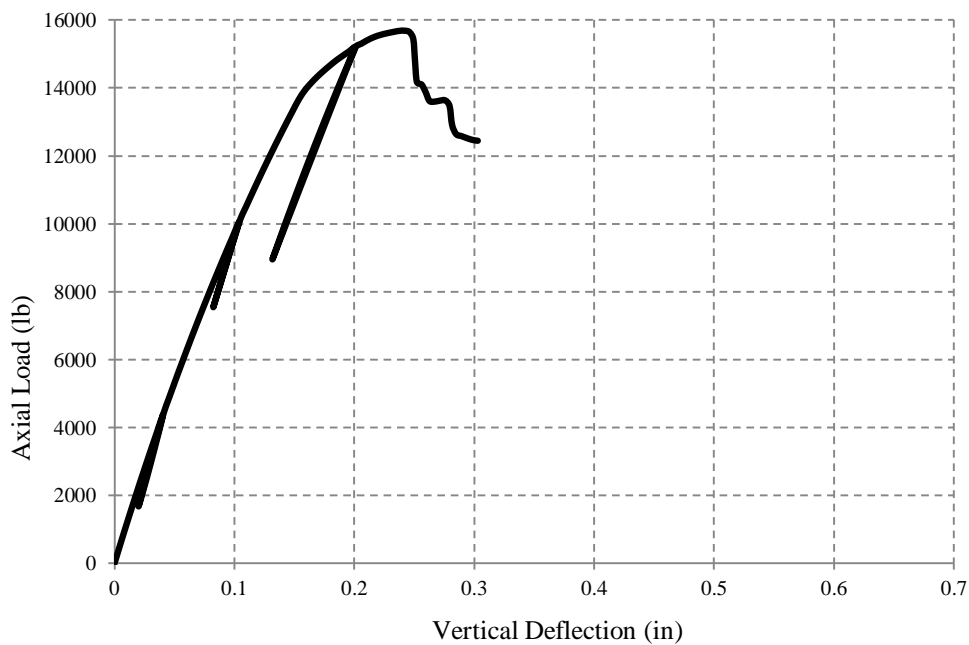


**Figure D.3** Analytical load-vertical deflection for column C3.

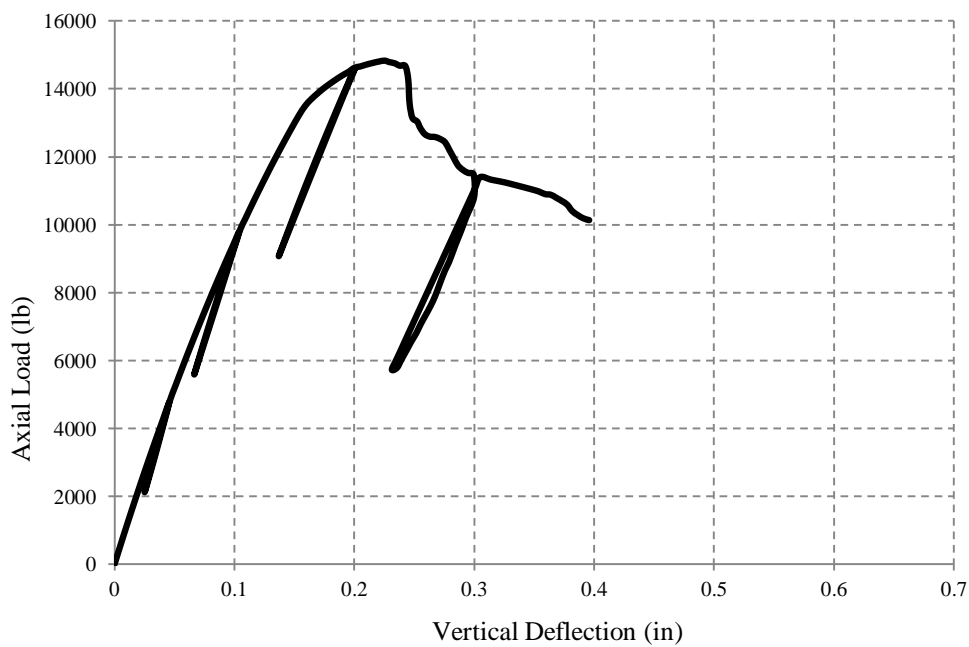


**Figure D.4** Analytical load-vertical deflection for column C4.

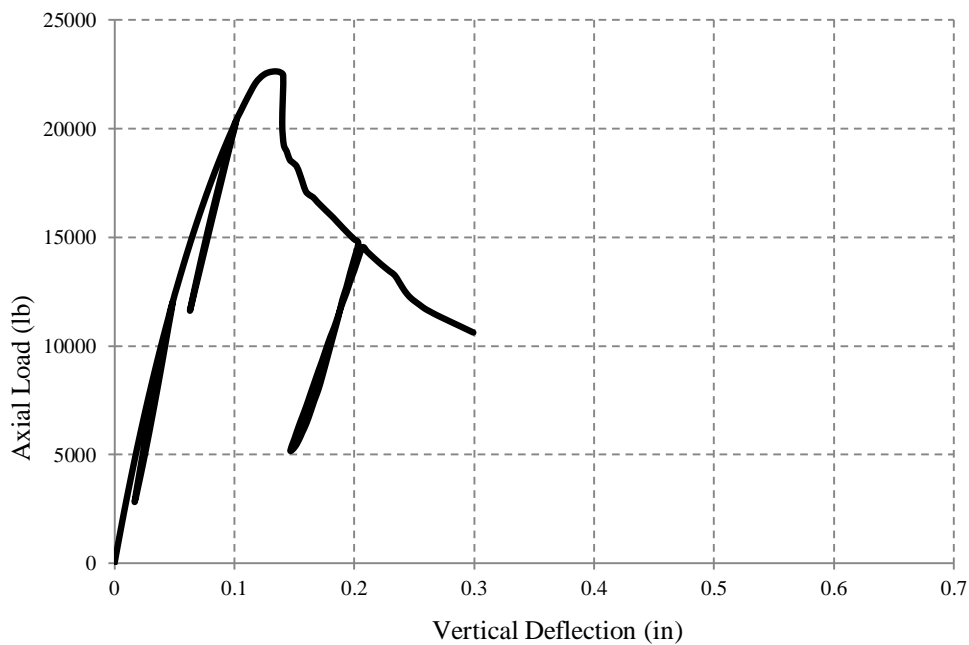


**Figure D.5** Analytical load-vertical deflection for column C5.

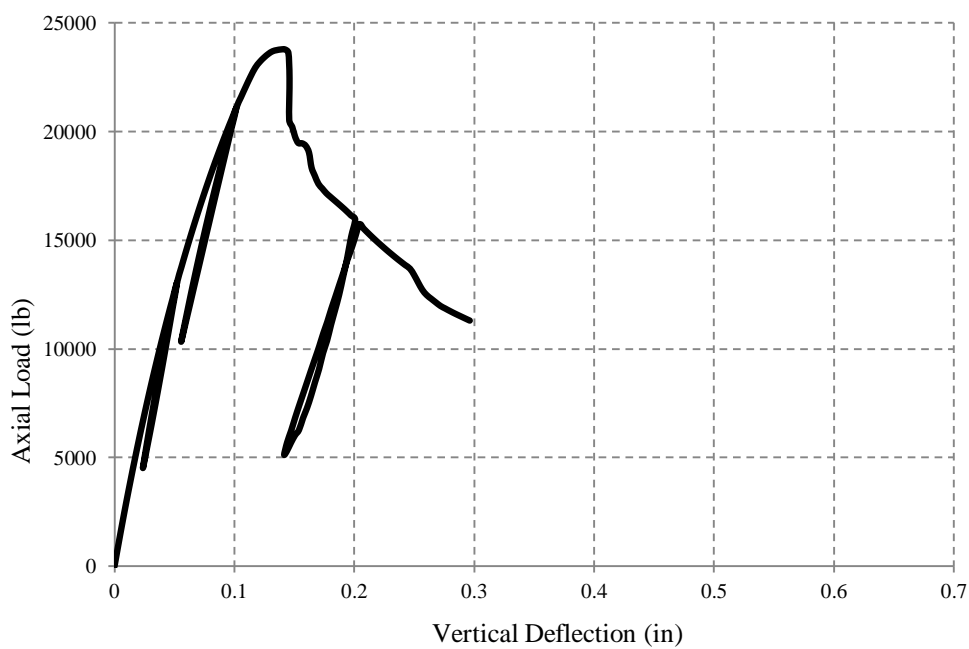


**Figure D.6** Analytical load-vertical deflection for column C6.



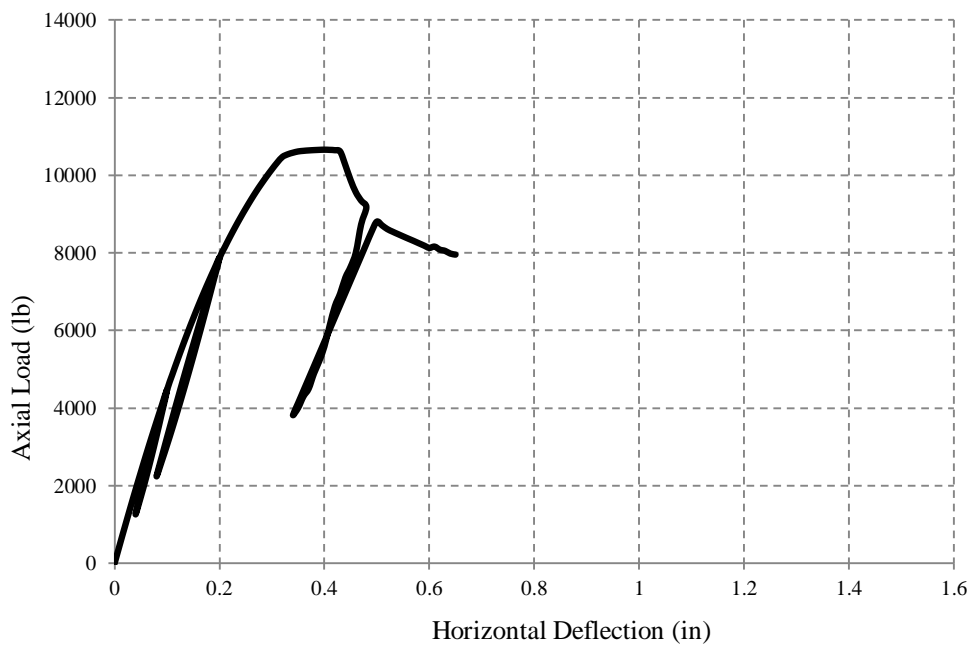


**Figure D.7** Analytical load-deflection in the X direction for column C1.

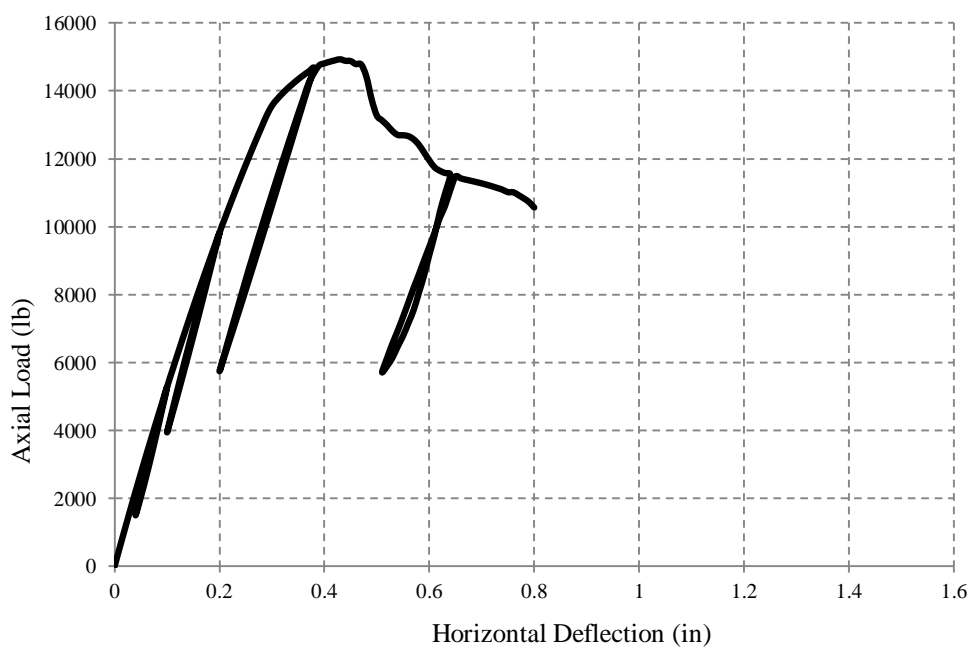


**Figure D.8** Analytical load-deflection in the X direction for column C2.

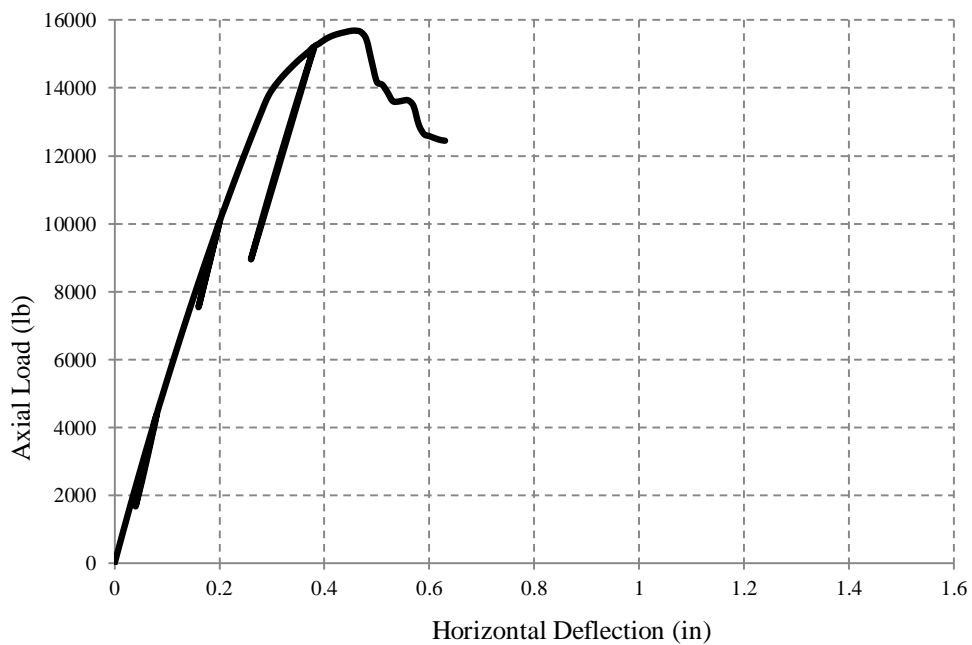


**Figure D.9** Analytical load-deflection in the X direction for column C3.

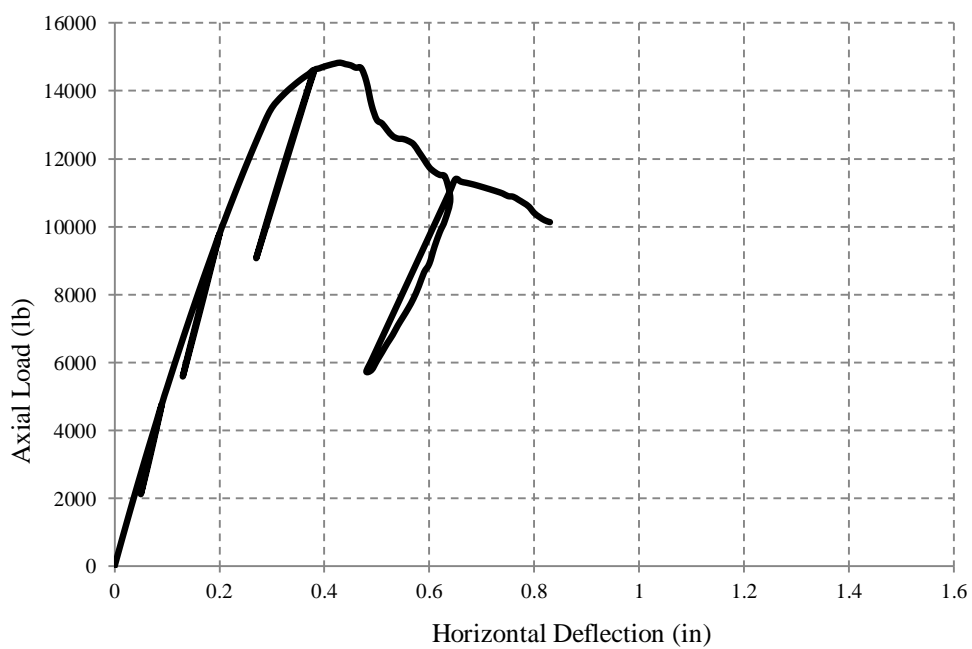


**Figure D.10** Analytical load-deflection in the X direction for column C4.

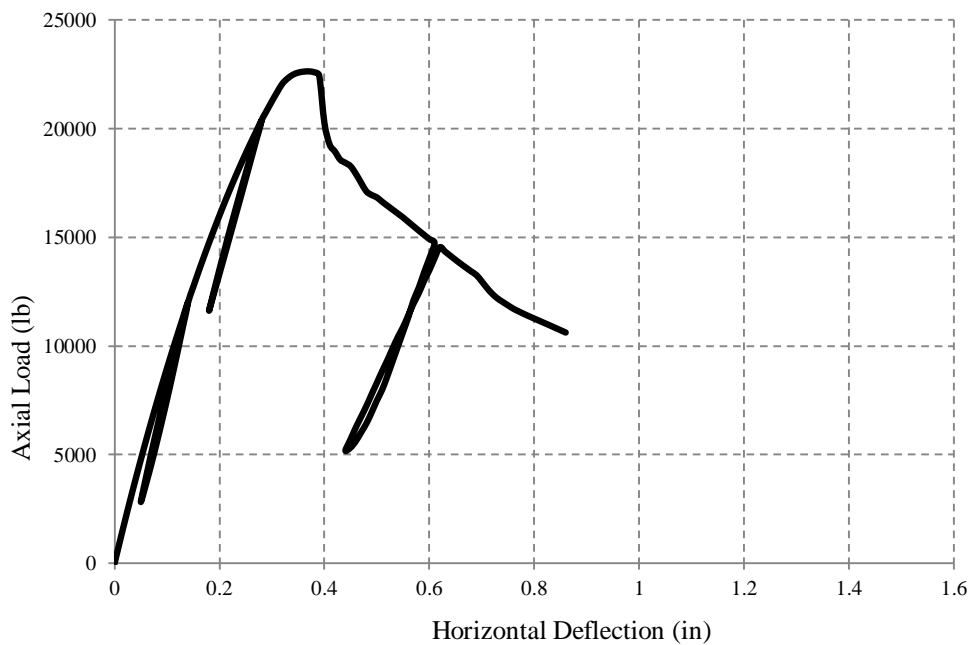


**Figure D.11** Analytical load-deflection in the X direction for column C5.

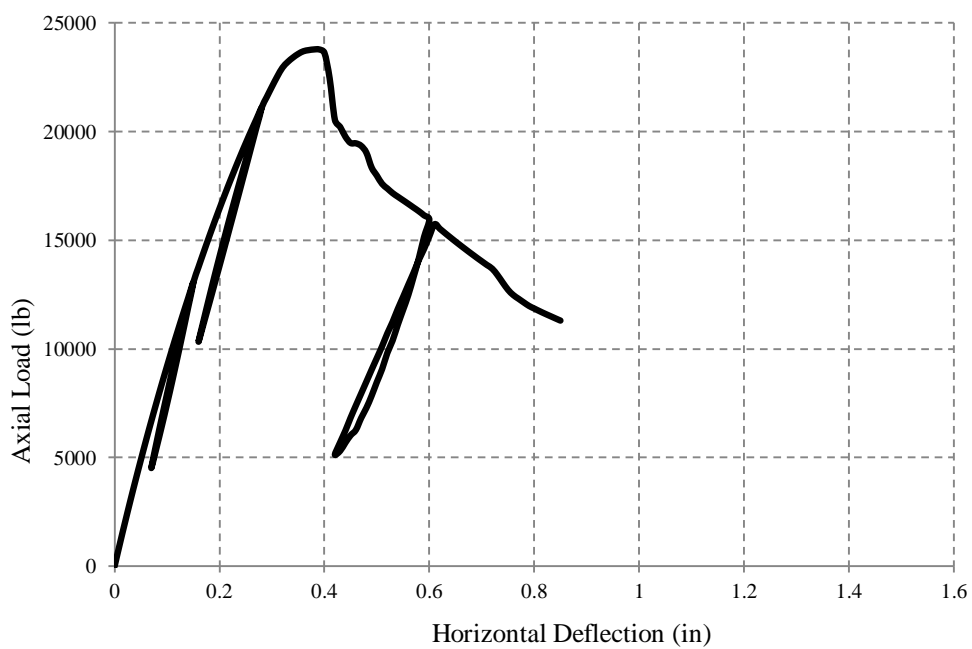


**Figure D.12** Analytical load-deflection in the X direction for column C6.

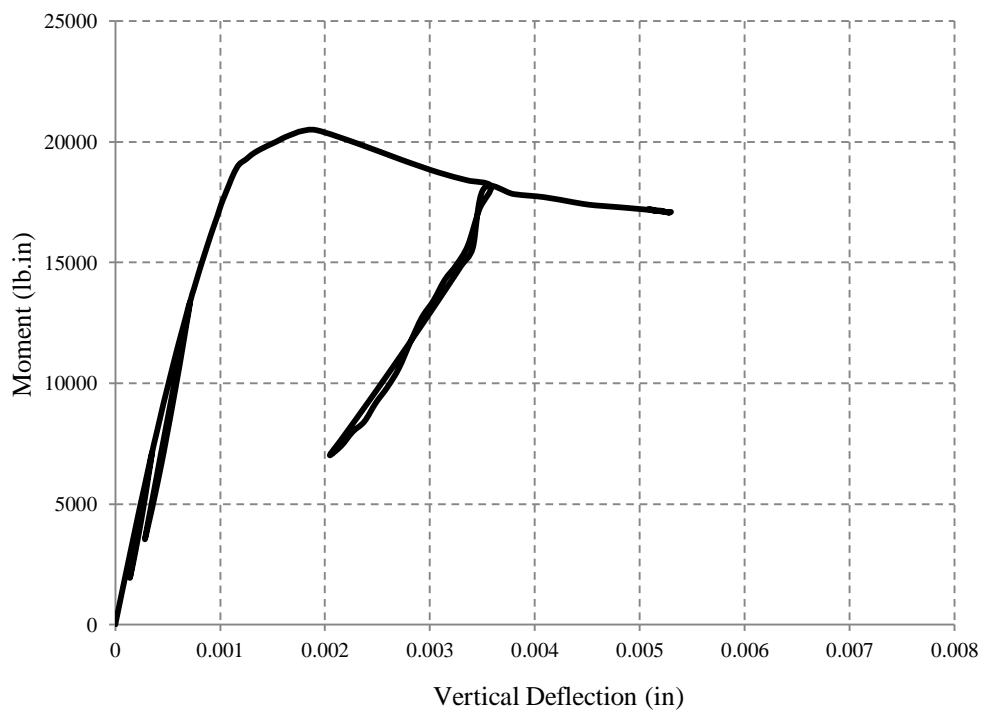


**Figure D.13** Analytical moment-curvature curve at X-direction for column C1.

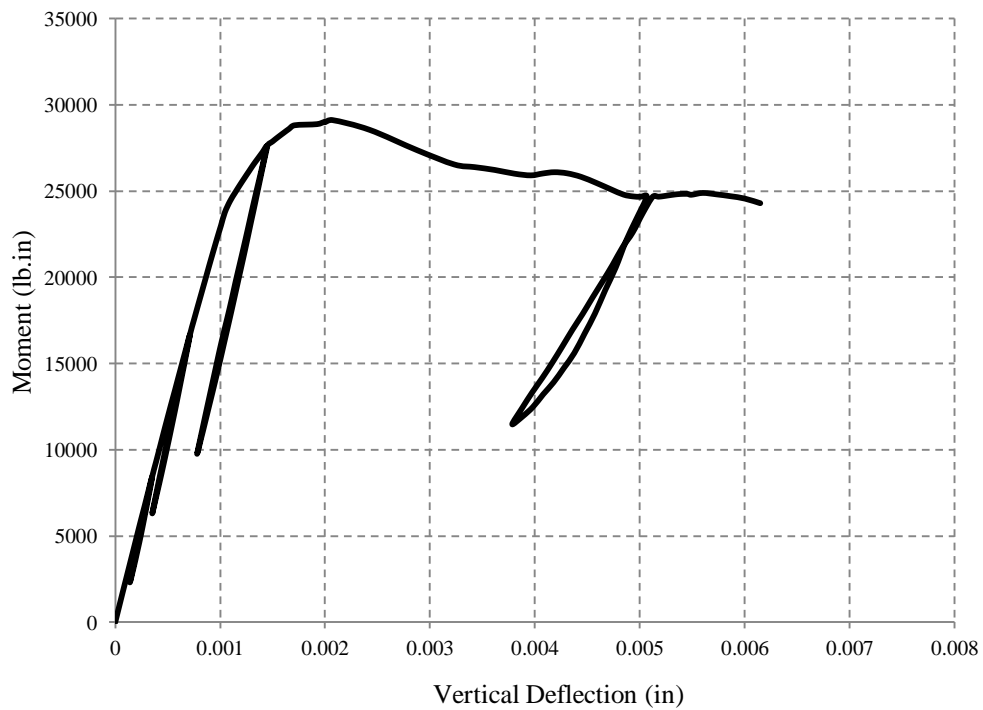


**Figure D.14** Analytical moment-curvature curve at X-direction for column C2.

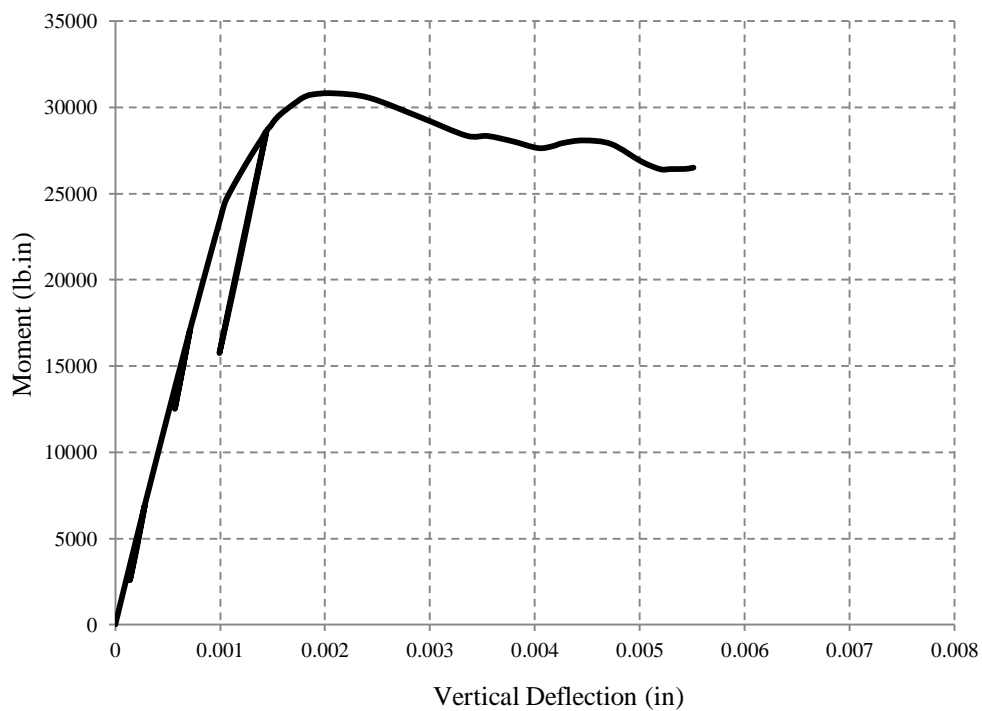


**Figure D.15** Analytical moment-curvature curve at X-direction for column C3.

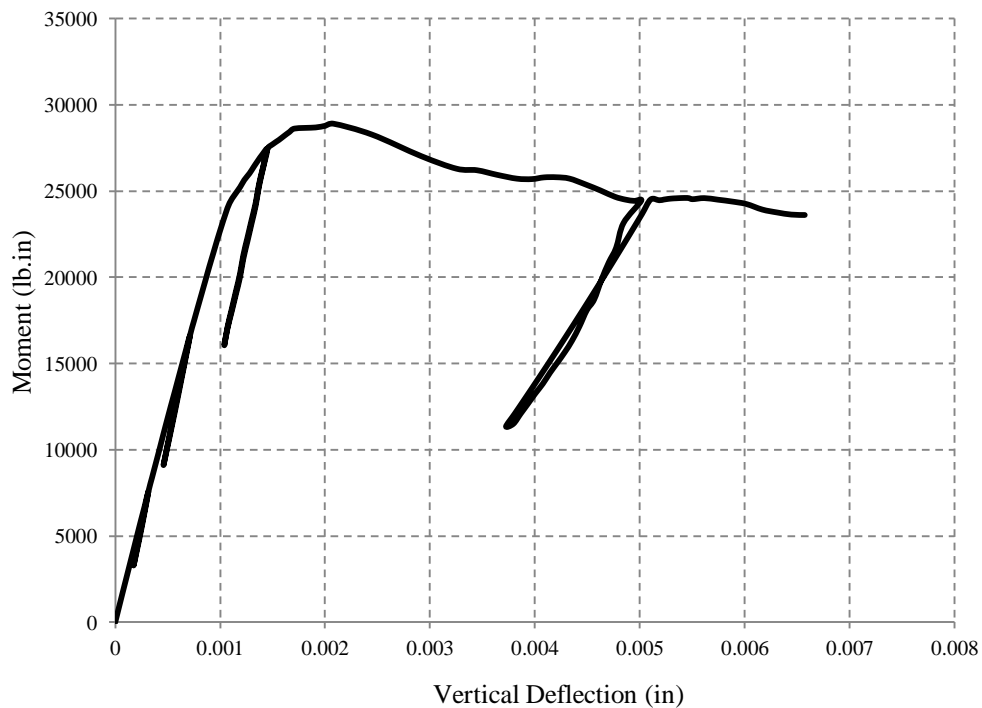


**Figure D.16** Analytical moment-curvature curve at X-direction for column C4.

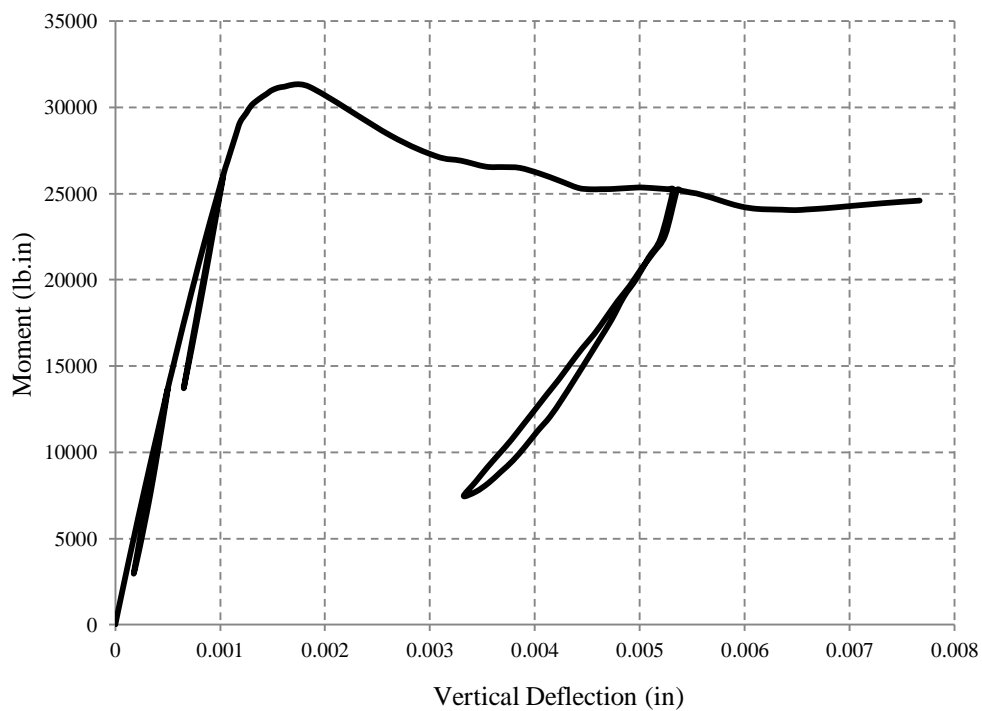


**Figure D.17** Analytical moment-curvature curve at X-direction for column C5.

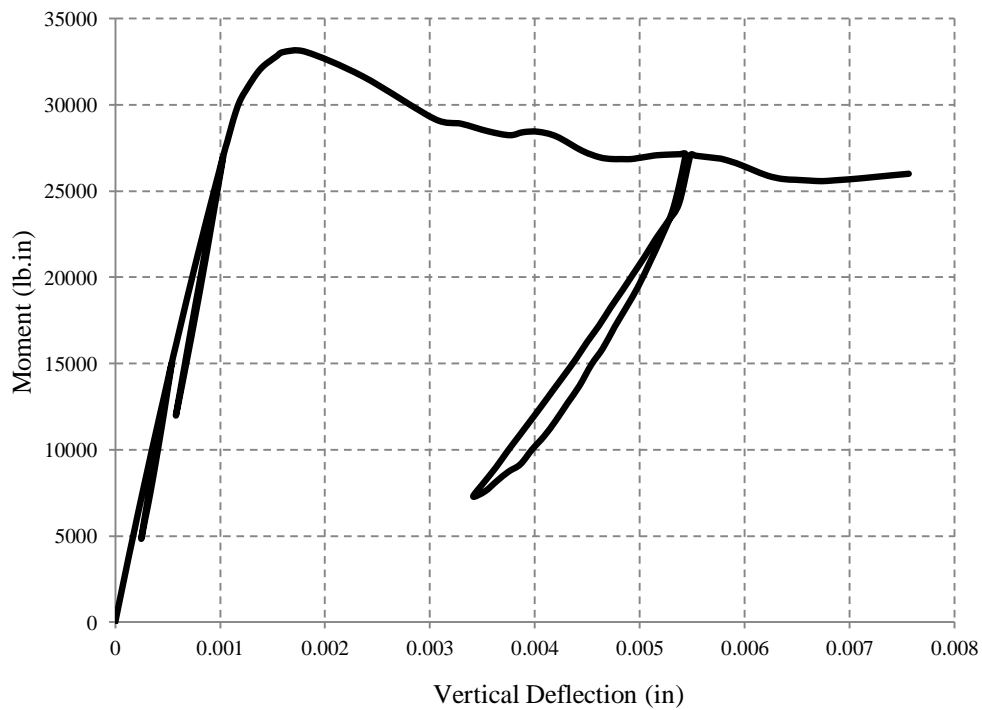


**Figure D.18** Analytical moment-curvature curve at X-direction for column C6.

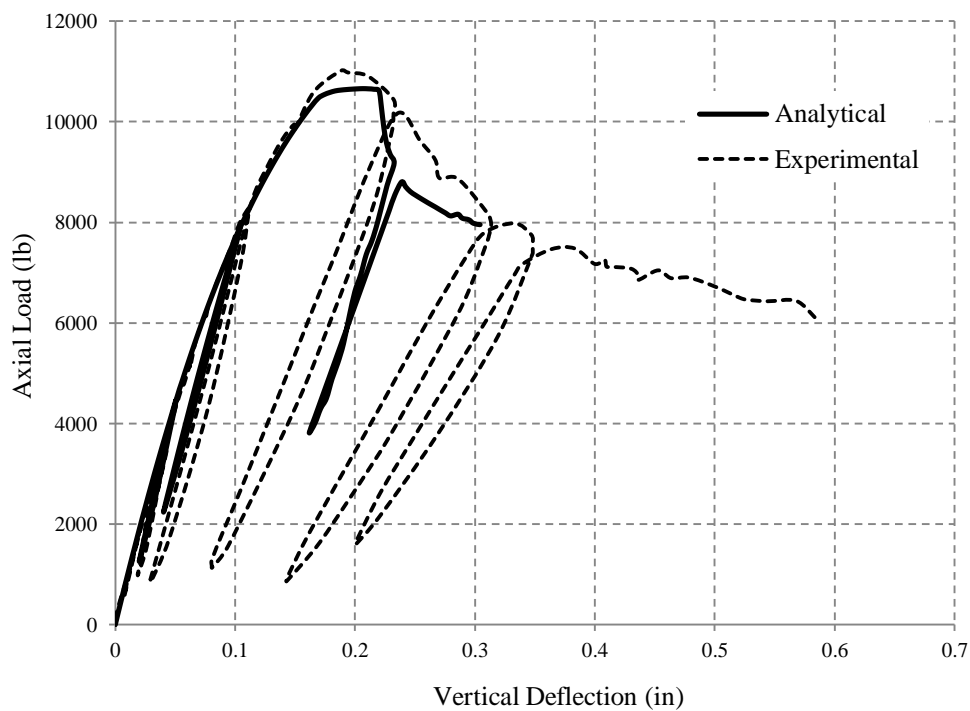


**Figure D.19** Load-vertical deflection for column C1.

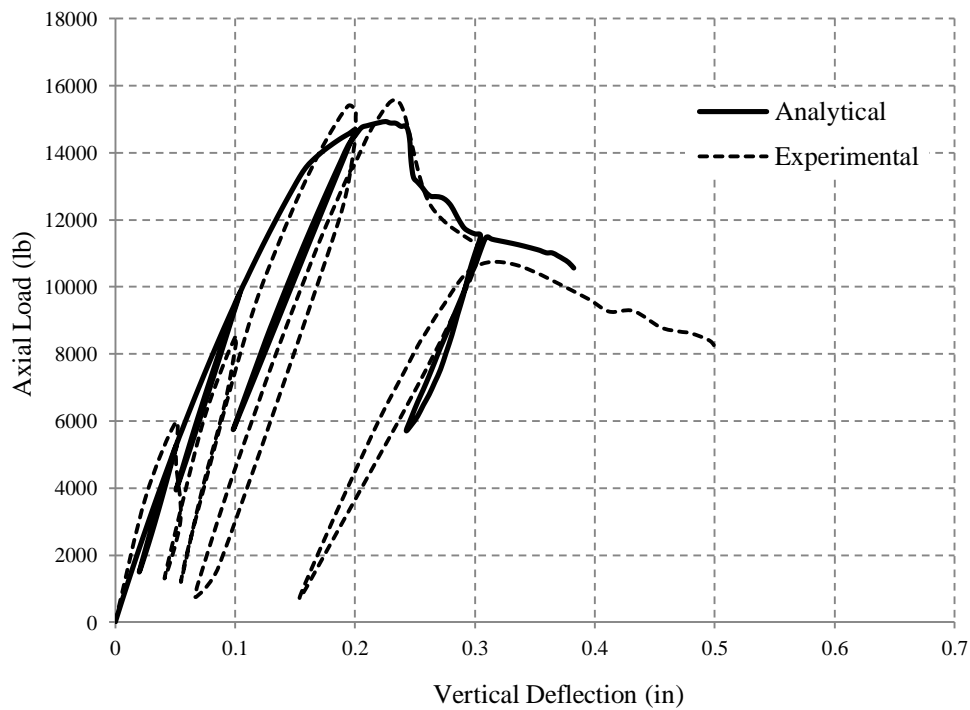


**Figure D.20** Load-vertical deflection for column C2.

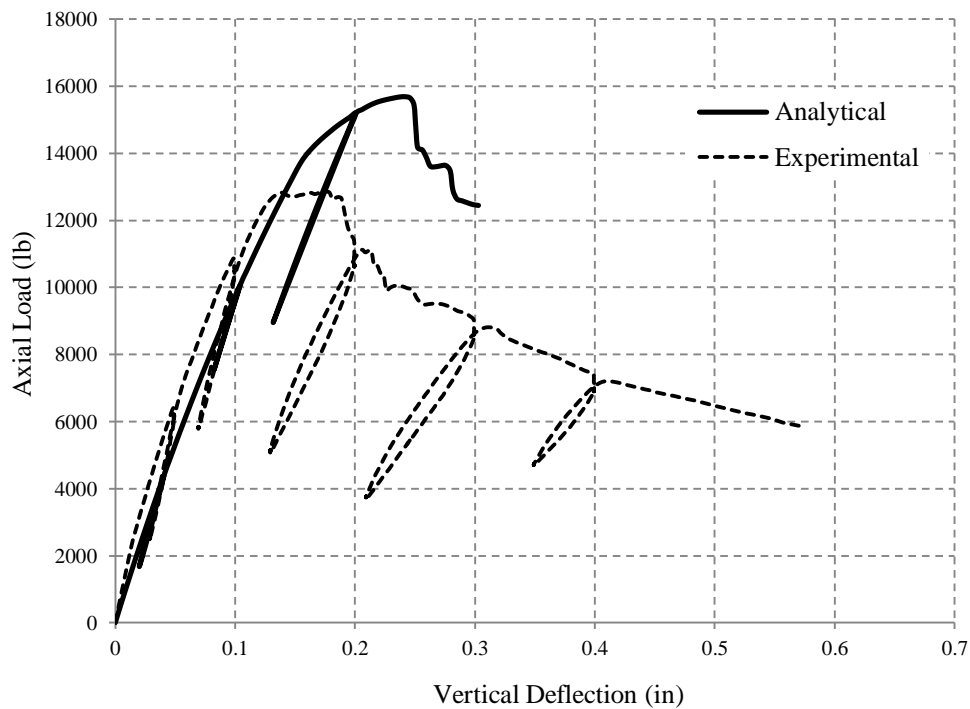


**Figure D.21** Load-vertical deflection for column C3.

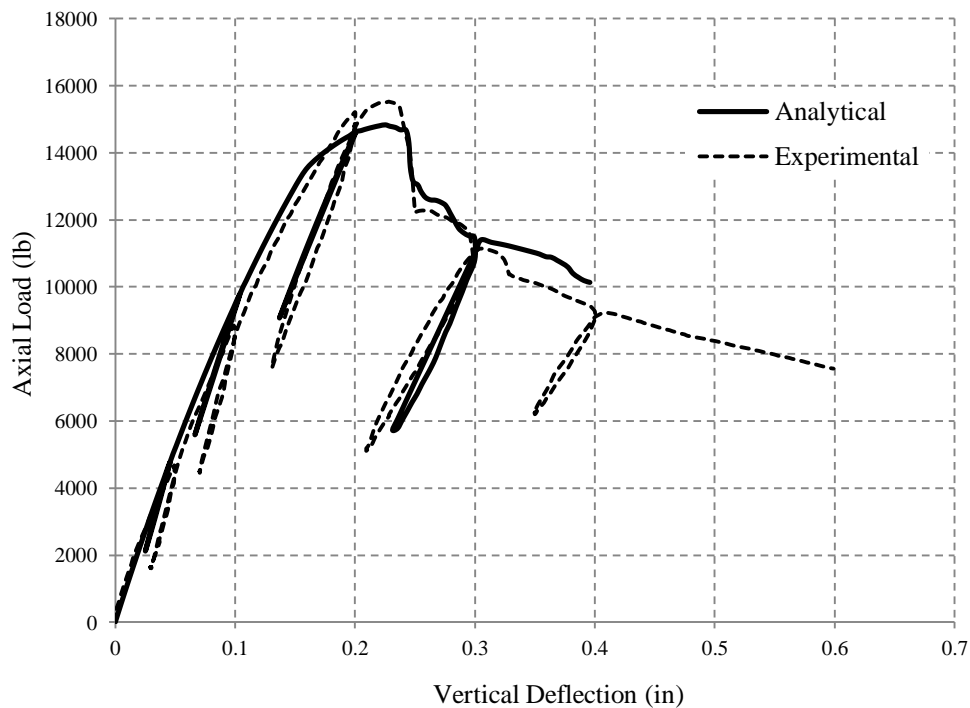


**Figure D.22** Load-vertical deflection for column C4.



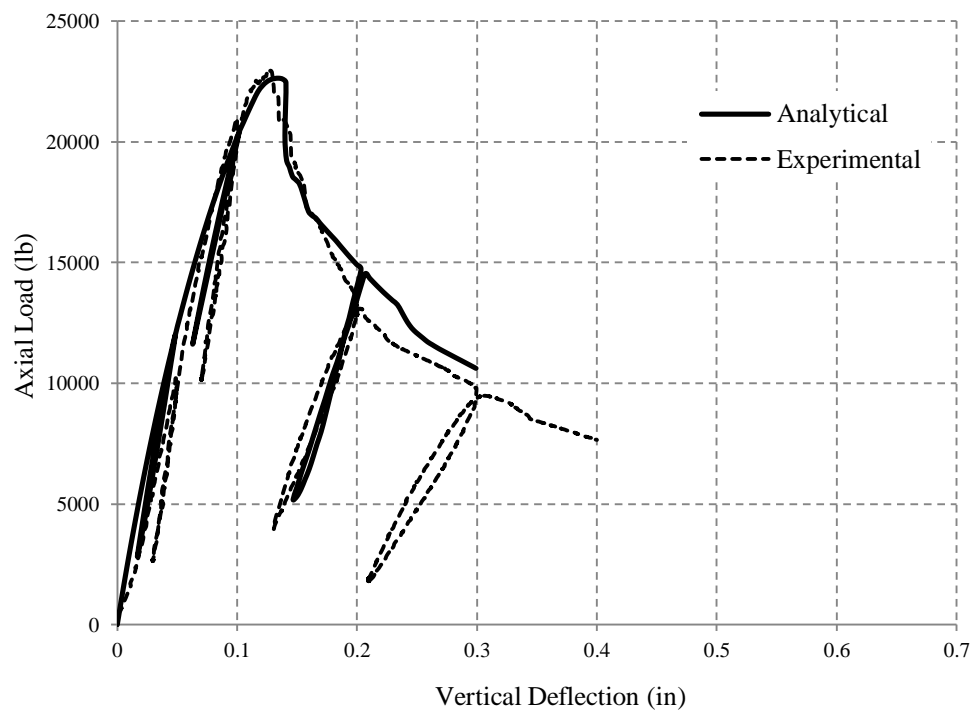


**Figure D.23** Load-vertical deflection for column C5.

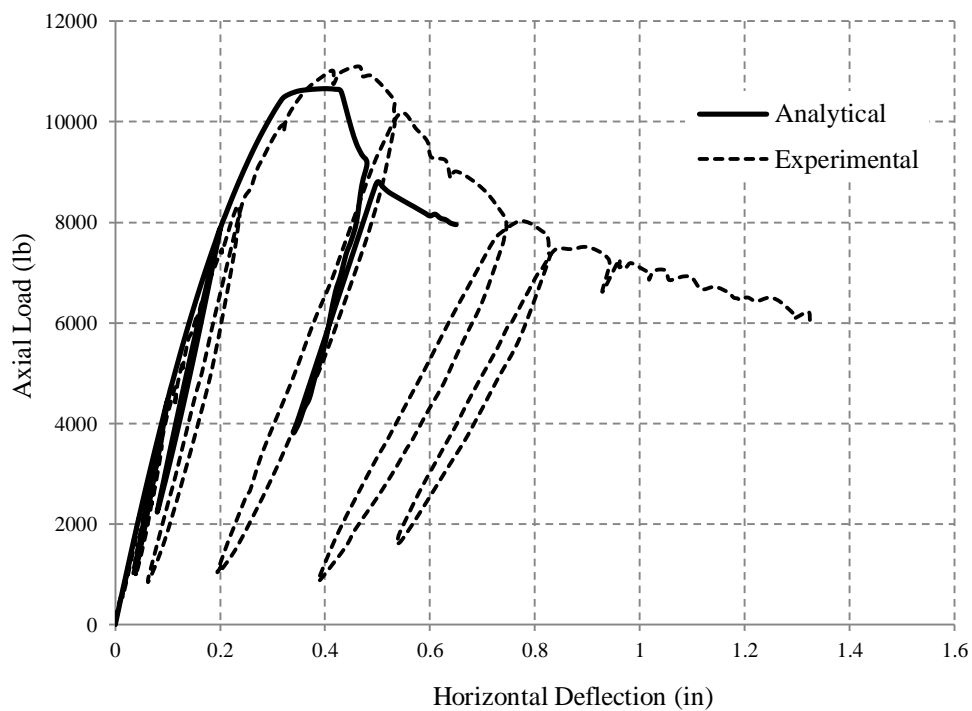


**Figure D.24** Load-deflection in the X direction for column C1.

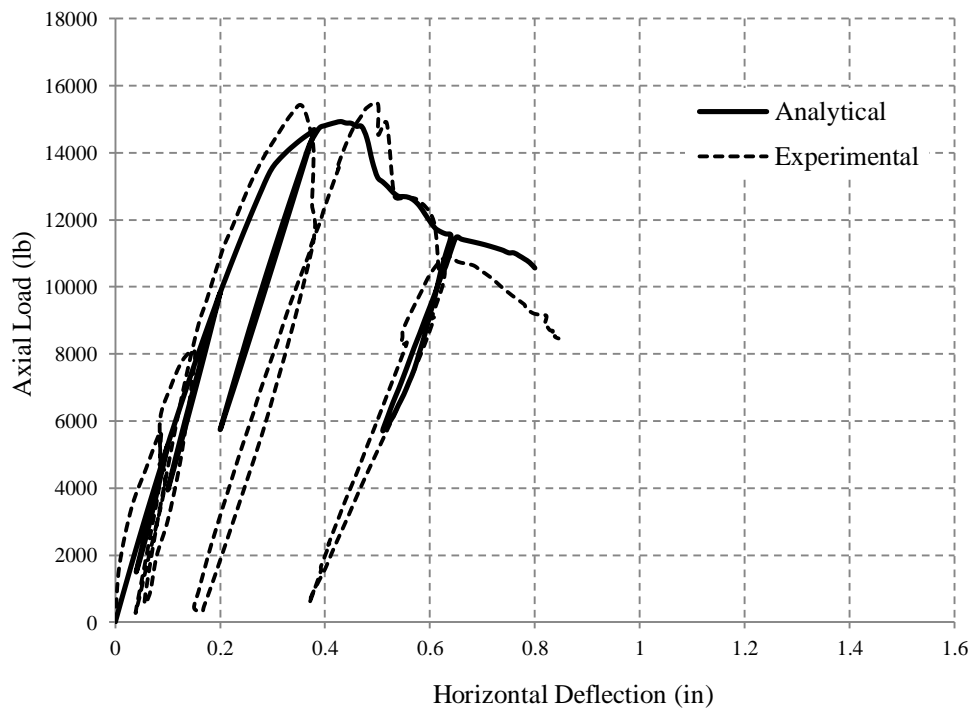


**Figure D.25** Load-deflection in the X direction for column C2.

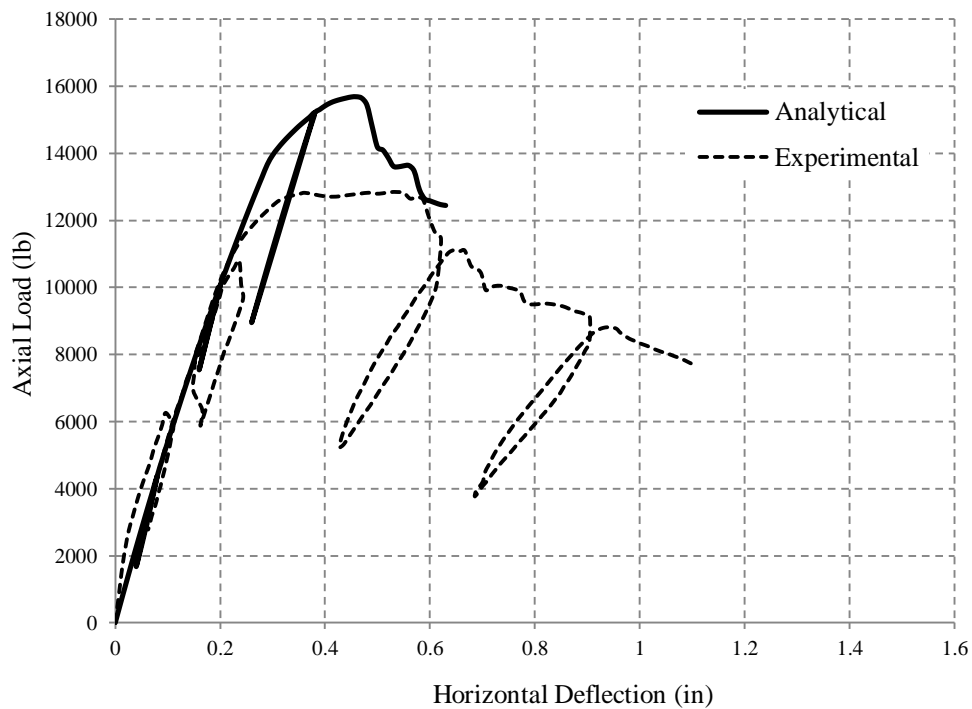


**Figure D.26** Load-deflection in the X direction for column C3.

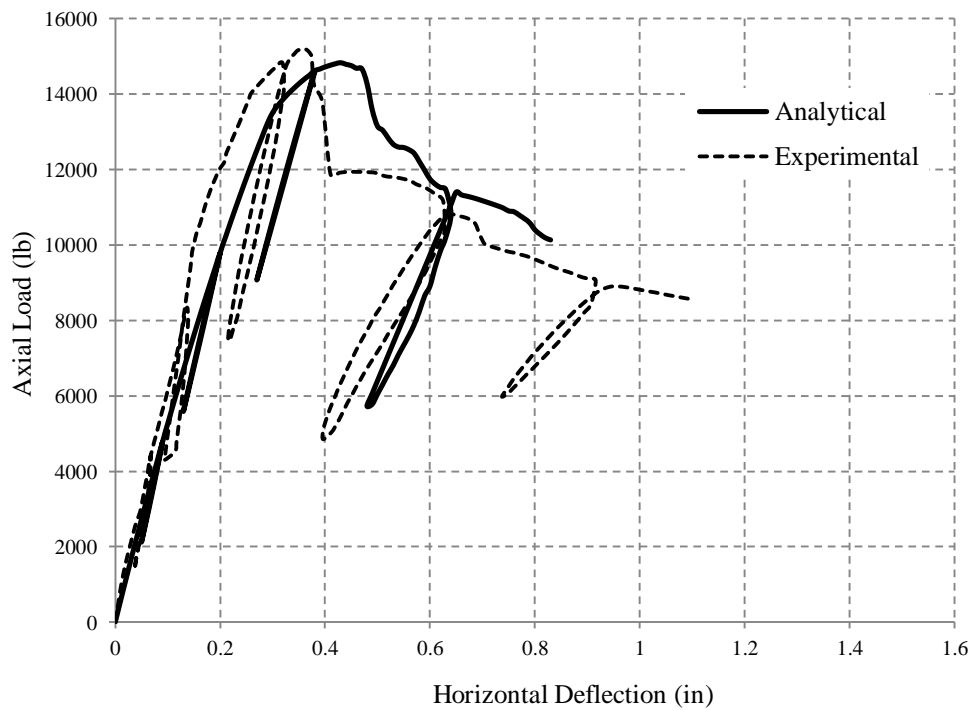


**Figure D.27** Load-deflection in the X direction for column C4.

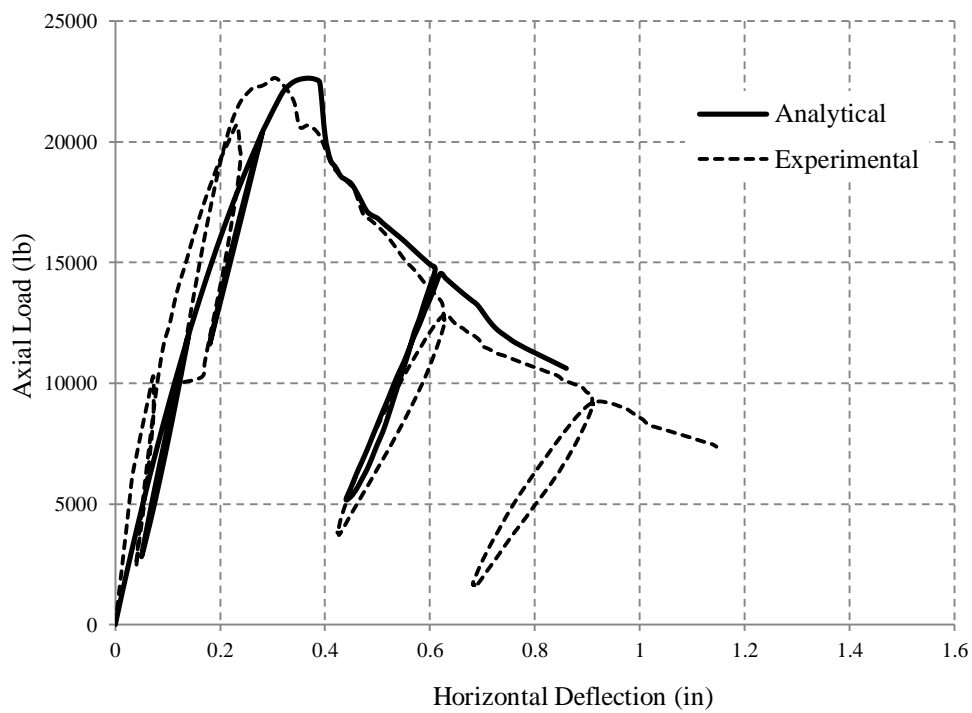


**Figure D.28** Load-deflection in the X direction for column C5.

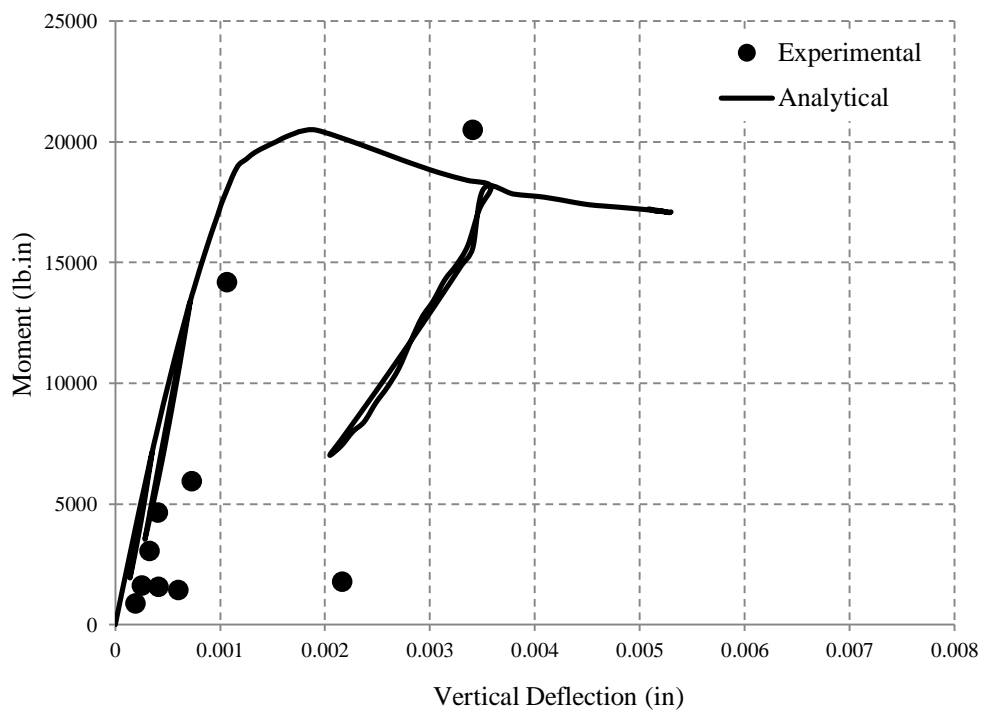


Figure D.29 Moment-curvature curve at X-direction for column C1.

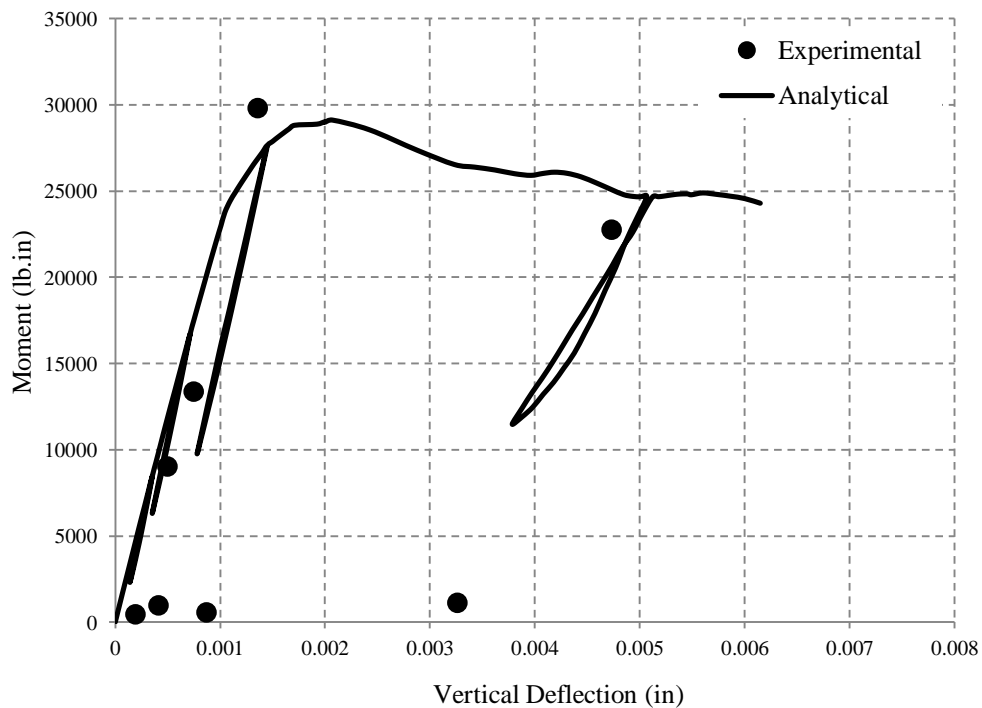
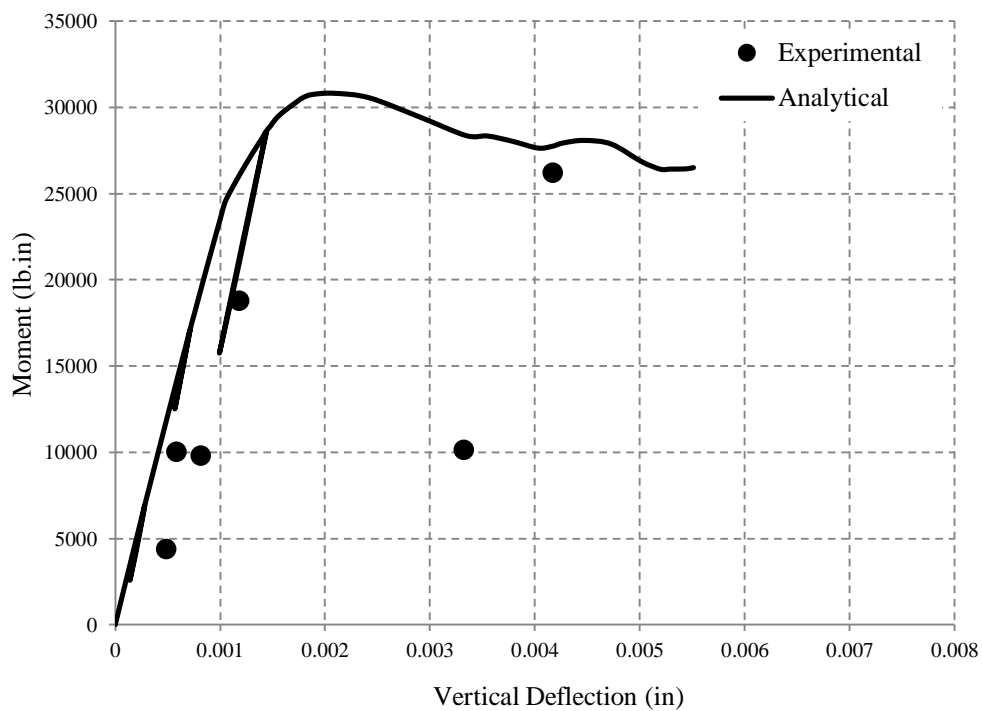
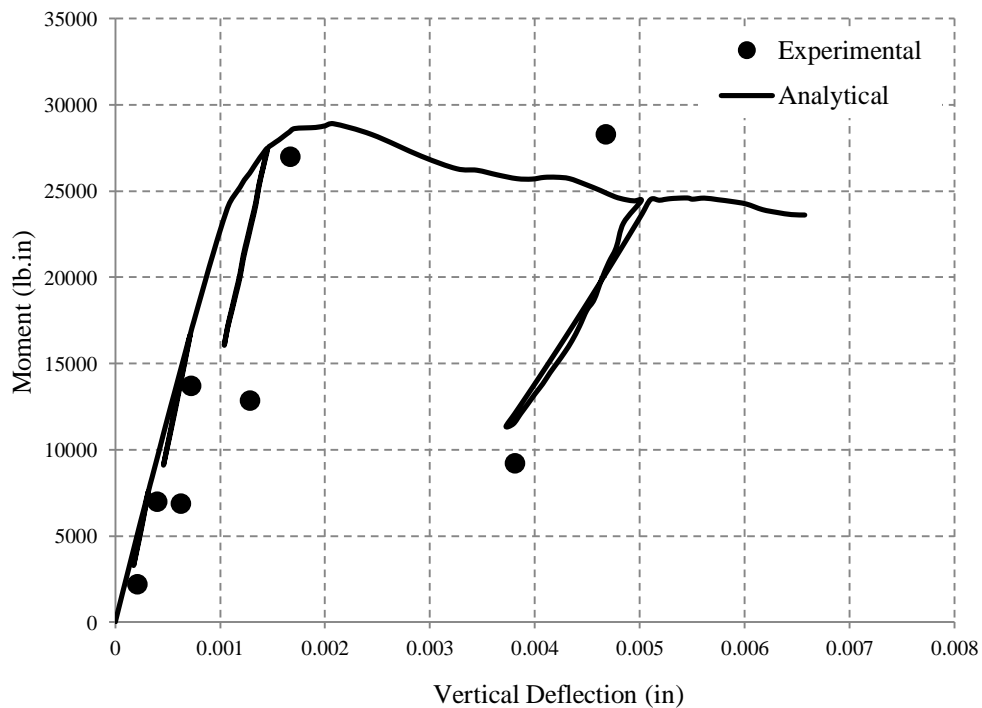


Figure D.30 Moment-curvature curve at X-direction for column C2.



**Figure D.31** Moment-curvature curve at X-direction for column C3.



**Figure D.32** Moment-curvature curve at X-direction for column C4.

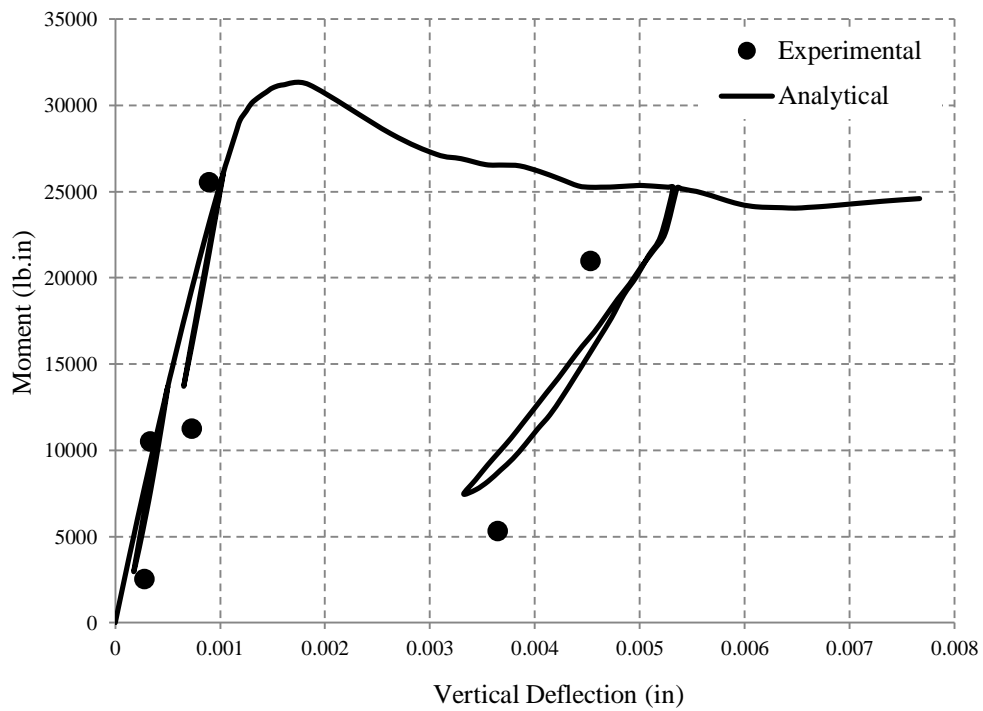
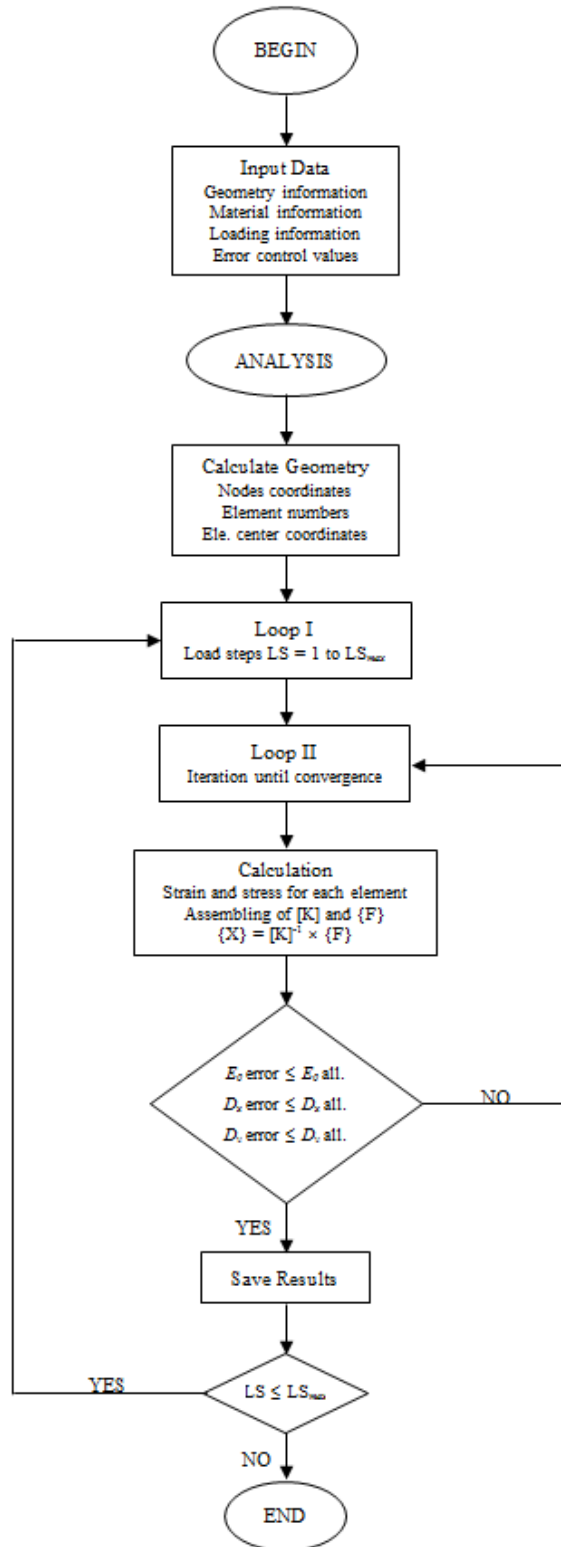


**Figure D.33** Moment-curvature curve at X-direction for column C5.

## APPENDIX E

### COMPUTATIONAL PROCESS FLOWCHART





## REFERENCES

- ACI Committee 318. (2011). *Building Code Requirements for Structural Concrete (ACI 318-05) and commentary (ACI 318R-05)*. Farmington Hills, MI: American Concrete Institute.
- ACI Committee 363. (1992). *State-of-the-Art Report on High-Strength Concrete*. Farmington, MI: American Concrete Institute.
- Azizinamini, A., Kuska, S. S., Brungardt, P., & Hatfied, E. (1994). Seismic Behavior of Square High Strength Concrete Columns. *ACI Structural Journal*, 91(3), 336-345.
- Bae, S., & Bayrak, O. (2003). Stress Block Parameters for High-Strength Concrete Members. *ACI Structural Journal*, 100(5), 626-636.
- Bahn, B. Y. (1994). Behavior of Concrete and Slender Reinforced Concrete Columns under Cyclic Axial Compression with Bidirectional Eccentricities. *Doctoral Thesis*. Newark, NJ: NJIT.
- Barros, J. A., Ferreira, D. R., & Varma, R. K. (2008). CFRP-Confined Reinforced Concrete Elements Subjected to Cyclic Compressive Loading. *ACI Special Publication*, 258, 85-104.
- Bibsy, L., & Ranger, M. (2010). Axial-Flexural Interaction in Circular FRP-Confined Reinforced Concrete Columns. *Construction and Building Materials*, 24, 1672-1681.
- Bisby, L. A., Dent, A. J., & Green, M. F. (2005). Comparison of Confinement Models for Fiber-Reinforced Polymer-Wrapped Concrete. *ACI Structural Journal*, 102(1), 62-72.
- Bousias, S. N., Triantafillou, T. C., Fardis, M. N., Spathis, L., & O'Regan, B. A. (2004). Fiber-Reinforced Polymer Retrofitting of Rectangular Reinforced Concrete Columns with or without Corrosion. *ACI Structural Journal*, 101(4), 512-520.
- Carreira, D. J., & Chu, K. H. (1985). Stress-Strain Relationship for Plain Concrete in Compression. *ACI Journal*, 82(6), 797-804.
- Chen, D. (1995). Stress-Strain Behavior of High-Strength Concrete Cylinders. *Doctoral Thesis*. Newark, NJ: NJIT.
- Chen, J. (2005). Behavior of Structural Concrete Members Strengthened by Composite Fabrics. *Doctoral Thesis*. Newark, NJ: NJIT.
- Dundar, C., Tokgoz, S., Tanrikulu, A. K., & Baran, T. (2008). Behaviour of Reinforced and Concrete-Encased Composite Columns Subjected to Biaxial Bending and Axial Load. *Building and Environment*, 1109-1120.
- Esmaily, A., & Xiao, Y. (2005). Behavior of Reinforced Concrete Columns Under Variable Axial Loads: Analysis. *ACI Structural Journal*, 102(5), 736-744.

- Hadi, M. N., & Zhao, H. (2011). Experimental Study of High-Strength Concrete Columns Confined with Different Types of Mesh under Eccentric and Concentric Loads. *ASCE, Journal of Materials in Civil Engineering*, 23(6), 823-832.
- Harajli, M. H., & Rteil, A. A. (2004). Effect of Confinement Using Fiber-Reinforced Polymer or Fiber-Reinforced Concrete on Seismic Performance of Gravity Load-Designed Columns. *ACI Structural Journal*, 101(1), 47-56.
- Hsu, C. T. (1974). Behavior of Structural Concrete Subjected to Biaxial Flexural and Axial Compression. *Doctoral Thesis*. Montréal, QC, Canada: McGill University.
- Hsu, C. T., & Punurai, W. (2011). Tension and Compression Strengthening of RC Structural Members by CFRP Composite Fabrics. *American Concrete Institute SP 275-69*.
- Hsu, L. S. (1992). Behavior of High Strength Concrete and Slender Reinforced Concrete Columns with and without Steel Fibers. *Doctoral Thesis*. Newark, NJ: NJIT.
- Kachlakev, D. I. (2002). Finite Element Analysis of Historic Bridge Strengthened with FRP Laminates. *Third International Conference on Composites in Infrastructure*. San Francisco, CA.
- Konstantinidis, D. K., Kappos, A. J., & Izzuddin, B. A. (2007). Analytical Stress–Strain Model for High-Strength Concrete Members under Cyclic Loading. *Journal of Structural Engineering*, 484-494.
- Lam, L., & Teng, J. (2003). Design-Oriented Stress–Strain Model for FRP-Confined Concrete. *Construction and Building Materials*, 17(6-7), 471-489.
- Légerona, F., & Paultre, P. (2003). Uniaxial Confinement Model for Normal- and High-Strength Concrete Columns. *ASCE, Journal of Structural Engineering*, 129(2), 241-252.
- Lu, X. (2005). Uniaxial and Triaxial Behavior of High Strength Concrete with and without Steel Fibers. *Doctoral Thesis*. Newark, NJ: NJIT.
- Matsuda, T.; Satu, H.; Fujiwara, H.; Higashira, N. (1990). Effect of Carbon Fiber Reinforcement as a Strengthening Measure for Reinforced Concrete Bridge Piers. *First U.S.-Japan Workshop on Seismic Retrofit of Bridges*. Tsukuba Science City, Japan: Public Works Research Institute, Ministry of Construction.
- Mirmiran, A. S., Samaan, M., El Chary, H., Mastrapa, J. C., & Pico, O. (1998). Effect of Column Parameters on FRP-Confined Concrete. *ASCE, Journal of Composites for Construction*, 2(4), 175-185.
- Mirmiran, A., & Shahawy, M. (1997). Behavior of Concrete Columns Confined by Fiber Composites. *ASCE, Journal of Structural Engineering*, 123(5), 583-590.
- Muffi, A. A., Erki, M. A., & Jaeger, L. G. (1991). Advanced Composite Materials with Applications. *State-of-the-art*. Montreal, Canada: CSCE.

- Naguib, W., & Mirmiran, A. (2002). Time-Dependent Behavior of Fiber-Reinforced Polymer-Confined Concrete Columns under Axial Loads. *ACI Structural Journal*, 99(2), 142-148.
- Ozbakkaloglu, T., & Akin, E. (2011). Behavior of FRP-Confined Normal- and High-Strength Concrete under Cyclic Axial Compression. *ASCE, Journal of Composites for Construction*.
- Pallarés, L., Bonet, J., Miguel, P., & Prada, M. A. (2008). Experimental Research on High Strength Concrete Slender Columns Subjected to Compression and Biaxial Bending Forces. *Engineering Structures*, 30, 1879-1894.
- Pantelides, C. P., & Gergely, J. (2002). Carbon-Fiber-Reinforced Polymer Seismic Retrofit of RC Bridge Bent: Design and In Situ Validation. *ASCE, Journal of Composites for Construction*, 6(1), 52-60.
- Rochette, P., & Labossière, P. (2000). Axial Testing of Rectangular Column Models Confined with Composites. *ASCE, Journal of Composites for Construction*, 4(3), 129-136.
- Saadatmanesh, H., Ehsani, M. R., & Jin, L. (1996). Seismic Strengthening of Circular Bridge Pier Models with Fiber Composites. *ACI Structural Journal*, 93(6), 639-647.
- Saadatmanesh, H., Ehsani, M. R., & Jin, L. (1997). Repair of Earthquake-Damaged RC Columns with FRP Wraps. *ACI Structural Journal*, 94(2), 206-214.
- Saadatmanesh, H., Ehsani, M. R., & Li, M. W. (1994). Strength and Ductility of Concrete Columns Externally Reinforced with Fiber Composite Straps. *ACI Structural Journal*, 91(4), 434-447.
- Saadeghvaziri, M. A. (1997). Nonlinear Response and Modeling of RC Columns Subjected to Varying Axial Load. *Engineering Structures*, 19(6), 417-424.
- Sadeghian, P., Rahai, A. R., & Ehsani, M. R. (2010). Experimental Study of Rectangular RC Columns Strengthened with CFRP Composites under Eccentric Loading. *ASCE, Journal of Composites for Construction*, 14(4), 443-450.
- Sarkeret, P. K., & Rangan, B. V. (2003). Reinforced Concrete Columns under Unequal Load Eccentricities. *ACI Structural Journal*, 100(4), 519-528.
- Sause, R., Harries, K. A., Walkup, S. L., Pessiki, S., & Ricles, J. M. (2004). Flexural Behavior of Concrete Columns Retrofitted with Carbon Fiber-Reinforced Polymer Jackets. *ACI Structural Journal*, 101(5), 708-716.
- Seible, F., Priestley, M. J., Hegemier, G. A., & Innamorato, D. (1997). Seismic Retrofit of RC Columns with Continuous Carbon Fiber Jackets. *ASCE, Journal of Composites for Construction*, 1(2), 52-60.
- Sheikh, S. A., & Yau, G. (2002). Seismic Behavior of Concrete Columns Confined with Steel and Fiber-Reinforced Polymers. *ACI Structural Journal*, 99(1), 72-80.

- Sheikh, S. A., Shah, D., & Khory, S. D. (1994). Confinement of High Strength Concrete Columns. *ACI structural Journal*, 91(1), 100-111.
- Srikanth, M., Rajesh Kumar, G., & Giri, S. (2007). Moment Curvature of Reinforced Concrete Beams Using Various Confinement Models and Experimental Validation. *Asian Journal of Civil Engineering*, 8(3), 247-265.
- Teng, J. G., Jiang, T., Lam, L., & Luo, Y. Z. (2009). Refinement of a Design-Oriented Stress-Strain Model for FRP-Confined Concrete. *Journal of Composites for Construction, ASCE*, 13(4), 269-278.
- Tsao, W. (1991). Behavior of Square and L-Shaped Slender Reinforced Concrete Columns Under Combined Biaxial Bending and Axial Loading. *Doctoral Thesis*. Newark, NJ: NJIT.
- Wang, G. (1990). Complete Load-Deformation Behavior of Biaxially Loaded Reinforced Concrete Columns. *Doctoral Thesis*. Newark, NJ: NJIT.
- Wang, G. (1995). Analysis of Plates and Reinforced Concrete Columns by Cubic B-Spline Function. *Doctoral Thesis*. Newark, NJ: NJIT.
- Wei, H., Wu, Z., Guo, X., & Yi, F. (2009). Experimental Study on Partially Deteriorated Strength Concrete Columns Confined with CFRP. *Engineering Structures*, 31, 2495-2505.
- Wu, H. L., Wang, Y. F., Yu, L., & Li, X. R. (2009). Experimental and Computational Studies on High-Strength Concrete Circular Columns Confined by Aramid Fiber-reinforced Polymer Sheets. *ASCE, Journal of Composites for Construction*, 13(2), 125-134.
- Yamamoto, T. (1992). FRP Strengthening of RC Columns for Seismic Retrofitting. *10th World Conference of Earthquake Engineering*. Rotterdam, the Netherlands.
- Ye, L., Zhang, K., Zhao, S., & Feng, P. (2003). Experimental Study on Seismic Strengthening of RC Columns with Wrapped CFRP Sheets. *Construction and Building Materials*, 17, 499-506.
- Yong, Y. K., Nour, M. G., & Nawy, E. G. (1988). Behavior of Laterally Confined High-Strength Concrete under Axial Loads. *ASCE, Journal of Structural Engineering*, 114(2), 332-351.